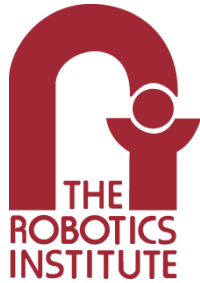


# **Handheld Micromanipulator for Robot-Assisted Microsurgery**

Sungwook Yang

CMU-RI-TR-15-11

**MAY 2015**



Robotics Institute  
Carnegie Mellon University  
Pittsburgh, Pennsylvania, 15213

## **THESIS COMMITTEE**

---

Cameron N. Riviere (Chair)

George A. Kantor

George D. Stetten

Gregory D. Hager (Johns Hopkins University)

*Submitted in partial fulfillment of the requirements  
for the degree of Doctor of Philosophy in Robotics.*

Copyright © 2015 Sungwook Yang. All rights reserved.



## ABSTRACT

Robot-assisted surgery has been increasingly adopted in a wide variety of surgical applications because it offers fine manipulation with high precision and dexterity. Despite the commercial success of robotic platforms, practical use in microsurgery is still challenging due to a considerable level of accuracy required at sub-millimeter scales. Limited visualization and constrained accessibility also hinder operation under operating microscopes. Furthermore, lack of tactile feedback may lead to substantial and even irrecoverable injury.

To address these issues in microsurgery, a handheld micromanipulator, Micron, has been introduced as an alternative to conventional robotic platforms. It allows surgeons to directly maneuver surgical tools, while selectively filtering out erroneous motion such as hand tremor. Thus, surgeons can attain the natural feel of manual operation and also direct tactile feedback from the tool attached to Micron. However, the existing Micron still entails several drawbacks in terms of the lack of degrees of freedom, limited range of motion, and ergonomically undesirable design.

This thesis presents a new design of the handheld micromanipulator and also explores automated microsurgery in conjunction with image-guidance. For the design of a miniature 6-DOF manipulator, a new optimization framework is introduced, resulting in the optimal dimension of the manipulator given the limited force capability of the miniature actuators used. Given the 6-DOF manipulation, the new platform allows the possibility of imposing a remote center of motion (RCM) for controlling an end-effector, which is generally required in most of minimally invasive surgery. Moreover, the new manipulator attains an order-of-magnitude increase in the range of motion so that it enables automated operations for intraocular OCT scanning and laser photocoagulation. We experimentally verify the design of the 6-DOF Micron and also evaluate its handheld performance under various conditions, which shows significant reduction of hand tremor. In addition, the 6-DOF Micron is utilized to improve the quality of handheld OCT imaging and obtain multi-dimensional structures from single-fiber OCT scanning.

The goal of this thesis is to accomplish automated subtasks in microsurgery using the newly developed handheld micromanipulator and image-guidance in realistic environments. Initial work demonstrates the feasibility of automated intraocular laser photocoagulation using position-based visual servoing, while compensating the eye movement. To realize automated surgery in an intact eye, we propose a monocular hybrid visual servoing scheme, incorporating cone beam reconstruction for surface estimation, partitioned visual servoing control, and adaptive frameworks in control. These approaches are validated through experiments with the eye phantom *in vitro* and porcine eyes *ex vivo*.



# ACKNOWLEDGEMENTS

This thesis would not have been possible without the support and assistance of many people. First, I would like to thank my advisor Dr. Cameron Riviere for his mentorship and encouragement. A wide range of his knowledge and wisdom have always motivated me to be creative in tackling challenges lying on my research. I also greatly thank to my thesis committee members, Dr. George Kantor, Dr. Geroge Stetten, and Dr. Gregory Hager for graciously agreeing to serve on my committee, and for providing invaluable insights and guidance for this thesis.

I also would like to thank the Kwanjeong Educational Foundation and its founder, Chonghwan Lee. Without the scholarship from the foundation, I would not have had an opportunity to pursue my doctoral study that I was eager to explore. I should say special thanks to Dr. Eui-Sung Yoon for his encouragement, and KIST for granting a leave of absence for my PhD study.

A huge thank you should also go to Dr. Louis Lobes and Dr. Joseph Martel for proving their surgical knowledge and skill to the project, but first and foremost for spending their valuable time in patiently performing tedious and buggy surgical experiments.

I would like to thank the members of the Surgical Mechatronics Lab. It has been a great opportunity to work with a professional research engineer, Robert MacLachlan. I also like to give special thanks to Brian Becker for his comments and feedbacks. I also thank to all present and past lab members, Nathan Woods, Craig Lehocky, and Trent Wells. I have really enjoyed a great time with the guys while staying in Pittsburgh and it would be unforgettable moments.

Thanks to RI Korean folks, Young-Woo Seo, Hwangbo Myung, Seung-il Huh, Seunmoon Song, Hanbyul Joo, and Sung Kyun Kim for all supports that allow me to have survived in the RI. I am very grateful to have many friends to hang out, discuss ideas, and share joy and agony with them. Special thanks to my buddies, Hyunggi Cho, Hyunsoo Park, Junsung Kim, Jiho Song, and Jonghan Kwon. To all KiDisTech members, in every meeting, it was a really great pleasure to meet people in a variety of research fields and to draw new and cool ideas.

My biggest thanks go to my family. To my parents, thank you for your patience and for your support. I should also say heartfelt thanks to my sister, who had lived in Pittsburgh together and taken care of me as well as our house. Without her devotion, it would not have been possible to focus on research and to reach this thesis.

It would be difficult to name all the people who have helped me through the PhD in Pittsburgh and also in Korea, but I should say heartfelt thanks to all.



# CONTENTS

1	Introduction	1
1.1	Motivation.....	1
1.2	Approach.....	3
1.3	Contributions .....	5
1.4	Outline .....	6
2	Background	7
2.1	Problem Domain.....	7
2.1.1	Retinal Diseases .....	7
2.1.2	Vitreoretinal Surgery.....	8
2.2	Robot-Assisted Retinal Surgery .....	11
2.2.1	Teleoperated Robots.....	11
2.2.2	Cooperative Robots .....	14
2.2.3	Handheld Robots .....	15
2.2.4	Microrobot Approach .....	19
2.3	Summary.....	20
3	Handheld Micromanipulator Design	21
3.1	Related Work .....	21
3.2	Kinematic Design .....	23
3.2.1	Kinematics.....	23
3.2.2	Generalized Force on Link.....	26
3.2.3	Design Optimization.....	27
3.2.4	Workspace Analysis .....	30
3.3	Mechanical Design .....	32
3.3.1	Miniature 6-DOF Manipulator .....	32
3.3.2	Handheld Manipulator Design .....	34
3.4	Control .....	37
3.5	Design Validation .....	39

3.5.1	Side Load Capability .....	39
3.5.2	Reachable Workspace .....	40
3.6	Summary.....	41
<b>4</b>	<b>Handheld Micromanipulator Performance</b>	<b>43</b>
4.1	Manipulator Evaluation .....	43
4.1.1	Positioning Performance .....	43
4.1.2	Dynamic Performance .....	44
4.2	Position Tracking Performance .....	46
4.2.1	Pointing Task.....	46
4.2.2	Circle-Tracing Task.....	47
4.3	Active Tremor Cancellation .....	49
4.3.1	Rubber Target: Hold-Still.....	50
4.3.2	Rubber Target: Circle Tracing .....	51
4.3.3	Eye Phantom: Hold-Still .....	52
4.4	Summary.....	55
<b>5</b>	<b>Intraocular Optical Coherence Tomography</b>	<b>57</b>
5.1	Related Work .....	57
5.2	System Integration .....	59
5.3	Stabilization of Handheld Imaging.....	61
5.3.1	Open-Sky: A-Mode Scan .....	61
5.3.2	In-vivo: A-Mode Scan .....	62
5.3.3	In-vivo: M-mode Scan.....	63
5.4	Multidimensional Scanning.....	65
5.4.1	C-Mode Scan .....	65
5.4.2	B-Mode Scan .....	66
5.5	Summary.....	67
<b>6</b>	<b>Robot-Aided Intraocular Laser Surgery I: Position-Based Visual Servoing</b>	<b>69</b>
6.1	Related Work .....	70

6.2	System Overview .....	72
6.2.1	System Calibration .....	75
6.2.2	Retinal Surface Reconstruction .....	77
6.3	Position-Based Visual Servoing .....	79
6.3.1	Control Principle .....	79
6.3.2	Surface Tracking .....	80
6.4	Experiments and Results.....	83
6.4.1	Control Performance .....	83
6.4.2	Handheld Performance .....	84
6.4.3	Eye Phantom.....	86
6.5	Summary.....	87
7	Robot-Aided Intraocular Laser Surgery II: Hybrid Visual Servoing	89
7.1	System Overview .....	90
7.1.1	Graphical Overlay System.....	92
7.2	Hybrid Visual Servoing .....	93
7.2.1	Control Principle .....	93
7.2.2	Image Jacobian Update .....	96
7.3	Experiments and Results.....	98
7.3.1	Experimental Setup .....	98
7.3.2	Data Analysis .....	99
7.3.3	Results .....	100
7.4	Comparative Evaluation .....	105
7.4.1	Experimental Setup .....	105
7.4.2	Open-Sky .....	106
7.4.3	Eye Phantom.....	108
7.5	Summary.....	111
8	Robot-Aided Intraocular Laser Surgery using Monocular Vision	113
8.1	Related Work .....	114
8.2	Retinal Surface Estimation using Monocular Vision .....	116
8.2.1	Projective Geometry Analysis.....	117

8.2.2	Dual Cone Beam Reconstruction .....	120
8.2.3	Single Cone Beam Reconstruction.....	125
8.3	Evaluation of Cone Beam Reconstruction.....	129
8.3.1	Simulation .....	129
8.3.2	Tests with Real Data.....	132
8.4	Visual Servoing Experiments and Results.....	138
8.4.1	Eye Phantom.....	138
8.4.2	Porcine Eye.....	139
8.5	Summary .....	143
9	Conclusion	145
9.1	Contributions .....	146
9.2	Future Directions .....	147
9.3	Concluding Remarks .....	150
	Bibliography	151

# LIST OF FIGURES

Fig. 2.1 Exemplary photos shown on eyesight by retinal diseases.....	7
Fig. 2.2. Illustration of pars planar vitrectomy.....	8
Fig. 2.3. (a) Illustration of laser photocoagulation. (b) Retinal tear treated with laser photocoagulation.....	9
Fig. 2.4. Hexapod surgical system (HSS) integrated with the da Vinci robot.....	12
Fig. 2.5. Intraocular robotic interventional and surgical system (IRISS).....	13
Fig. 2.6. Microsurgical robotic system for vitreoretinal surgery.....	14
Fig. 2.7. New Steady Hand eye robot for vitreoretinal surgery.....	14
Fig. 2.8. (a) Initial Micron prototype. (b) <i>Itrem</i> .....	15
Fig. 2.9. 3-DOF Micron .....	16
Fig. 2.10. Other handheld manipulators.....	17
Fig. 2.11. Wireless magnetic microrobot for targeted retinal drug delivery.....	19
Fig. 3.1. 6-DOF handheld micromanipulator.....	21
Fig. 3.2. Kinematic configuration of a 6-DOF parallel mechanism with a tool tip and a remote center of motion (RCM) .....	24
Fig. 3.3. (a) The force variation with respect to the varying geometric parameters of the manipulator for side load of 0.2 N acting at the RCM. (b) The contour of the force variation with respect to the base and the top diameters at a link length of 25 mm.....	28
Fig. 3.4. (a) Reachable space (red) obtained by pivoting the tool tip around a predefined RCM. The cylinder (blue) inside the space indicates the desired workspace. (b) The reachable space depending on applied side load.....	30
Fig. 3.5. Miniature 6-DOF manipulator, compared with a US quarter.....	32
Fig. 3.6. Exploded view of the handheld manipulator assembly (top) and the linear actuation module (bottom).....	34
Fig. 3.7. Micron system architecture.....	37
Fig. 3.8. Linearization curve: velocity with respect to motor command (duty cycle). ....	38

Fig. 3.9. Experimental setup for measuring side load capability (a) and resulting trajectory with respect to the amount of the side load (b).....	39
Fig. 3.10. Demonstration confirming attainment of the specified workspace. ....	40
Fig. 4.1. Frequency response of the micromanipulator.....	44
Fig. 4.2. Trajectory of the tool tip during a pointing task .....	46
Fig. 4.3. (a) RMS error during automatic handheld circle-tracing with various circle diameters and tracking velocities. (b) Trajectory of circle-tracing for various sizes of circles.....	47
Fig. 4.4. Simulated Micron low-frequency response, hand to tip. ....	49
Fig. 4.5. Experimental setup. (a) Micron, (b) ASAP, (c) microscope, (d) CCD camera, and (e) eye phantom. ....	50
Fig. 4.6. Average RMS and maximum errors for hold-still (top) and circle-tracing (bottom) tasks.....	51
Fig. 4.7. Result of circle-tracing task according to three control modes. (a) Unaided (off) trial, (b) aided trial with lowpass, (c) aided trial with scaling mode. ....	52
Fig. 4.8. Result of hold still task in an eye phantom. (a) Unaided (off) trial, (b) aided trial with lowpass, (c) aided trial with scaling mode. ....	53
Fig. 4.9. Average RMS and maximum errors for hold-still task in an eye phantom .....	53
Fig. 5.1. Schematic diagram of a handheld OCT imaging system using Micron. ....	59
Fig. 5.2. Micron, an active handheld micromanipulator with an OCT probe (a) and the OCT probe with multiple sheaths of hypodermic tubing. ....	60
Fig. 5.3. (a) A-scans during hold-still task above a fundus image. (b) OCT scans (A-scan and M-scan) in a live rabbit eye. ....	61
Fig. 5.4. Results of OCT scan images and short-time Fourier transform (STFT) of surface profiles for the control modes, arranged in descending order: <i>unaided, lowpass, and scaling</i> .....	62
Fig. 5.5. Results of OCT M-scan images in the live rabbit eye and STFT of surface profiles. ....	64
Fig. 5.6. Results of OCT scanned profiles (top) and power spectrogram (bottom). (a) A-scans during hold-still task in the air. (b) A-scans during hold-still task in the	

live rabbit eye. (c) M-scans, manually scanning a line of interest in the live rabbit eye. In the A-scans, the profiles are the axial deviation of the tip. ....	64
Fig. 5.7. (a) USAF 1951 MIL-STD-150A resolution test chart. (b) Result of spiral C-mode scan of USAF 1951 MIL-STD-150A resolution test chart, group 1, element 4.....	65
Fig. 5.8. Result of zigzag B-mode scan of a stack of 3 layers of 3M™ Polyester Tape 8911..	66
Fig. 6.1. 6-DOF handheld micromanipulator integrated with a laser probe. ....	72
Fig. 6.2. System setup for automated intraocular laser surgery .....	73
Fig. 6.3. Block diagram of the system, showing data and execution flow.....	74
Fig. 6.4. Tip position collected during the calibration procedure. ....	76
Fig. 6.5. Visualization of the control procedure. ....	79
Fig. 6.6. 3D planar surface tracking, utilizing the 2D retinal vessel mapping and localization.....	81
Fig. 6.7. Automated laser photocoagulation results according to various control thresholds on a fixed paper slide under a clamped condition .....	83
Fig. 6.8. Average errors for different tasks and settings, with error bars.....	85
Fig. 6.9. Handheld performance on a fixed paper slide: automated vs. manual. ....	85
Fig. 6.10. Demonstration of the automated intraocular laser photocoagulation in an eye phantom. ....	86
Fig. 7.1. Automated intraocular laser surgery system. (a) Handheld instrument (Micron) and eye phantom. (b) Overall system setup, including the Micron controller, the operating microscope, the graphical overlay system, and the laser controller. (c) Graphical overlays shown through the right eyepiece of the operating microscope.....	90
Fig. 7.2. Block diagram of the system, showing data and execution flow.....	91
Fig. 7.3. Visualization of the control procedure .....	96
Fig. 7.4. Results from eye phantom trials. The top row (a–d) presents automated trials with targeting tolerances of 50–200 $\mu\text{m}$ : (a) 50 $\mu\text{m}$ , (b) 100 $\mu\text{m}$ , (c) 150 $\mu\text{m}$ , and (d) 200 $\mu\text{m}$ targeting threshold. The bottom row (e–h) shows manual trials with	

laser repeat rates of 1.0–2.5 Hz: (e) 1.0 Hz, (f) 1.5 Hz, (g) 2.0 Hz, and (h) 2.5 Hz repetition rate.....	100
Fig. 7.5. Overall mean error for automated and manual trials at various speeds.....	101
Fig. 7.6. Normalized histograms of error for automated and manual trials.....	101
Fig. 7.7. Proportion of erroneous outcomes over the entire targets .....	102
Fig. 7.8. Automated avoidance of blood vessels in automated laser photocoagulation..	104
Fig. 7.9. Targeting error vs. effective frequency in both open-sky and eye phantom tasks.	
.....	106
Fig. 7.10. Representative figures for a 1.0 Hz repetition rate in the open-sky and the eye phantom tasks.....	107
Fig. 7.11. Average error for various repetition rates in the open-sky task.....	107
Fig. 7.12. Average error for various repetition rates in the eye phantom task.....	109
Fig. 8.1. Illustration of a conic section shown as an ellipse on the retinal surface.....	116
Fig. 8.2. Cone beam analysis and corresponding parameters to describe a target plane.	118
Fig. 8.3. An infinite set of surface normal vectors existing along the axis of the cone. (a) The identical shapes of ellipses according to different axes of rotation. (b) The infinite set of normal vectors is represented as a 3D circle (the cyan color) in the ASAP coordinates.....	119
Fig. 8.4. (a) Conic sections forming two ellipses on the retinal surface by circular scanning of the laser probe about the axis of the tool. (b) Resulting ellipses shown in the image plane. ....	120
Fig. 8.5. Illustration of the infinite sets of two initial normal vectors in the unit sphere.	
.....	121
Fig. 8.6. The dotted lines indicate the ellipses when the major axis of the first ellipse (blue) is aligned with the $x$ -axis. The solid lines represent the final trajectories after applying the coordinate mapping, which is subject to being identical to the trajectories in the camera view as shown in Fig. 8.4(b). .....	123
Fig. 8.7. Estimated surface via dual cone beam reconstruction. ....	124
Fig. 8.8. Failure cases of dual cone beam reconstruction with real data. ....	125
Fig. 8.9. Ellipse trajectories for demonstration of the single cone beam reconstruction.	126

Fig. 8.10. The tip angle with respect to the estimated plane, according to the aspect ratio of an ellipse.....	130
Fig. 8.11. (a) Angle error in surface normal estimation, led by errors in lengths of the major and minor axes in pixels. (b) Surface depth error by variation on lengths of the major and minor axes. ....	131
Fig. 8.12. (a) Depth error in surface estimation, led by the angle error in estimation of the surface normal. (b) Depth error according to uncertainty on the image scale. 131	
Fig. 8.13. Ellipse trajectories with respect to the size of scanning diameter. ....	133
Fig. 8.14. Angle and depth errors in surface estimation with respect to the size of scan diameter: (a) angle error and (b) depth error. ....	133
Fig. 8.15. (a) Repeated measurements of angle errors for 10 trials. (b) Depth errors for 10 trials. ....	134
Fig. 8.16. Ellipse trajectories obtained by handheld beam scanning .....	135
Fig. 8.17. Angle and depth errors in surface estimation by handheld cone beam scanning: (a) angle errors and (d) depth errors. ....	135
Fig. 8.18. (a) Eye phantom filled with water and also covered with the contact lens. (b) Resulting ellipse trajectory obtained by handheld scanning in the eye phantom. ....	136
Fig. 8.19. Demonstration of hybrid visual servoing based on the cone beam reconstruction in the wet eye phantom. ....	139
Fig. 8.20. (a) Porcine eye and intraocular surgical setup for the test <i>ex vivo</i> . (b) Elliptical trajectories created by cone beam scans inside the porcine eye. ....	140
Fig. 8.21. Demonstration of automated intraocular laser surgery in a porcine eye <i>ex vivo</i> . 141	



# LIST OF TABLES

Table 2.1. Comparison of Handheld Micromanipulators.....	18
Table 3.1. Specification of 6-DOF Micron .....	36
Table 3.2. RMS Errors with respect to the Goal Trajectories for Side Loads .....	39
Table 4.1. RMS Errors with respect to the Planned Trajectories and Various Velocities .	43
Table 4.2. Comparison of 3D RMS and Maximum Errors .....	54
Table 5.1. Errors during Hold-Still Tasks.....	63
Table 6.1. Summary of Experimental Results for Automated Laser Photocoagulation ...	84
Table 7.1. Summary of Experimental Results .....	103
Table 7.2. Comparison of Automated and Manual Trials with the Interpolated Data at Equivalent Frequencies .....	103
Table 7.3. Summary of Experimental Results in Open-Sky Task .....	108
Table 7.4. Summary of Experimental Results in Eye Phantom Task .....	110
Table 8.1. Settings for Evaluation of Cone Beam Reconstruction .....	129



# 1 INTRODUCTION

## 1.1 Motivation

Microsurgery is challenging even for an experienced surgeon because small anatomy in the sub-millimeter range is beyond the precision of human manipulation. In particular, vitreoretinal surgery<sup>1</sup> is a prime example, requiring such a considerable level of accuracy in operation, since retinal vasculature is often less than 100  $\mu\text{m}$  and membranes such as the internal limiting membrane (ILM) in the eye are around 5–10  $\mu\text{m}$  [1]. Meanwhile, surgeons' hand tremor has been reported at the level of hundreds of micrometers [2], [3]. In addition to such a high demand of precision, limited visualization and constrained accessibility lead to poor control of surgical tools [4]. Lack of tactile feedback could also be problematic during retinal surgery [5]. The eye would not be regenerated if injured [6], [7]

Robot-aided micromanipulation can be a promising solution to these problems since it has offered a variety of advantages over conventional techniques in biomedical applications [8]–[10]. For example, robotic platforms enable fine manipulation with high precision and dexterity during surgery by tremor filtering and also motion scaling [11]–[13]. In addition, subtasks can be automated, alleviating the cognitive load of repetitive procedures and improving accuracy [14].

To provide a stable base for accurate manipulation, most platforms are mechanically grounded [15]–[17]. However, these systems involve potential risks during operation due to their relatively large range of motion and high inertia [18], the risk being exacerbated by the tendency of patients to move during surgery, especially when merely sedated rather than anesthetized, as in ophthalmic surgery [19]. Teleoperation also involves a separation between surgeon and patient, and a lack of natural feel in manipulation.

To address the latter problems, a cooperative robot, the Steady Hand, has been developed, using shared control principles [20], [21]. The robot selectively complies with force/torque sensor input, allowing voluntary motion and suppressing tremor while a surgeon simultaneously holds the surgical instrument. The Steady Hand thus provides a more direct coupling to the human's natural kinesthetic sense [20]. However, the system still has the same drawback with respect to the possibility of patient movement [22].

---

<sup>1</sup>A typical method to treat several ophthalmologic problems, such as retinal detachment, vitreous hemorrhage, macular pucker, macular hole and diabetic retinopathy [7].

As an alternative, a fully handheld micromanipulator, Micron, has been introduced, to retain the surgeon's direct manual control of gross positioning of the tool and to preserve the natural feel of manual operation [22], [23]. The handheld manipulator senses its own motion and selectively filters out erroneous motion such as hand tremor. The manipulator then produces stabilized motion at the tool tip via active error compensation.

Despite its advantages in terms of usability, safety, and economy [23], the present system, 3-DOF Micron, still entails several drawbacks that must be overcome for practical use in microsurgery. First of all, due to the limited number of degrees of freedom (DOF) in manipulation, the system cannot offer a remote center of motion (RCM), as is generally required in most of minimally invasive surgery [24], [25]. In particular, for intraocular surgery, an RCM is necessary in order to avoid unwanted transverse movement at the point of entry through the sclera [25]. In addition, the range of motion at the tip of the current 3-DOF Micron system is limited to a few hundred micrometers due to the small displacement of the piezoelectric bender actuators used [23]. This results in frequent saturation of the actuators due to large or rapid motion of the hand. The limited range of motion also hinders Micron from being used in numerous applications such as patterned laser photocoagulation [26]. For such applications, an order-of-magnitude increase in the range of motion is needed [23]. Moreover, the wide head of the existing design of Micron due to the shape of the bender actuators is ergonomically undesirable and likely to interfere with the sight line of the operating microscope [23].

Therefore, a new design of the handheld micromanipulator, namely 6-DOF Micron, is proposed for microsurgery, having a larger range of motion, more degrees of freedom in a smaller diameter. These benefits are also exploited in image-guided interventions. The 6-DOF Micron offers the stabilization of handheld imaging and also multidimensional scans in intraocular optical coherence tomography (OCT). We also demonstrate the feasibility of automated laser surgery in conjunction with visual-servoing. To accomplish automated surgery in an intact eye with limited visualization, a new visual-servoing scheme using a monocular camera is explored.

## 1.2 Approach

In this thesis, we propose a new design of the handheld micromanipulator, addressing the issues on the present handheld micromanipulator. This incorporates an appropriate selection of actuators used for the manipulator and design optimization for minimizing the dimension of the manipulator. This is of particular importance for this system due to a trade-off between the tolerable external load and the size of the manipulator, given the limited force capability of the miniature actuators used. Given the optimization, we build a fully handheld instrument incorporating a miniature 6-DOF manipulator for vitreoretinal microsurgery. The load capability and enlarged workspace derived from simulations are experimentally verified.

We extensively evaluate the performance of the 6-DOF Micron under various conditions. First, trajectory-following tasks are conducted for both grounded and ungrounded settings, in order to verify the control performance of the manipulator. Active tremor cancelling performance is then evaluated in both an open space (called open-sky) and in an eye phantom with an RCM constraint, while adopting the tremor filtering methods used in the 3-DOF Micron.

For the application of handheld OCT imaging, the 6-DOF Micron is integrated with an intraocular OCT probe developed at Johns Hopkins University. The active tremor cancelling feature is utilized to stabilize handheld scans. Moreover, the feasibility of multidimensional scans is demonstrated, by exploiting the trajectory-servoing capability of the 6-DOF Micron with a large range of motion.

The automated laser photocoagulation is also performed via visual-guidance of a stereomicroscope. First, we adopt a position-based visual servoing scheme, requiring the 3D reconstruction of a retinal surface and the aiming beam of a laser probe. We investigate the feasibility of the automated surgery in an eye phantom, while compensating the eye movement during operation by the extension to 3D of the EyeSLAM algorithm which is capable of tracking the eye in 2D [27].

Finally, in order to realize the automated laser surgery in an intact eye, we propose a hybrid visual servoing scheme using a monocular camera, since the position-based visual servoing is prone to failure in such a complex eye due to considerable optical distortion and unreliable vision detection. Hence, the proposed method relies primarily on the aiming beam that is highly detectable in the eye, regardless of illumination change. Given scanning of the aiming beam, projected beam patterns on the retinal surface is analyzed to estimate the surface in 3D, which is assumed to be parallel to an image plane. The

registration of the surface in the Micron coordinate allows us to control the aiming beam in 2D and to simultaneously regulate the depth of the laser probe from the retinal surface in 3D. To improve accuracy and reduce operating time, we also adopt adaptive frameworks to update the image Jacobian online. In this thesis, we formalize a method for the surface estimation and explore the feasibility of the partitioned control scheme with the image Jacobian update. All these approaches will be integrated and tested on realistic eye models and intact eyes, such as porcine eyes, under vitrectomy.

### 1.3 Contributions

We expect this thesis to achieve the following contributions.

- A **state-of-the-art handheld micromanipulator** is designed, providing more degrees of freedom and larger range of motion in a smaller package.
- A **new optimization framework for designing a miniature manipulator** is established.
- A **versatile handheld micromanipulator** is developed, capable of **high-precision active tremor cancellation** as well as **automated operations** requiring large range of motion.
- The new handheld manipulator is utilized in **handheld intraocular imaging: stabilizing handheld imaging and offering multidimensional scans** to single fiber OCT.
- The handheld micromanipulator enables **automated microsurgery** in conjunction with visual servoing and virtual fixture frameworks.
- A **new visual servoing framework using monocular vision** is proposed for intraocular microsurgery.
- A **new surface estimation framework** is established, using the automatic scanning of the handheld micromanipulator and the geometric analysis of projected beam patterns on the surface.
- **Automated intraocular laser surgery** is demonstrated in **a realistic eye model**.

*A novel handheld micromanipulator capable of high-precision active tremor cancellation as well as automated micromanipulation enables real-world use of handheld robot-assisted microsurgery, in conjunction with monocular surface reconstruction, visual servoing, and virtual fixture frameworks.*

## 1.4 Outline

This thesis organized as follows:

- Chapter 2 introduces a problem domain that we are particularly interested in, and provides a review of robotic platforms designed for vitreoretinal surgery. Specifically, handheld robots are thoroughly discussed for the design of a new handheld micromanipulator.
- Chapter 3 formalizes a new optimization framework for designing a miniature manipulator, and describes the micromanipulator design and overall Micron system.
- Chapter 4 evaluates the performance of the handheld micromanipulator, experimentally, for various tasks.
- Chapter 5 introduces an application of the handheld micromanipulator in handheld OCT imaging, which involves stabilization of handheld imaging, and also multidimensional scanning.
- Chapter 6 introduces handheld robot-assisted microsurgery, particularly for intraocular laser photocoagulation. We show the first demonstration of fully automated intraocular laser surgery, using the handheld micromanipulator in conjunction with position-based visual servoing.
- Chapter 7 extends the automated laser surgery introduced in Chapter 6, by applying a hybrid visual servoing scheme to address issues in the initial demonstration. With the improved system, a comparative study of handheld robot-aided laser surgery is also investigated.
- Chapter 8 proposes a new surface reconstruction method using a projective geometry of cone beam scans, in order to tackle erroneous surface estimation by conventional stereo-reconstruction in the real eye. Finally, automated laser surgery is demonstrated in the real eye, in conjunction with the hybrid visual servoing developed in Chapter 7.
- Chapter 9 revisits the contributions of this thesis, and points out future research directions with concluding remarks.

## 2 BACKGROUND

This chapter describes the survey of robot-assisted microsurgery, in particular, vitreoretinal surgery, which is the most technically demanding ophthalmologic discipline [28]. We thus regard the vitreoretinal surgery as our primary testbed for generalizing the proposed frameworks in microsurgery. First, we look through vision-threatening retinal diseases and relevant treatments in order to find appropriate applications for robotic surgery. We then review most of robotic platforms that have been developed for ophthalmic surgery, in terms of design and applicability. This will provide us with a guideline on designing a new handheld micromanipulator.

### 2.1 Problem Domain

#### 2.1.1 Retinal Diseases

In spite of progress made in surgical techniques, 285 million people are still visually impaired worldwide and 39 million of these are blind [29]. In the United States, 1.3 million people (0.9%) are blind in the population of over 40. Moreover, people who suffer from age-related macular degeneration and diabetic retinopathy are 2.1 million (1.5%) and 7.7 million (5.4%), respectively [30]. Such retinal diseases are the leading cause of new

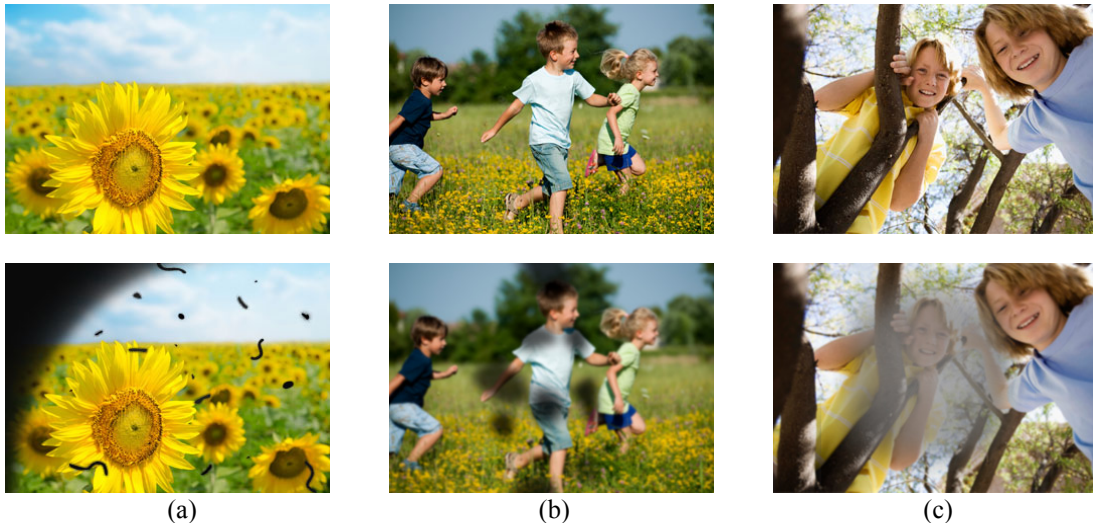


Fig. 2.1 Exemplary photos shown on eyesight by retinal diseases: retinal detachment (a), diabetic retinopathy (b), and macular degeneration (c). Each photo on the top indicates normal vision. Photo credit [170].

blindness among working-age adults in the United States [31]. As the number of people affected grows, potentially blinding eye conditions by age-related macular degeneration, diabetic retinopathy, and glaucoma are substantially increasing. For instance, the number of Americans 40 years or older with vision-threatening diabetic retinopathy will triple in 2050: from 1.2 million in 2005 to 3.4 million in 2050 [32]. Unfortunately, those blindness and vision impairment will be a significant burden, not only to those affected by slight loss, but to national economy as well, in which the costs associated with adult vision problem in the United States are estimated at \$51.4 billion [33].

### 2.1.2 Vitreoretinal Surgery

Vitreoretinal surgery is a typical method to treat several ophthalmologic problems, such as retinal detachment, vitreous hemorrhage, macular pucker, macular hole, and diabetic retinopathy [7]. In conventional vitreoretinal surgery, a pars plana vitrectomy is performed under an operating stereomicroscope as shown in Fig. 2.2, with three ports for illumination, surgical instrument (vitreous cutter, forceps, etc.), and infusion to maintain proper ocular pressure. During the procedure, the vitreous humor is replaced with substitutable liquid such as silicone oil or saline solution, to provide better access to the back of the eye. The surgeons often operate in bimanual fashion with a light pipe in one hand and an interventional tool such as a forceps, needle, or laser probe in the other hand.

Laser photocoagulation is an established treatment for a variety of retinal diseases such as proliferative retinopathy most commonly diabetic retinopathy [34], [35], sealing retinal breaks important in the successful repair of retinal detachment [36], macular edema [37],

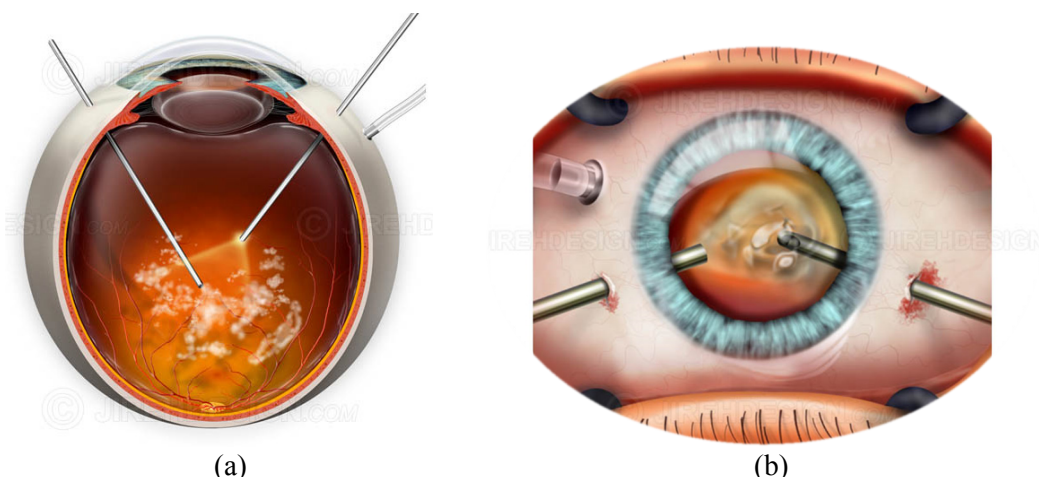


Fig. 2.2. Illustration of pars planar vitrectomy: (a) side view and (b) top view. Photo credit [171].

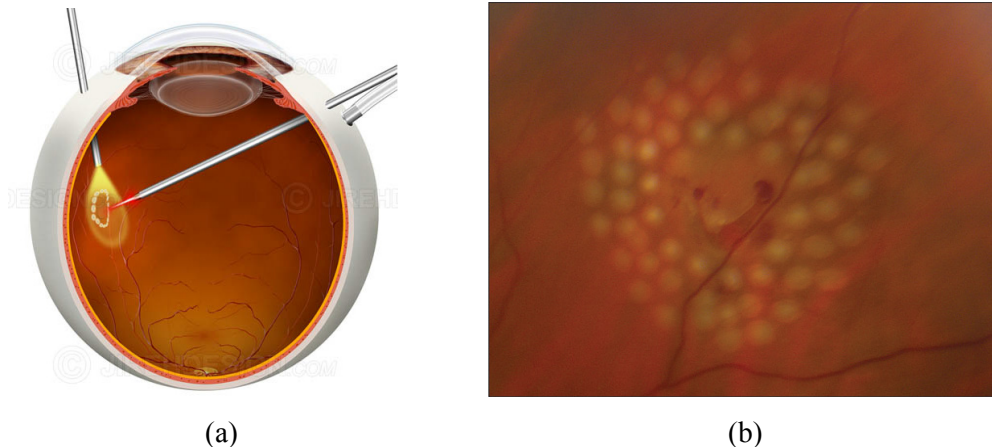


Fig. 2.3. (a) Illustration of laser photocoagulation. (b) Retinal tear treated with laser photocoagulation. Photo credits [171], [172].

[38], and treatment of retinal vascular lesions [39], [40], to name a few. The intraoperative goals of laser treatment include treatment of ischemic retina to allow regression of retinal neovascularization, formation of a chorioretinal scar around retinal breaks, treatment of leaking vascular lesions, and stimulation of the retinal pigment epithelium to reduce retinal edema.

Grid laser photocoagulation is used to directly treat a specific target region usually in the macula for treatment of macular edema [38]. Focal laser photocoagulation treats blood vessel specific lesions or a small area of the retina with a limited number of laser burns. For instance, this method can be applied to treat retinal breaks [36] or macular edema due to diabetes [37], [38] or retinal vein occlusion [39], [40], as shown in Fig. 2.3. On the other hand, panretinal (or scatter) laser photocoagulation delivers hundreds of laser burns to a wider area of the retina, usually in the regions outside the macula [34]. It is generally used as a treatment of any cause of proliferative retinopathy, the most common being proliferative diabetic retinopathy in order to lower the production proangiogenic and vascular hyperpermeability modulators most notably VEGF that may be responsible for generation of abnormal blood vessels (neovascularization). Retinal neovascularization is the precursor to the most serious vision threatening complications of proliferative retinopathy.

Another typical treatment is to peel epiretinal or internal limiting membranes from the surface of the retina for treating macular diseases [41]. Overall, those procedures require high accuracy for optimal clinical since inadvertent photocoagulation of normal blood vessels or the fovea can cause permanent vision loss [42]. In addition, long treatment

sessions may impose discomfort and tedium on both patients and ophthalmologists [43], [44]. However, surgeons encounter problems due to the limited maneuverability of surgical instruments, hand tremor, and poor visualization of surgical targets, and lack of tactile feedback in tool-to-tissue interactions [28]. For example, inadvertent photocoagulation of a vein can cause vein occlusion; peeling membranes without damaging other retinal layers is also demanding [45]. Vein cannulation is more difficult to perform [46] primarily because of limited dexterity, given the need to keep the cannula in the vessel [47].

## 2.2 Robot-Assisted Retinal Surgery

Robot-assisted surgery has been introduced in a wide variety of surgical fields, including cardiovascular surgery [48]–[50], gastrointestinal surgery [51]–[53], urology [54]–[56], gynecology [57]–[59], neurosurgery [60]–[62] and orthopedics [63]–[65]. These lists of surgical indications are growing rapidly, as the technology becomes more accessible [66]. The most common surgical robot is the master-slave da Vinci® surgical system [67], [68], which allows surgeons to remotely control a patient-side slave robot through manipulation of wristed instruments that are anthropomorphically-aligned to the surgical scene [69]. The robot offers a number of potential improvements over unassisted human hands, such as tremor filtration, scaling of motion, enhanced dexterity in confined spaces, and extremely high precision [66].

Despite the widespread applications of robotic surgery, use of robotic platforms in ophthalmic surgery is still in its infancy [70] since the surgery poses a number of unique engineering challenges for robot development [66]. Ophthalmic surgery is unique, as surgeons have direct and noninvasive visualization of surgical site and ocular structures via the transparent cornea under the high magnifications of an operating microscope. Thus, one of the foremost advantages of robotic surgery—direct visual access and microsurgical manipulation in a confined surgical site—is not relevant to ophthalmic surgery [71]. In addition, a great level of precision and dexterity is required on the order of microns, not millimeters. The pivot point, or remote center of motion, also differs from typical laparoscopic surgery, which makes adoption of commercial laparoscopic robots problematic [66]. While a number of obstacles exist for application of surgical robots in ophthalmic surgery, robotic assistance has the potential to expand our treatment armamentarium, reduce complication rates, and treat conditions that remain incurable today [66].

The following review introduces robotic platforms dedicated for ophthalmic surgery: categorized as teleoperated, cooperative, handheld, and microrobotic platforms.

### 2.2.1 Teleoperated Robots

A teleoperated platform has been widely investigated in ophthalmic surgery in order to utilize its advantages in this delicate surgery [15]. Charles *et al.* adopted a telerobotic system, called RAMS (Robot Assisted Micro Surgery), for eye surgery. This cable-driven robot was developed for high-dexterity microsurgery [16], incorporating a lightweight and

compact 6-DOF master-slave system. Although the system demonstrated high precision in a wide range of motion, the complexity of the software control and the lack of mechanical remote center of motion were the main limitations of this model. A parallel manipulator capable of imposing an RCM was also developed for intravascular drug delivery and microvascular pressure measurement [25]. However, the robot could not be intuitively operated to realize spatial motions due to an interface with a trackball and buttons. In addition, Yu *et al.* introduced a robotic ocular microsurgical system, which successfully showed intravascular drug delivery, the implantation of microdrainage devices, and the intraretinal manipulation of microelectrodes in animal trials. These early prototypes already had an appropriate remote center of motion for intraocular surgery as well as a relatively good range of motion, but they were too premature to raise a tangible interest for further development [72].

Following the great commercial success of the da Vinci® surgical system, the feasibility of intraocular robotics surgery was investigated in porcine eyes [17], [73]. Although the da Vinci surgical robot provided adequate dexterity for delicate manipulation, this system originally designed for laparoscopic surgery encountered two major issues in ophthalmic surgery. First, the kinematics of the robotic arms was awkward for intraocular maneuvers since the remote center of motion was located above the wrist, whereas it is desired to be at the surgical incision point. This resulted in less controllable motion. In addition, visualization was also challenging because the endoscopic image did not yield the same detail as acquired by an ophthalmic microscope. To address the remote center of motion problem in intraocular surgery, a hybrid type of surgical robot was proposed by combining a hexapod manipulator with the da Vinci robot [74], [75], which allows the pivot point of intraocular instruments to be at the entry point as shown in Fig. 2.4. Recently, the UCLA group introduced the intraocular robotic interventional surgical system (IRISS), presented

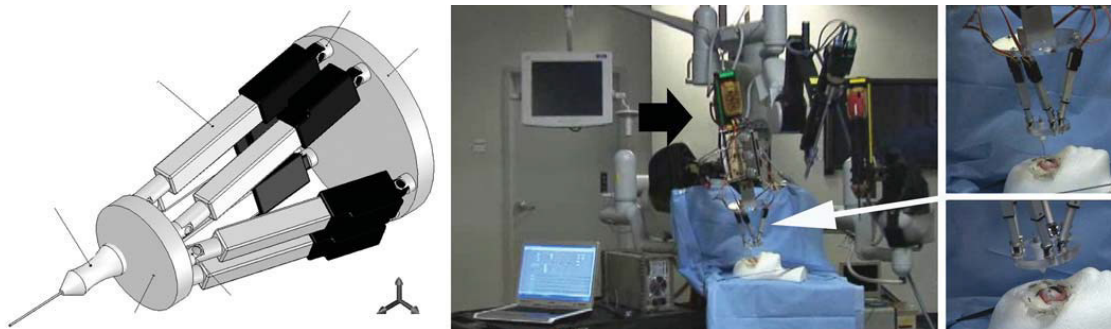


Fig. 2.4. Hexapod surgical system (HSS) integrated with the da Vinci robot. Photo credit [75].

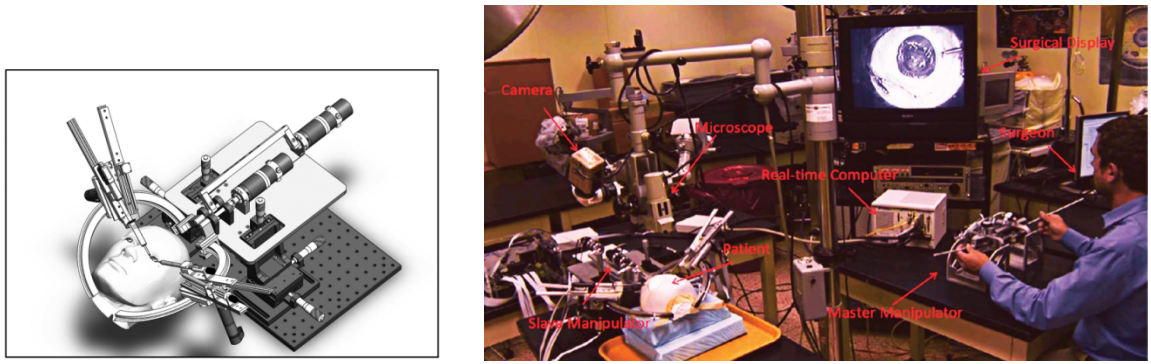


Fig. 2.5. Intraocular robotic interventional and surgical system (IRISS). Photo credit [76].

in Fig. 2.5. The system is a dedicated microsurgical platform capable of performing complete ophthalmic procedures. Feasibility was shown in both anterior and posterior segment intraocular surgery with porcine eyes [76].

Similar dual arm systems have also been proposed for retinal microvascular surgery [77], [78]. The latest development incorporates an 11-DOF robotic system composed of a 6-DOF parallel robot, a 3-DOF stent deployment robot providing intraocular dexterity, and a 2-DOF differential wrist. In addition, an intraocular OCT probe was integrated in the system for image guidance. Membrane peeling and B-mode scans were demonstrated in an eye phantom; OCT-based visual servoing still remains as future work [78].

Japanese researchers have also developed a robotic system for vitreoretinal microsurgery [79], [80]. Nakano *et al.* introduced a master-slave robotic system using a parallel mechanism to obtain high stability and accuracy of instrument positioning [79]. Due to the interference of links with rotational movement, they separated the rotational degrees of freedom around the tool by placing a redundant rotational mechanism on the end-effector. However, the workspace of the system was still narrow for various uses in ophthalmological surgery, which led to the development of a new prototype [80]. The new robotic instrument directly controls 2-DOF angular motion using a pair of spherical guides and 3-DOF positioning is allowed using translational stages. Once the position of a tool is set at the entry point of the eye by translation, the orientation of the tool is then defined by the 2-DOF angular stages and axial motion along the tool is independently controlled; the tool can also be rotated around the axis for specific usages. In addition to the evaluation of pointing accuracy, the feasibility of creating posterior vitreous detachment (PVD), retinal vessel sheathotomy (RVS), and retinal vessel microcannulation also were evaluated in porcine eyes *ex vivo*.

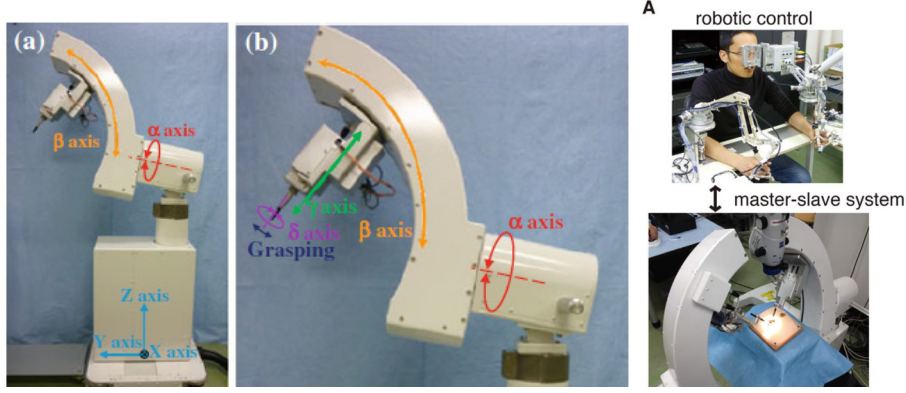


Fig. 2.6. Microsurgical robotic system for vitreoretinal surgery. Photo credit[4].

## 2.2.2 Cooperative Robots

The development of a cooperative robot, the Steady Hand, for intraocular surgery has been presented by the JHU group [20], [21], [81]. Mitchell *et al.* presented a small steady-hand manipulator (Eye Robot 1) using a force/torque sensor, which provides an arm with 5-DOF motion: tilt and roll mechanisms on a 3-DOF translational stage. The manipulator was tested on a biological model with the chorioallantoic membrane of a chicken embryo and showed reliable performance to cannulate veins successfully. From the extensive investigation of the Eye Robot 1, a new generation of the Eye Robot (Eye Robot 2) has been introduced to overcome the limitations of the previous prototype [81]. Given the modification of the geometric design and operating mechanisms, the Eye Robot 2 incorporates both a significantly improved manipulator and an integrated micro-force-sensing tool.

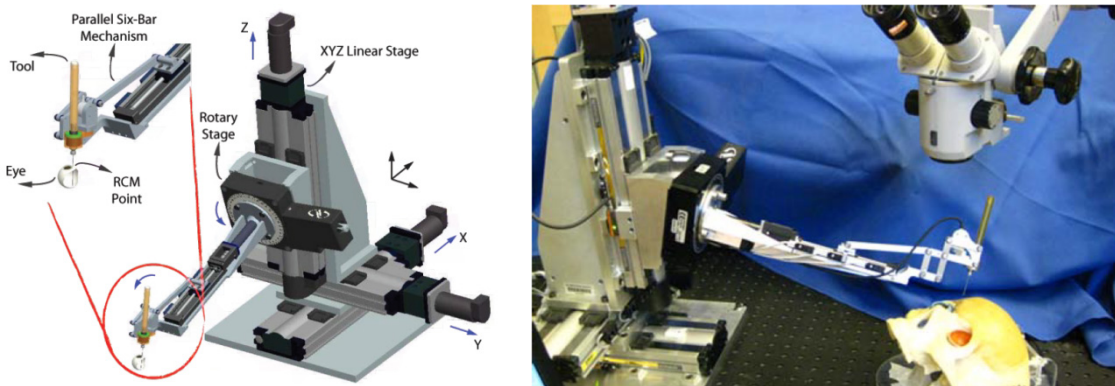


Fig. 2.7. New Steady Hand eye robot for vitreoretinal surgery. Photo credit [81].

### 2.2.3 Handheld Robots

The development of a handheld instrument for microsurgery has been primarily led by our group (CMU) since a handheld micromanipulator, Micron, was first completely presented in 2003 [82]. The first prototype presented adaptive cancelling of physiological tremor for improved precision in microsurgery [82]. The instrument incorporated a 3-DOF manipulator based on piezoelectric stack actuators and a 6-DOF inertial sensing module. In addition, tremor is modeled online using the weighted Fourier linear combiner (WFLC) [83] for active cancellation. However, the instrument is quite heavy for handheld operation because it deploys seven piezoelectric stacks in series to provide a desirable magnitude of motion. To reduce the cost and weight of the handheld device, mechanical amplification on the actuation was adopted in the second prototype [84], which allowed Micron to feel more like existing passive instruments. Nevertheless, satisfactory operation could not be achieved since the complex mechanical design of joints and moving parts led to degraded performance. Although a flexure-based manipulator was also introduced to address this issue [85], it still suffered from imprecision in fabricating parts, resulting in a smaller workspace than as designed. Furthermore, it was not equipped with an embedded sensing module, so that reflective markers had to be attached to the tool for optical tracking of the tool tip. As a descendent of Micron, a similar flexure-based handheld instrument called '*Itrem*' was later introduced as shown in Fig. 2.8 [86]. It incorporates an inertial sensing module that is strategically placed to improve the sensing resolution [87].

During the course of development, it is found that motion must be suppressed at frequencies that are well below 10 Hz, lower than could be accurately detected with the inertial sensors, in order to achieve useful accuracy improvement in microsurgery. Hence,

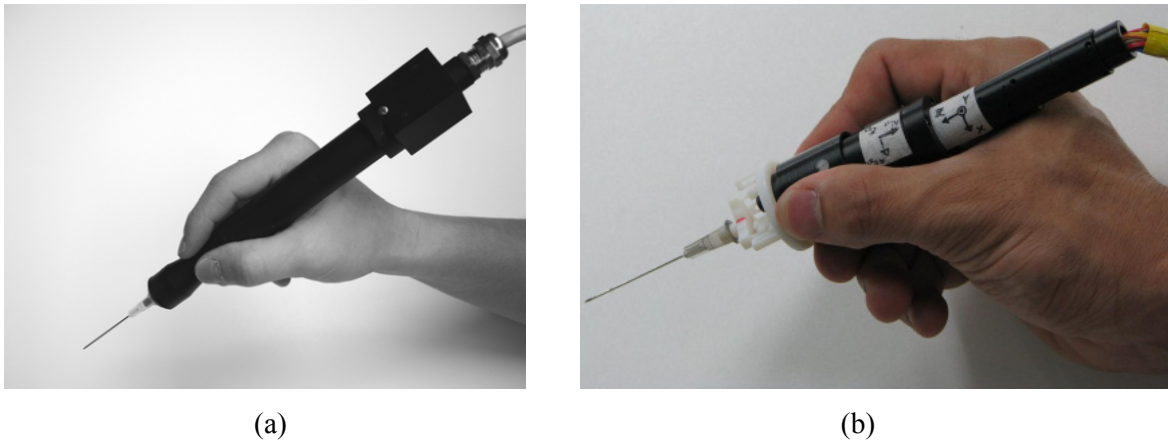


Fig. 2.8. (a) Initial Micron prototype. (b) *Itrem*. Photo credits [84], [87].

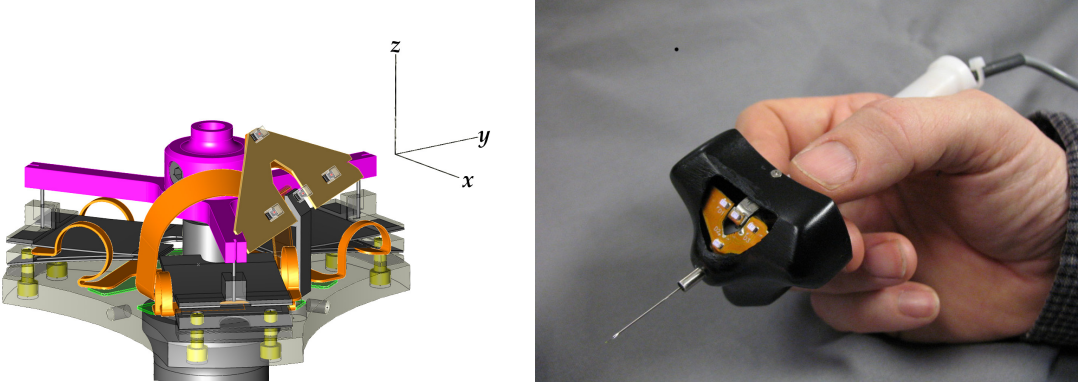


Fig. 2.9. 3-DOF Micron. Photo credit [23].

considerable modification was made in a new design of Micron as shown in Fig. 2.9, in terms of actuation, sensing, and control [23]. First, it deployed piezo-biomorph actuators on a large base to increase the range of motion, yielding a few millimeters of transverse motion. In addition, the inertial sensing module was replaced with a custom-built optical tracking system (Apparatus to Sense Accuracy of Position, or “ASAP”) capable of accurately detecting lower frequencies than the inertial sensors can detect, allowing closed-loop control of the device. This platform is capable of active tremor cancelling as well as motion scaling for fine manipulation. These subsequent developments enabled Micron to demonstrate a significant quantitative improvement in handheld accuracy.

A few other groups have recently introduced handheld micromanipulators for cancelling hand tremor [88], [89]. However, these platforms seem premature yet to perform handheld operation; benchtop tests only were conducted, with simulated signals. Saxena *et al.* adopted a disc-shaped IPMC (ionic polymer metallic composite) actuator and a commercially available IMU, for realizing a highly lightweight handheld instrument. However, the degrees of freedom are still limited to one for transverse motion. Another platform based on a linear delta manipulator was also proposed, using three voice coil motors (VCMs) [89]. Although the actuators used are capable of allowing a large range of motion due to the large displacement of the VCMs (noted as about 5 mm), no sensors are integrated in the instrument for detecting hand motion; it is only equipped with linear encoders for controlling the actuators.

Recently, a new type of a handheld manipulator was introduced, utilizing OCT-depth information as position feedback for stabilizing the instrument [90]. Although the actuation is limited to 1-DOF axial motion, it demonstrated its potential for OCT-guided servoing. In addition, haptic force feedback for a handheld instrument has been studied to deliver

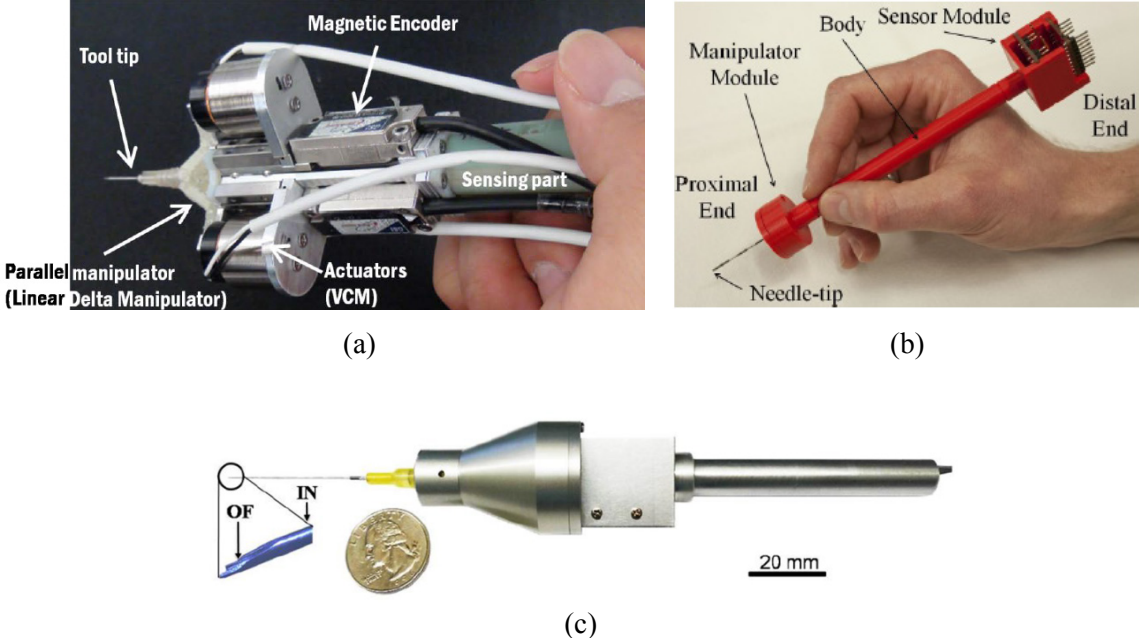


Fig. 2.10. Other handheld manipulators: (a) Chang *et al.* [89], (b) Saxena *et al.* [88], and (c) Song *et al.* [126].

magnified force to an operator and increase force perception, in particular for microsurgery [91], [92]. Since a handheld platform is not grounded to any fixed base, these systems deployed a force sensor on a tool tip and an actuator on a brace to realize haptic force feedback. Later, a handheld platform featuring both motion compensation and force feedback was also introduced [93]. Hence, the force feedback was delivered to an operator's fingertip and also used to regulate the axial motion of a tool tip, using an additional actuator.

The handheld micromanipulators introduced in this survey are summarized in Table 2.1.

TABLE 2.1. COMPARISON OF HANDHELD MICROMANIPULATORS

Description	Actuator	DOF	Sensor	Range of Motion (mm)	Overall Dimension (mm)	Weight (g)	Features
Riviere <i>et al.</i> , 2003 (Micron)	Piezoelectric	3	IMU	$0.56 \times 0.56 \times 0.1$	$\varnothing 22 \times 180$	170	No mechanical amplification.
Ang <i>et al.</i> , 2004 (Micron)	Piezoelectric	3	IMU	$0.56 \times 0.6 \times 0.1$	$\varnothing 20 (16^a) \times 180$	100	
Choi <i>et al.</i> , 2005 (Micron)	Piezoelectric	3	Optical tracking <sup>b</sup>	$0.35 \times 0.43 \times 0.08$	$\varnothing 22 \times 58.5$	-	Flexure-hinge based.
MacLachlan <i>et al.</i> , 2012 (Micron)	Piezo-biomorph	3	Optical tracking	$2.0 \times 2.0 \times 0.4$	$\varnothing 50 (14^a) \times 120$	-	Fully closed loop control. Semiautomated operation.
Latt <i>et al.</i> , 2009, (ITrem)	Piezoelectric	3	IMU	$0.4 \times 0.4 \times 0.05$	$\varnothing 22 \times 189$	75	Compact IMU.
Saxena <i>et al.</i> , 2013	IPMC <sup>c</sup>	1	IMU	1.0	$\varnothing 27 (13.3^a) \times 157$	23.6	Lightweight.
Chang <i>et al.</i> , 2013	VCM <sup>d</sup>	3	Encoder <sup>e</sup>	5.0 <sup>f</sup>	$\varnothing 27 (14^a) \times 60$	-	
Song <i>et al.</i> , 2012	Piezolinear	1	OCT	55 <sup>f</sup>	$\varnothing 22 \times 140$	65.0	OCT depth-guided servoing.
<b>Proposed Micron</b>	Piezolinear	<b>6</b>	Optical tracking	<b><math>04.0 \times 4.0</math></b>	$\varnothing 28.5 (20^a) \times 126$	70.0	Fully-automated operation. OCT handheld imaging.

<sup>a</sup>The narrowest dimension in the manipulator for gripping.

<sup>b</sup>It detects only the tip motion.

<sup>c</sup>Ionic polymer metallic composite.

<sup>d</sup>Voice coil motor.

<sup>e</sup>The encoders are used for controlling VCMs: none of sensors for detecting hand motion.

<sup>f</sup>The travel of actuators used is only specified.

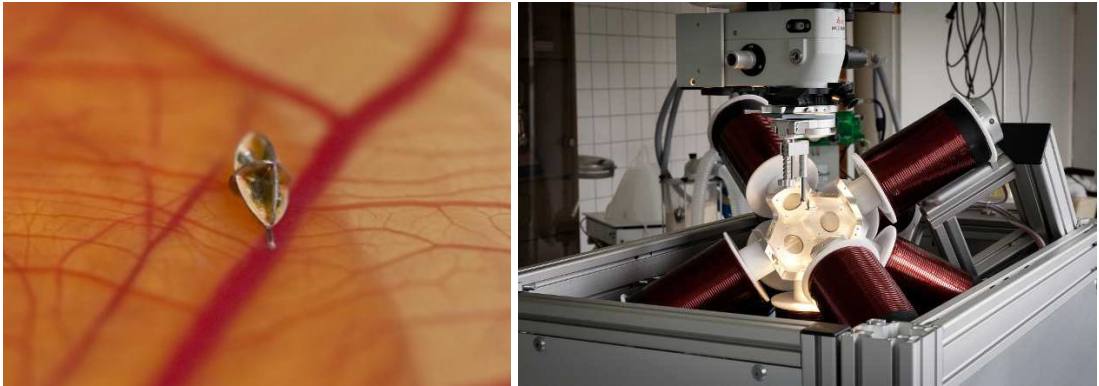


Fig. 2.11. Wireless magnetic microrobot for targeted retinal drug delivery. Photo credits [94], [96].

#### 2.2.4 Microrobot Approach

An untethered approach using a microrobot (OctoMag, presented in Fig. 2.11) has also been introduced for intraocular surgery by the ETH group [94]–[96], primarily for targeted drug delivery. Once the microrobot is injected into the eye by a syringe, the fully untethered robot can freely move through a large workspace using 5-DOF wireless magnetic control: 3-DOF position and 2-DOF orientation [95]. Its mobility and controllability were examined in different media, specifically vitreous, balanced salt solution (BSS), and silicone oil, and also demonstrated through animal experiments *ex vivo* and *in vivo* [96].

A unique micro-forceps called Microhand, mimicking a human hand, was also developed. This MEMS based gripper is pneumatically controlled, allowing grasping and manipulation of the retina [97].

## 2.3 Summary

We have reviewed robot-aided micromanipulation, specifically, for vitreoretinal surgery. The refinements of teleoperated systems for use in ophthalmic surgery have been conducted over two decades. As a result, these efforts have brought robot-assisted vitreoretinal surgery closer to real-world use although practical issues still remain to be solved.

For the handheld robot, despite its unique advantages over grounded platforms, none of the platforms has been applied in a realistic surgical environment yet due to the challenges involved in miniaturizing actuation and sensing systems while preserving a level of performance similar to that of the grounded platforms. Many demonstrations have been in either benchtop setups or simplified configurations, e.g., holding still in an open space rather than through a sclerotomy. These are primarily due to the limited degrees of freedom and small range of motion of the manipulators.

This motivates us to develop a new handheld micromanipulator that can perform under realistic environments, beyond the proof of concepts. For use of the handheld micromanipulator in vitreoretinal surgery, the new manipulator should be able to offer an RCM, as in a laparoscopic robot. In addition, the limited range of motion should be increased for numerous applications such as patterned laser photocoagulation.

### 3 HANDHELD MICROMANIPULATOR DESIGN

We propose a new Micron design providing a larger range of motion and higher degrees of freedom in a smaller package using novel linear actuators. In this chapter, we describe the development of a fully handheld micromanipulator, presented in Fig. 3.1, including the design optimization and mechanical design of a miniature Gough-Stewart platform. We also experimentally evaluate its force capability and workspace that is primarily considered in the optimization and mechanical design.

#### 3.1 Related Work

In order to realize the new manipulator, a parallel-link mechanism is preferable to a serial-link mechanism since it occupies a small volume and provides large angular displacement with high inherent stiffness [25]. Several 6-DOF parallel manipulators have already shown their potential in biomedical applications [18], [25], [75], [98]–[100]. A 6-DOF parallel micromanipulator based on the Gough-Stewart platform was introduced for retinal surgery [25], [75]. A dual structure of two 3-DOF parallel micromanipulators was also developed for cell micromanipulation [98]. In addition, Shoham *et al.* presented a smaller 6-DOF parallel micromanipulator using micromotors and embedded LVDT sensors [18]. However, these manipulators have to be mounted to a table or the skeleton of

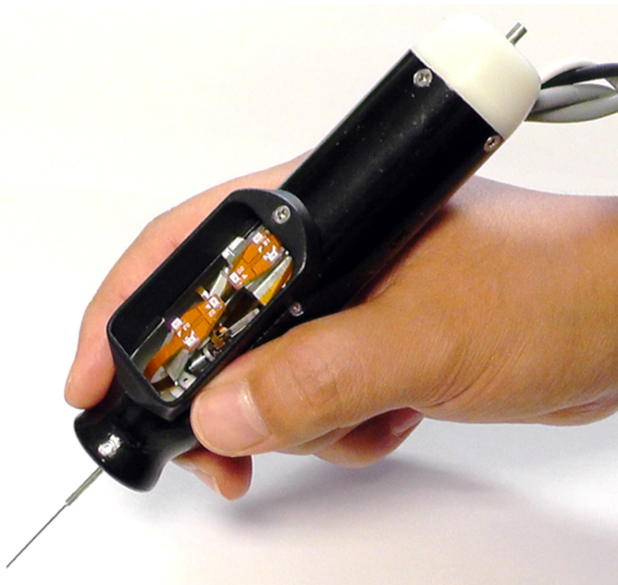


Fig. 3.1. 6-DOF handheld micromanipulator.

the patient due to their size. Manipulators presented in the literature that are of comparable size to Micron generally have only three degrees of freedom. Peirs *et al.* developed miniature parallel manipulators for steerable arms integrated in a self-propelled endoscope, based on hydraulic power. A motorized version of the manipulator was also developed, offering relatively large angular motion [99]. As for handheld operation, manipulators using piezoelectric actuators and flexure hinges for mechanical amplification have been introduced [85], [100]. Despite the mechanical amplification, the workspace of these handheld manipulators is limited to several hundred micrometers because of the small displacement of the piezoelectric stack actuators used—the factor which led to the development of the most recent 3-DOF Micron prototype [23], whose range of motion is larger, but still inadequate. In order to attain a much larger range of motion in a comparable size, an alternative actuation modality is necessary.

## 3.2 Kinematic Design

The goal is to make the instrument as narrow as possible, and in any case no wider than 25 mm. For the 6-DOF handheld micromanipulator, the Gough-Stewart platform [101], [102] is adopted, in order to take advantage of its high stiffness while still occupying small volume. In order to realize a miniature version of the parallel mechanism, several challenges should be addressed. First, the size constraint considerably limits the set of feasible actuators. Although a variety of miniature actuators has been introduced in realizing miniature mechanisms [103], [104] and some of them are commercially available, it is still challenging to obtain enough force or torque from them to provide reliable motion. For instance, micro DC motors may be adequate for the miniaturization of mechanisms in terms of size. However, they are commonly combined with high reduction gears to compensate for the low torque and also with a set of a thread and nut to convert rotational motion into linear motion, which leads to low speed as well as a complex and bulky mechanism.

For our application, we adopt the SQUIGGLE® motor (SQL-RV-1.8, New Scale Technologies, Inc., USA), a type of piezoelectric linear motor, since it is small enough (2.8 mm × 2.8 mm × 6 mm) and generates adequate force (>0.3 N at 3.3V). The motor utilizes the orbital vibration of the piezoelectric elements on it to generate linear motion of a threaded rod. Moreover, the linear stroke of the motor is adjustable to any value by selecting the length of the threaded rod, which provides us flexibility in the design and optimization of the manipulator.

### 3.2.1 Kinematics

The six degrees of freedom of the manipulator, considered in terms of the movements of interest for the microsurgical application, are as follows:

- Translation in XYZ Euclidean space at the tool tip (3-DOF);
- Translation in XY plane at a point somewhere along the tool shaft (2-DOF);
- Axial rotation of the tool (1-DOF).

The second translation tends to be constrained in robot-aided surgery to provide a fulcrum at the surgical incision point. For intraocular surgery, the desired workspace for the tool tip is a cylinder 4 mm in diameter and 4 mm long.

The inverse kinematics involves determination of the vector  $\mathbf{M}_i$  corresponding to each

link, given the position and orientation of the tool tip. The vector  $\mathbf{M}_i$  is represented by the sum of vectors  $\mathbf{OA}_i$  and  $\mathbf{OB}_i$  in (3.1). Here,  $\mathbf{O}$  and  $\mathbf{P}$  are the origins of the base (fixed frame) and the moving platform, respectively, as shown in Fig. 3.2.  $A_i$  is one end of the  $i$ th link attached on the moving platform, which is defined with respect to the origin  $\mathbf{P}$ .  $B_i$  is the other end of the  $i$ th link, at the base, defined with respect to the origin  $\mathbf{O}$ .

$$\mathbf{M}_i = \mathbf{OA}_i - \mathbf{OB}_i = \mathbf{OP} + \mathbf{PA}_i - \mathbf{OB}_i \quad (3.1)$$

In order to determine,  $\mathbf{OA}_i$  the end and the middle positions of the tool tip  $\mathbf{P}_0\mathbf{T}_e$  and  $\mathbf{P}_0\mathbf{T}_m$ , respectively, are expressed by (3.2) and (3.3) with respect to the initial origin of the moving platform  $\mathbf{P}_0$ .

$$\mathbf{P}_0\mathbf{T}_e = [\Delta d_{ex} \quad \Delta d_{ey} \quad \Delta d_{ez} + l_t]^T \quad (3.2)$$

$$\mathbf{P}_0\mathbf{T}_m = [\Delta d_{mx} \quad \Delta d_{my} \quad d_{RCM}]^T \quad (3.3)$$

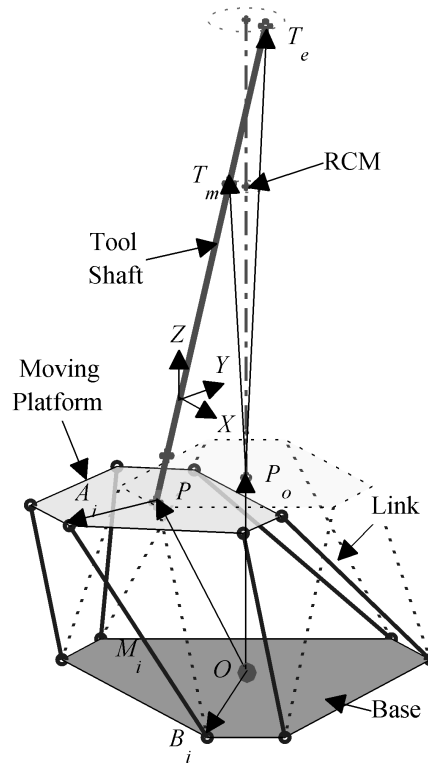


Fig. 3.2. Kinematic configuration of a 6-DOF parallel mechanism with a tool tip and a remote center of motion (RCM). The dotted lines represent the initial configuration and the solid lines a configuration with displaced tool tip and RCM.

The relative displacements from the initial positions of the tool tip are denoted by  $\Delta d_{ei}$  and  $\Delta d_{mi}$ , where the subscript  $i$  indicates each coordinate in the Euclidean space. The nominal length of the tool shaft is  $l_t$ . In addition,  $d_{RCM}$  is given by setting a remote center of motion with respect to the initial position of the moving platform. The unit vector of the tool tip  $\mathbf{u}_t$  is then defined by two positions of the tool tip:

$$\mathbf{u}_t = \frac{\mathbf{P}_0\mathbf{T}_e - \mathbf{P}_0\mathbf{T}_m}{|\mathbf{P}_0\mathbf{T}_e - \mathbf{P}_0\mathbf{T}_m|} = [u_{tx} \ u_{ty} \ u_{tz}]^T. \quad (3.4)$$

The origin of the moving platform  $\mathbf{P}$  is represented by the length of the tool and corresponding vectors  $\mathbf{OP}_0$ ,  $\mathbf{P}_0\mathbf{T}_e$  and  $\mathbf{u}_t$  in (3.5).

$$\mathbf{OP} = \mathbf{OP}_0 + \mathbf{P}_0\mathbf{T}_e - l_t \mathbf{u}_t \quad (3.5)$$

The rotation of the moving platform is then expressed by the axis of rotation and the corresponding angle. The axis of the rotation  $\hat{\mathbf{n}}_{rot}$  is regarded as the cross product of the initial vector  $\mathbf{u}_{init}$  (equivalent to the z-axis) and the current vector of the tool tip  $\mathbf{u}_t$  in (3.6). The angle of the rotation is corresponding to the angle between two vectors  $\mathbf{u}_{init}$  and  $\mathbf{u}_t$  in (3.7).

$$\hat{\mathbf{n}}_{rot} = \frac{\mathbf{u}_{init} \times \mathbf{u}_t}{|\mathbf{u}_{init} \times \mathbf{u}_t|} \quad (3.6)$$

$$\theta_{rot} = \cos^{-1}(\mathbf{u}_{init}^T \mathbf{u}_t), \quad (3.7)$$

where  $\mathbf{u}_{init}$  is  $[0 \ 0 \ 1]^T$ .

Given the angle-axis rotation, a rotation matrix,  $\mathbf{R}_{ot}^{3\times 3}$  is also defined using a matrix form of Rodrigues' rotation formula in (3.8) in order to construct a homogenous transform.

$$\mathbf{R}_{ot}^{3\times 3} = \cos \theta_{rot} \mathbf{I}^{3\times 3} + \sin \theta_{rot} \hat{\mathbf{n}}_{rot} \times \mathbf{I}^{3\times 3} + (1 - \cos \theta_{rot}) \hat{\mathbf{n}}_{rot} \hat{\mathbf{n}}_{rot}^T, \quad (3.8)$$

where  $\mathbf{I}^{3\times 3}$  is an identity matrix of size 3.

The rotation matrix is also regarded as the combination of rotations with the Tait-Bryan (yaw-pitch-roll) angles  $\alpha$ ,  $\beta$ , and  $\gamma$  with respect to the initial position in (3.9).

$$\begin{aligned} \mathbf{R}_{ot}^{3\times 3} &= \mathbf{X}(\gamma)\mathbf{Y}(\beta)\mathbf{Z}(\alpha) \\ &= \begin{bmatrix} C_\beta C_\alpha & -C_\beta C_\alpha & S_\beta \\ C_\gamma S_\alpha + C_\alpha S_\gamma S_\beta & C_\gamma C_\alpha - S_\gamma S_\beta S_\alpha & -C_\beta S_\gamma \\ S_\gamma S_\alpha - C_\gamma C_\alpha S_\beta & C_\gamma S_\alpha + C_\gamma S_\beta S_\alpha & C_\gamma C_\beta \end{bmatrix}, \quad C_\theta \equiv \cos \theta, \\ &\quad S_\theta \equiv \sin \theta \end{aligned} \quad (3.9)$$

where  $\mathbf{X}$ ,  $\mathbf{Y}$ , and  $\mathbf{Z}$  are the rotation matrices about each axis with an angle of  $\theta$ .

In particular, the angles  $\beta$  and  $\gamma$  are simply derived by (3.10) using the components of the unit vector  $\mathbf{u}_t$  with the axial rotation of the tool  $\alpha$  assumed to be zero. This is because axial rotation does not change the tool tip position, and is therefore not needed in active tremor cancellation [22]. The corresponding angles are written in (3.11).

$$\mathbf{R}_{ot}^{3 \times 3} \mathbf{u}_{init} = \mathbf{u}_t \quad (3.10)$$

$$\begin{aligned}\beta &= \sin^{-1}(u_{\alpha}) \\ \gamma &= -\tan^{-1}\left(\frac{u_y}{u_z}\right)\end{aligned} \quad (3.11)$$

Each end position  $\mathbf{OA}_i$  of the  $i$ th link on the moving platform is determined by a homogeneous transform in (3.12), where the vector  $\mathbf{OP}$  is regarded as translation of the moving platform.

$$\begin{bmatrix} \mathbf{OA}_i^{3 \times I} \\ 1 \end{bmatrix} = \begin{bmatrix} \mathbf{R}_{ot}^{3 \times 3} & \mathbf{OP}^{3 \times I} \\ \mathbf{0}^{I \times 3} & 1 \end{bmatrix} \begin{bmatrix} \mathbf{PA}_i^{3 \times I} \\ 1 \end{bmatrix} \quad (3.12)$$

The desired length of each link is finally determined by the vector of each link  $\mathbf{M}_i$  using (3.1).

### 3.2.2 Generalized Force on Link

It is essential to analyze the generalized forces acting on the links in the design of the manipulator since the actuators used are relatively weak and prone to failure due to external force on the tool tip of the instrument. For the analysis, we introduce Plücker coordinates, which represent the vector of each link as six homogeneous coordinates. The representation offers convenient tools in analyzing the kinematics of the manipulator [105]. In addition to the force analysis, it is also useful for the singularity analysis of the manipulator, being combined with the screws and wrenches [106].

Let the unit screw  $\mathbf{e}_i^{l \times 6}$  be the combination of two vectors  $\mathbf{q}_i$  and  $\mathbf{q}_{io}$  in (3.13). Here,  $\mathbf{q}_i$  represents the normalized vector of the  $i$ th link and  $\mathbf{q}_{io}$  is the cross product of  $\mathbf{PA}_i$  and  $\mathbf{q}_i$ .

$$\mathbf{e}_i^{l \times 6} = [\mathbf{q}_i \quad \mathbf{q}_{io}] = \begin{bmatrix} \mathbf{B}_i \mathbf{A}_i & (\mathbf{PA}_i \times \mathbf{B}_i \mathbf{A}_i) \\ |\mathbf{B}_i \mathbf{A}_i| & |\mathbf{B}_i \mathbf{A}_i| \end{bmatrix} \quad (3.13)$$

Given each position of a link derived by the inverse kinematics, Plücker coordinates  $\mathbf{E}$  are assigned by horizontally cascading each unit screw  $\mathbf{e}_i$  in (3.14).

$$\mathbf{E}^{6 \times 6} = \begin{bmatrix} \mathbf{e}_1^T & \mathbf{e}_2^T & \mathbf{e}_3^T & \mathbf{e}_4^T & \mathbf{e}_5^T & \mathbf{e}_6^T \end{bmatrix} \quad (3.14)$$

The velocity kinematics is completely described in (3.15) using the relationship between the generalized velocities of the links  $\dot{\theta}$ , the twist of the moving platform  $\Omega$ , Plücker coordinates  $E$  and the matrix  $G$ .

$$E\Omega = G\dot{\theta}, \quad (3.15)$$

where  $\dot{\theta}$  is composed by  $\begin{bmatrix} \dot{\theta}_1 & \dot{\theta}_2 & \dot{\theta}_3 & \dot{\theta}_4 & \dot{\theta}_5 & \dot{\theta}_6 \end{bmatrix}^T$  and  $\Omega$  is  $\begin{bmatrix} V_x & V_y & V_z & \omega_x & \omega_y & \omega_z \end{bmatrix}^T$ . In the Stewart platform,  $G$  is an identity matrix since each diagonal element is the scalar product of  $q_i$  and the vector of the generalized coordinate  $\theta_i$  that also lies on each link. For any configuration with the full rank of the matrix  $E$  the generalized force  $F$  is derived as (3.16) upon an external wrench  $R$ .

$$F = G [E^T]^{-1} R, \quad (3.16)$$

where  $R$  is  $\begin{bmatrix} F_x & F_y & F_z & M_x & M_y & M_z \end{bmatrix}^T$ .  $F$  is then represented as  $[f_1 \ f_2 \ f_3 \ f_4 \ f_5 \ f_6]^T$ , where  $f_i$  is the signed magnitude of the force acting along each link.

### 3.2.3 Design Optimization

Our primary goal is to design the manipulator to be compact as possible for easy grip and also robust to external disturbance during operation, particularly transverse loading at the entry point through the sclera. This factor drives the optimization of geometric parameters such as diameters of the base and moving (or “top”) platforms, and the length of the links.

Although various approaches have been introduced for optimization of the dimensions of parallel manipulators [107], [108], they primarily focus on the overall stiffness of the manipulators in order to withstand external loads and to achieve high control bandwidth. Hence, we need a new approach to consider the capabilities of actuators used in such a small manipulator. For instance, small actuators suitable for the compact package are weak in terms of force/torque. This may result in undesirable manipulation under the considerable force at the fulcrum because such actuators cannot overcome external force. Hence, to maintain the position of the tool tip even under heavy side load, the force distributed on each actuator by force and moment equilibrium should not exceed the maximum thrust force of the actuator. Otherwise, the actuator stalls and the manipulator

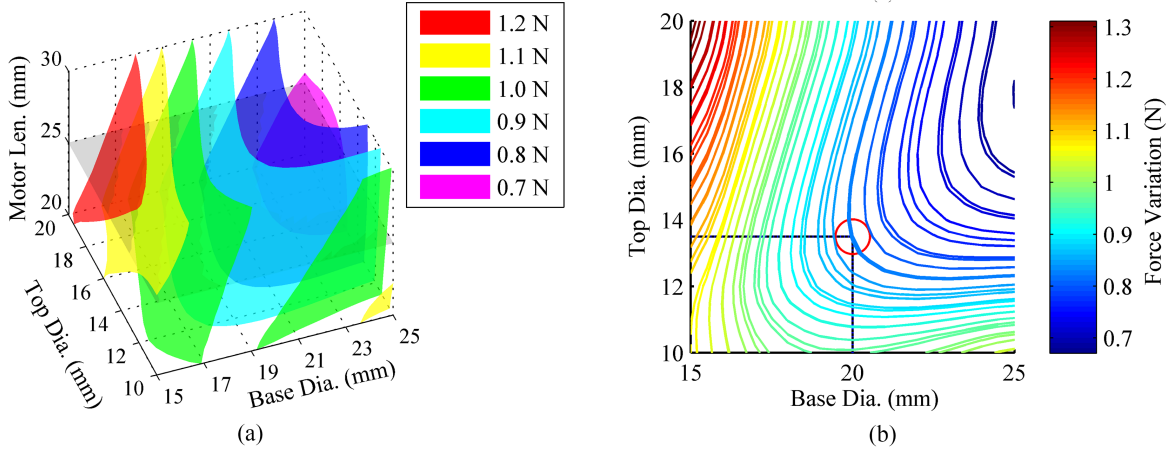


Fig. 3.3. (a) The force variation with respect to the varying geometric parameters of the manipulator for side load of 0.2 N acting at the RCM. (b) The contour of the force variation with respect to the base and the top diameters at a link length of 25 mm. The red circle indicates the optimal diameter of the moving platform when the upper bound of the base diameter is set at 20 mm.

cannot cancel hand tremor. Moreover, the design space is more limited in the case of the small manipulator since the actuators occupy most of the volume in the mechanical design of the manipulator.

The optimal dimension for the manipulator is therefore determined by the expected side load and the available thrust force. Specifically, the distributed force acts as either compression or tension to each link, depending on the direction of the side load. Considering transverse application of force to the tool tip in all possible directions, the external wrench  $\mathbf{R}$  defined in (3.16), is rewritten in terms of a certain side load  $F_s$  and application angle  $\theta_s$  in (3.17).

$$\mathbf{R} = [F_s \cos \theta_s \quad F_s \sin \theta_s \quad 0 \quad 0 \quad 0 \quad 0]^T \quad (3.17)$$

We also define link force variation  $f_{var}$  using (3.16) upon the geometric parameters such as the diameters of the base and top and the nominal length of the links, denoted by  $D_b$ ,  $D_t$ , and,  $L_m$ , respectively in (3.18).

$$f_{var}(D_b, D_t, L_m, F_s, \theta_s) = |\max(f_i) - \min(f_i)|, \quad i = 1 \dots 6 \quad (3.18)$$

Given the side load and application angle, the force variation can be minimized by appropriate selection of the dimensions of the manipulator. Fig. 3.3(a) shows how the force variation (3.18) behaves given different geometric parameters when the transverse load is

0.2 N (determined from previous experiments [109]) and the angle of application varies from  $-\pi$  to  $\pi$  around the RCM. For example, given a link length of 25 mm, larger base diameter and corresponding top diameter offer the minimum force variation, as shown in Fig. 3.3(b).

In order to find the optimal dimension for the manipulator, the cost function should minimize the force variation on the links at a nominal tool pose in (3.19), where the same amount of side load is applied with all angles of application used for simulating Fig. 3.3.

$$\arg \min_{D_b, D_t, L_m} (f_{var}(D_b, D_t, L_m, F_s, \theta_s) |_{F_s = 0.2 \text{ N}, \theta_s \in [-\pi, \pi]}) \quad (3.19)$$

Since the optimization tends to approach the upper limit of the base diameter, we set the largest feasible diameter of the base to 20 mm, taking into account the grip of the handheld manipulator. The parameters are optimized using a numerical approach based on the ‘active-set’ algorithm utilizing the Matlab™ function ‘fmincon.m,’ which performs constrained nonlinear multivariable optimization. It can thus include not only upper and lower bounds of the parameters but also nonlinear inequality constraints. The additional constraints are important in the design for real-world use. For instance, moving components such as the links and the top must avoid collision with the housing. Moreover, the minimum allowable link length is a function of the other geometric parameters because it is determined by the need to reach the predefined workspace.

The refined approach imposes two types of nonlinear inequality constraints on the optimization, driven by the predefined workspace. First, the largest displacement of the moving platform in the desired workspace is considered, to prevent the moving platform from going beyond the outer diameter of the base.

- $d_{ur} < \frac{D_b}{2}$  and  $d_{lr} < \frac{D_b}{2}$ ,

where  $d_{ur}$  and  $d_{lr}$  are the longest distances from the central axis of the manipulator to any edge of the moving platform at the upper and lower limit of the workspace, respectively. The second is to simultaneously update the lower bound of the link length while running the optimization, with respect to the nominal length and travel of the link. Since any parameter related to the workspace is not encoded in the cost function, the nominal length is regulated by this constraint in order to reach the entire workspace. Hence, we first introduce the minimal length of the link  $l_0$ , contributed by mechanical components such as a bearing assembly, which will be described later. The value is set to be 17.5 mm for the optimization. The longest and shortest lengths of the link are also defined by the linear

mechanism as  $l_0 + 2l_s$  and  $l_0 + l_s$ , where  $l_s$  is the total available travel of the link. Given any nominal length of the link during iteration, the maximum length of the link  $l_{\max}$  required to reach the workspace must be less than or equal to the longest length,  $l_0 + 2l_s$  and vice versa.

- $l_{\max} \leq l_0 + 2l_s$  and  $l_{\min} \geq l_0 + l_s$

The optimization yields a top diameter of 13.3 mm and a link length of 25.1 mm at the upper bound of the base diameter, 20.0 mm, with force variation of 0.83 N. The amount of the force variation is acceptable with the range of the thrust force of the motor selected,  $\pm 0.5$  N. The total travel of the linear motors is calculated to be 5.3 mm for covering the cylindrical workspace that we define.

### 3.2.4 Workspace Analysis

Given the optimization result, the reachable space of the manipulator is determined by applying pivoting motion about an RCM that is 35 mm above the moving platform. The space is fundamentally limited by the available travel of the link. Fig. 3.4(a) depicts the reachable space in red for a travel of 5.3 mm derived from the optimization. The required cylindrical workspace shown as the blue in Fig. 3.4(a) is entirely covered by the reachable space.

Furthermore, we investigate the workspace with respect to the amount of side load that

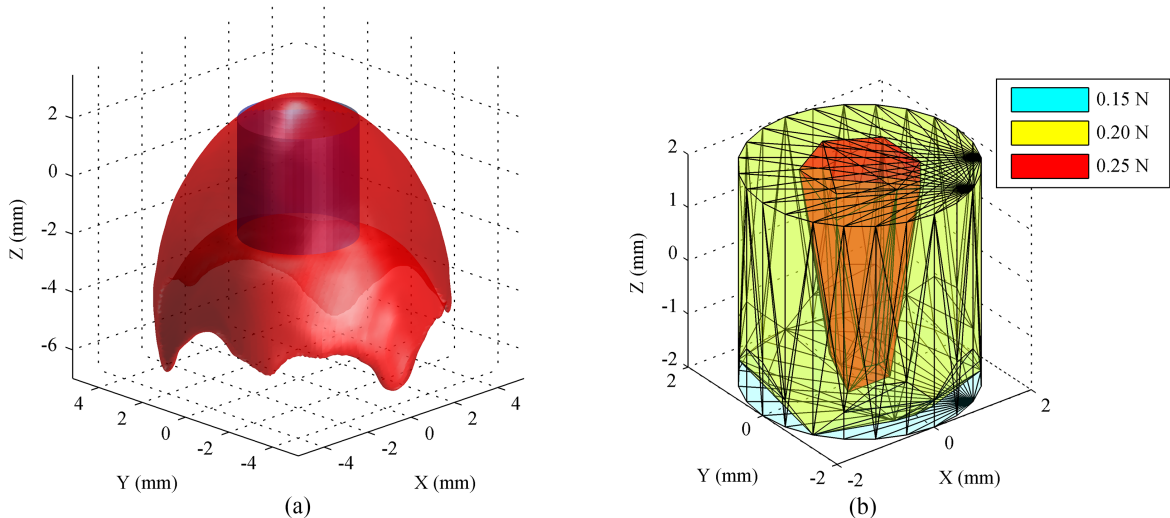


Fig. 3.4. (a) Reachable space (red) obtained by pivoting the tool tip around a predefined RCM. The cylinder (blue) inside the space indicates the desired workspace. (b) The reachable space depending on applied side load.

the manipulator can tolerate. In order to sustain the load, each motor should be able to support the axial load produced by the distribution of the side load. This is tantamount to regarding the stall force of the motor as the primary constraint in the optimization. Fig. 3.4(b) illustrates the available workspace with respect to the varying side loads from 0.15 to 0.25 N. The load can be tolerated up to 0.20 N in most of the cylindrical workspace, the exception being small regions near the workspace boundary, visible in Fig. 3.4 (b). Although the higher load shrinks the available space, the design bears the load up to 0.25 N in the desirable workspace for canceling hand tremor. Beyond the load of 0.30 N, available workspace does not exist because the stall force of the actuator is assigned to be  $\pm 0.5$  N.

In addition to the side load capability, desired workspace of the manipulator has also been analyzed for singularities, which may be encountered in such closed-loop kinematic chains [110]. Given the velocity kinematics (3.15), the manipulator undergoes a singularity if the determinant of either the matrix  $G$  or  $E$  is zero. However, the matrix  $G$  is uniquely defined as an identity matrix in our platform because the inverse kinematics provides a unique solution for the links in the relatively small workspace without rotation about the tool tip. Hence, non-zero instantaneous motion does not occur along active links when the moving platform is fully locked [106]. The matrix  $E$  also has full rank within the designated workspace, as it provides non-zero determinants during a grid search. This is led by setting the distance between the ends of adjacent links to be the smallest possible value; singularities can occur when the screw axes intersect or are parallel to each other [106]. As a result, the manipulator does not yield undesired and uncontrollable motion when no motion is introduced on the links.

### 3.3 Mechanical Design

#### 3.3.1 Miniature 6-DOF Manipulator

We built a miniature 6-DOF manipulator based on piezoelectric linear motors as shown in Fig. 3.5, which allows maneuverability in the desired cylindrical workspace while withstanding side loads up to 0.25 N. The manipulator is composed of the top (Delrin), base (aluminum), and six legs incorporating the piezoelectric linear motors.

In order to use the linear motor in our platform, it is essential to incorporate a miniature bearing assembly that decouples the pure linear motion from screw motion combined with translation and rotation on the threaded rod. The assembly includes a miniature bearing (681h, Dynaroll Corp., USA; 1.0 mm thickness × 3.0 mm diameter), a motor coupler, a housing, and a retainer as shown in Fig. 3.6(bottom).

Two mechanical stops limit the travel of the screw, in order to protect the manipulator from dismantling itself, and to avoid becoming locked by the threaded rod at the extremity of travel. One stop is located at the free end of the screw. This part is made of PTFE (Polytetrafluoroethylene), a soft and low-friction material, since the stopper is rotating as it contacts the motor body. The retainer doubles as an upper stop, preventing the motor coupler from being fastened onto the motor body like a screw head.

The upper and lower ends of the link are connected to the moving platform and the base by flexure hinges (#1-0 polypropylene suture). These feature smaller size and less friction than ball/universal joints [100], and are adequate given the small angular range of motion.

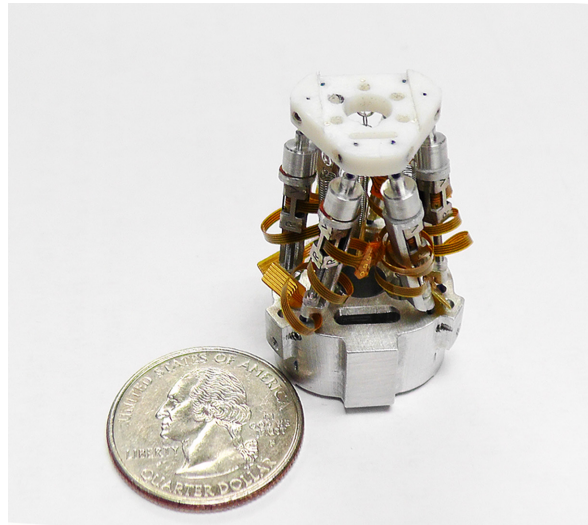


Fig. 3.5. Miniature 6-DOF manipulator, compared with a US quarter.

Within the designated workspace, the maximum angular displacement of the flexure hinge is 10.9° and the corresponding stress is 20.8 MPa for a length of 2.5 mm, which is less than the yield stress of polypropylene (30.3 MPa).

A certain amount of preload on the SQUIGGLE® motors is required for proper operation, as it avoids backlash that would otherwise result from the loose fit between the threaded rod and the actuated “nut.” To provide this preload, three tension springs are vertically aligned from the base to the moving platform. The minimum stiffness that avoids backlash is desirable in order to minimize variation of preload across the workspace, and to avoid using up the force capability of the motors just to overcome the preload. We opted for a spring with stiffness of 28.2 mN/mm (CI 010EF 14S316, Lee Spring, USA).

Each link weighs 0.3 g and the entire weight of all moving parts is only 2.3 g. It is consequently light enough to be free from degradation in dynamic performance due to excessive mass. The mechanism has an overall diameter of 23 mm and a height of 37 mm, with total weight of 14.4 g.

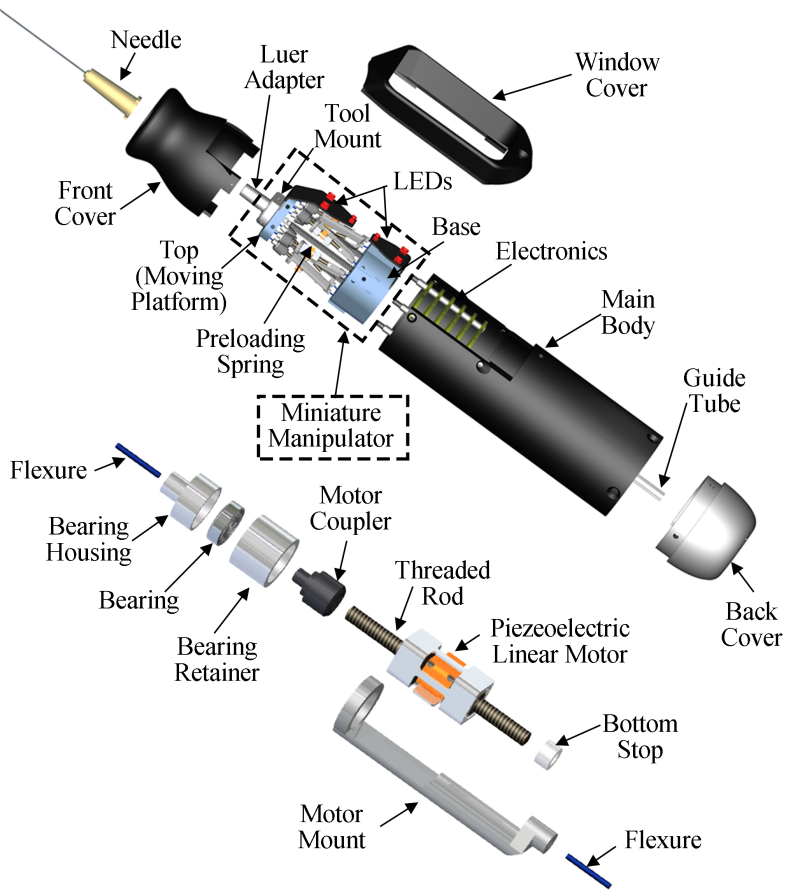


Fig. 3.6. Exploded view of the handheld manipulator assembly (top) and the linear actuation module (bottom).

### 3.3.2 Handheld Manipulator Design

For the control of the manipulator, we adopted a custom-built microscale optical tracking system, “ASAP” (Apparatus to Sense Accuracy of Position) [111]. Compared to previous Micron prototypes incorporating inertial sensors [82], [87], [112], the optical tracking system is preferable in terms of size, accuracy, and speed. For good performance, we found that motion must be suppressed at frequencies below 1 Hz, which is lower than could be detected with the inertial sensing system in [82]. In addition, inertial sensing leads to drift in position measurement, which must be addressed with either sensor fusion or recalibration of sensors [112].

The manipulator is equipped with two sets of infrared LEDs, in order to enable optical tracking of the position and orientation of both the tool tip and the handle. Three LEDs are

mounted to the moving platform and the other three are affixed to the handle (the LEDs are visible as small white blocks in Fig. 3.1). The position sensitive detectors (PSD) sense the differently modulated signals using frequency domain multiplexing and provide an analog position measurement of the centroid of each light source [111]. Consequently, the detectors allow each LED position to be triangulated in three dimensions and then the poses of the tool tip and handle are fully recovered from the position of each triad of LEDs [23]. The poses are acquired at a sampling rate of 1 kHz over a 27 cm<sup>3</sup> workspace, with less than 10 μm RMS noise [111]. A PCB (printed circuit board) stack of six layers is attached to the bottom of the manipulator. The three layers of the PCB stack closest to the base of the manipulator drive the motors, which communicate with a main controller via inter-integrated circuit (I2C) protocol. The remaining two layers are used for driving the LEDs for ASAP measurement. The last PCB routes the power and control signals to all upper PCBs.

The handle comprises a front cover, a window cover, a main body, and a back cover as shown in Fig. 3.6(top). The front cover provides an ergonomic grip. In order to balance the overall weight of the handle, the front cover and the back end were made of aluminum and Delrin, respectively, by CNC machining. The window cover was designed to fully allow LED light emission and protect the moving LEDs from being touched. The manipulator also incorporates a male Luer-Slip connector with a tool mount to accommodate conventional hypodermic needles. For other applications, the adaptor is replaceable with a variety of end-effectors such as a micro-pipette or laser probe.

The assembled instrument is 28.5 mm in diameter and 126 mm long, excluding the end-effector attached to the Luer-Slip adaptor. The total mass is 70.0 g, with the center of mass near the geometric center of the handle. Fig. 3.1 presents the fully assembled manipulator. The specifications of the 6-DOF Micron are summarized in Table 3.1.

TABLE 3.1. SPECIFICATION OF 6-DOF MICRON

Description	Specification
Overall dimension <sup>a</sup>	$\varnothing 28.5 \times 126$ mm
Total weight	70.0 g
Miniature manipulator	$\varnothing 23.0 \times 37.0$ mm (14.4 g)
Workspace <sup>b</sup>	$\varnothing 4.0 \times 4.0$ mm (cylindrical workspace)
Degrees of freedom	6
Side load capability <sup>c</sup>	up to 0.25 N
Actuator	Piezoelectric linear motor (SQUIGGLE® SQL-RV-1.8) A custom-built optical tracking system
Position sensor	(a sampling rate of 1 kHz over a 27 cm <sup>3</sup> workspace, with less than 10 $\mu$ m RMS noise)

<sup>a</sup>The dimension is for the entire housing, excluding the tool tip.

<sup>b</sup>The workspace is defined at the end of the tool tip with a fixed RCM.

<sup>c</sup>The maximum value is allowed at the center of the workspace; the manipulator can endure the sideload up to 0.15 N over the entire workspace.

### 3.4 Control

The 6-DOF Micron is primarily controlled in link-length space using the inverse kinematics derived in the kinematics section; the goal position and current position of the tool tip are converted to six link-lengths by the inverse kinematics. Accordingly, we can define the error in each link in terms of length, which is subject to PID control. Fig. 3.7. Micron system architecture. For the feedback control of the manipulator, the goal position and current position are defined in terms of six link-lengths via inverse kinematics. Any undesired motion is regarded as a control disturbance, and the errors in the links are regulated by a PID controller. Fig. 3.7 presents the overall architecture of 6-DOF Micron, including a control scheme where the hand tremor is regarded as a control disturbance. Given the link errors, the motors are controlled by applying appropriate duty cycles to motor drivers (NSD-2101, New Scale Technologies, Inc., USA) that generate ultrasonic signals.

The SQUIGGLE motors are linearized before use in order to compensate the inconsistent performance that arises due to their inherent characteristics. Since the motor relies on the indirect driving method of orbital motion of the piezoelectric membrane on the nut, rather than directly rotating the threaded rod, the performance is sensitive to the

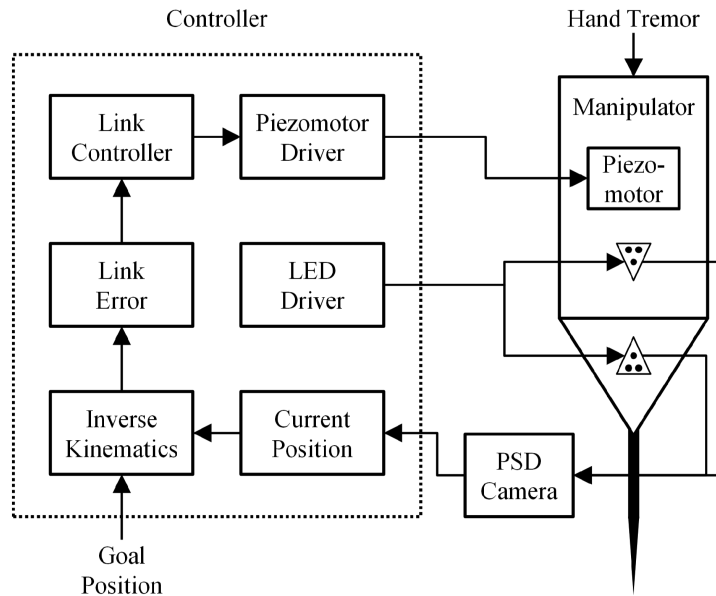


Fig. 3.7. Micron system architecture. For the feedback control of the manipulator, the goal position and current position are defined in terms of six link-lengths via inverse kinematics. Any undesired motion is regarded as a control disturbance, and the errors in the links are regulated by a PID controller.

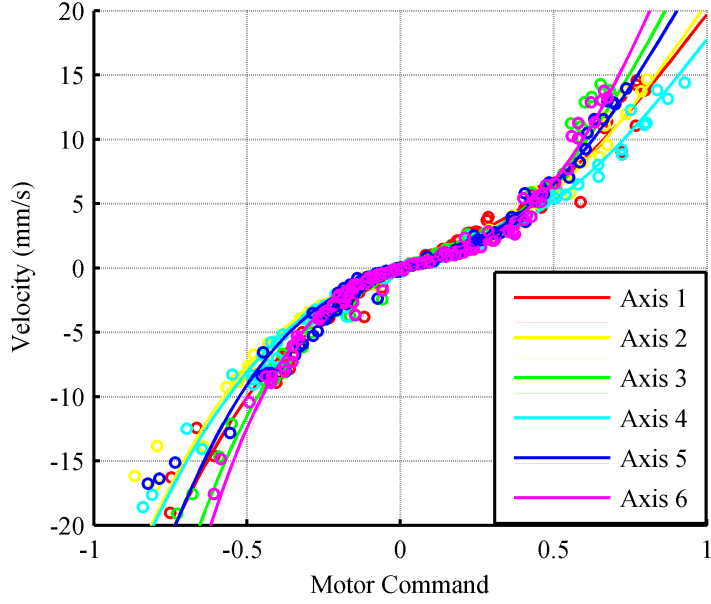


Fig. 3.8. Linearization curve: velocity with respect to motor command (duty cycle).

external environment. The displacement and speed are dependent on supply voltage, applied frequency, and load. Operating temperature also affects the resonant frequency of the piezoelectric membrane. Furthermore, the bearing assembly has a large effect on the performance because the bearing itself restrains rotation somewhat, due to friction and mating tolerances. In addition, the side load provided by bending of the flexures may be significant. These effects may become pronounced in operation of such small actuators. Lastly, the applied preload on the motor yields asymmetric motion according to the direction of the motion. It is important to quantify the variation of the motors raised by these factors and manage the variation in control.

For the linearization process, the velocity of each motor is measured while applying the varying duty cycle of the command signal. As shown in Fig. 3.8, the response is nonlinear with respect to the motor command. To calibrate the motors, we constructed a table of motor command vs. velocity by making a fifth-degree polynomial fit to data recorded while the platform moved up and down along the  $z$  axis. The amplitude of the motion was modulated from  $50 \mu\text{m}$  to  $1.5 \text{ mm}$  for  $2.5 \text{ s}$ . This process is also usable for monitoring degradation of the linear actuation module. In order to guarantee the performance of the motors, we constrain the slope of the curve at the zero command to be greater than 2 and the velocity values at  $\pm 0.8$  duty cycles to be greater than  $10 \text{ mm/s}$ . In case of a flat slope at the zero, there may be chattering on the motors when alternating the direction of motion. The lower values at the both ends of duty cycles limit the slew rate of the motors.

### 3.5 Design Validation

#### 3.5.1 Side Load Capability

We investigated the side load capability of the manipulator under varying side loads applied at an RCM which was 30 mm above the top of the tool mount as shown in Fig. 3.9(a). The range of the side loads was set from 0 to 0.3 N. A sinusoidal trajectory of  $\pm 1$  mm amplitude was applied along the x-axis for duration of 4 s; the average speed over the total 4-mm stroke in each direction was 1 mm/s. The five trials were repeated for each side load.

Fig. 3.9(b) shows the resulting sinusoidal profiles corresponding to the different side loads. RMS error with respect to the goal trajectory is summarized in Table 3.2. Although

TABLE 3.2. RMS ERRORS WITH RESPECT TO THE GOAL TRAJECTORIES FOR SIDE LOADS

Side Load (N)	0	0.05	0.10	0.15	0.20	0.25	0.30
Error ( $\mu\text{m}$ )	6	6	10	15	17	17	47

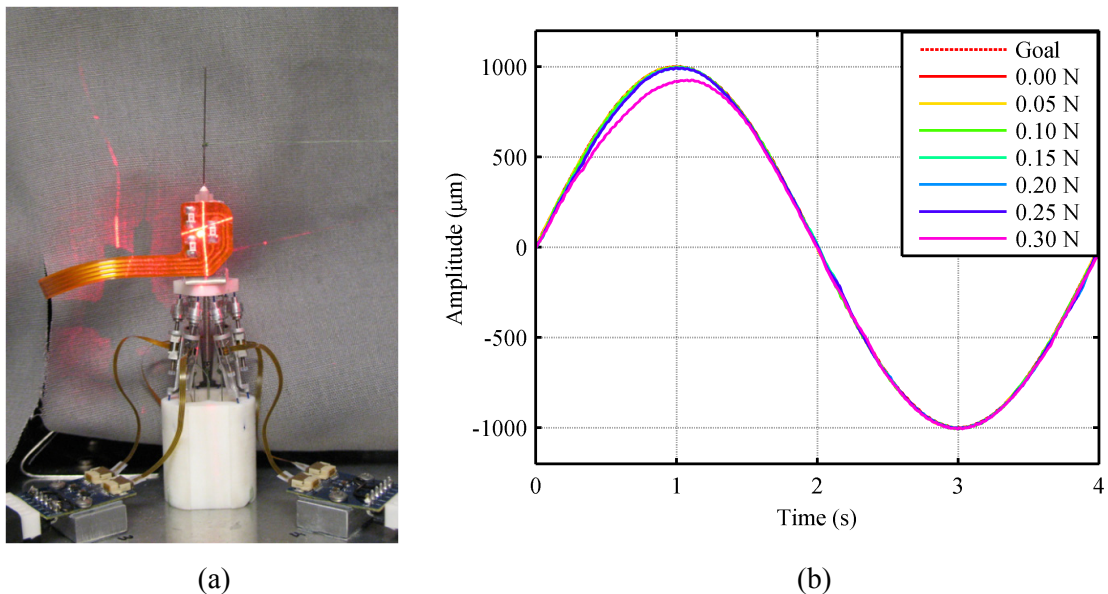


Fig. 3.9. Experimental setup for measuring side load capability (a) and resulting trajectory with respect to the amount of the side load (b).

the RMS error gradually increases until 0.25 N side load, the resulting profiles are still close to the sinusoidal goal trajectory. As the side load reaches 0.3 N, the distortion on the profile is markedly larger. These experimental results agree fairly well with the simulation done in the workspace analysis section assuming motor stall force of  $\pm 0.5$  N. Thus, we can conclude that the micromanipulator successfully tolerates side load up to 0.25 N without significant degradation.

### 3.5.2 Reachable Workspace

To demonstrate the reachable workspace of the manipulator, Fig. 3.10 shows sets of points collected at circles of different diameter and heights ranging from -2 mm to 2 mm along the z axis, in steps of 0.5 mm. Although the quality of the tracing results at the top and bottom of the workspace is somewhat poorer than the center, the manipulator covers the specified workspace.

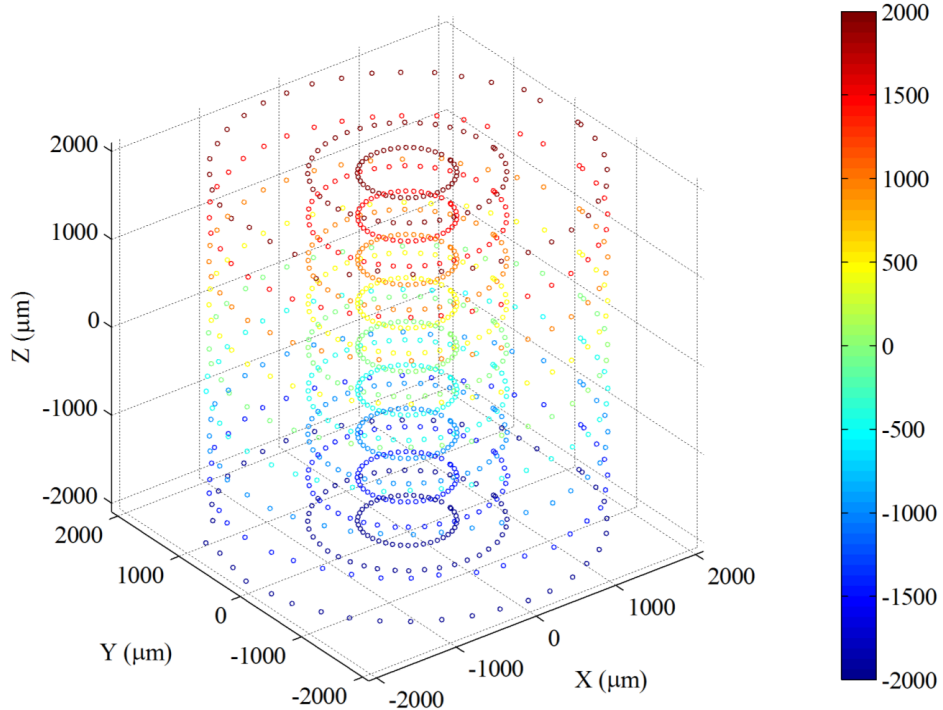


Fig. 3.10. Demonstration confirming attainment of the specified workspace.

### 3.6 Summary

We presented the design of a novel handheld manipulator. In order to realize the miniature 6-DOF manipulator, the design was optimized, focusing primarily on the amount of tolerable side load introduced at an RCM during vitreoretinal surgery. This is of particular importance for this system due to a tradeoff between the tolerable side load and the size of the manipulator (particularly the diameter), given the limited force capability of the miniature actuators used. The mechanical design and control have been refined to improve the performance of the linear actuation module by taking into account the underlying characteristics of the SQUIGGLE motor. In addition, an ergonomic handle was combined with the manipulator, enclosing also the ASAP system and embedded electronics for handheld operation. The fully handheld manipulator successfully tolerates side load up to 0.25 N without significant degradation.

In comparison to the 3-DOF piezo-bender manipulator [23], the new 6-DOF Micron offers six DOFs and an order-of-magnitude larger range of motion with adequate force capability and slew rate. It enables real-world use of the handheld manipulator, since it is capable of imposing an RCM during surgery, and also avoiding the saturation in actuation which frequently occurred in the 3-DOF Micron, hindering effective compensation.

Further experiments will also be performed on various tasks *ex vivo* and *in vivo* with multiple subjects in order to rigorously confirm the handheld performance improvement.



# 4 HANDHELD MICROMANIPULATOR PERFORMANCE

In this chapter, we investigate the performance of the 6-DOF Micron under various conditions. First, we evaluate the performance as a generic micromanipulator itself, in terms of positioning and dynamic performance, while the manipulator is firmly affixed to a solid base. Thereafter, the performance as a fully handheld micromanipulator is demonstrated in position tracking and active tremor cancellation tasks.

## 4.1 Manipulator Evaluation

### 4.1.1 Positioning Performance

Positioning performance was evaluated with respect to the five degrees of freedom that are important for the application. Axial rotation was excluded. Two angular motions were generated by pivoting about the RCM, parallel to the x and y axes, respectively. Three translations were also generated along x, y, and z axes by moving both the end-effector and the moving platform by the same amount of the amplitude. We adopted a sinusoidal profile as the reference trajectory with peak-to-peak amplitude of  $\pm 2$  mm to cover the entire workspace. To investigate the positioning performance at different velocities up to the slew limit of the motor, the duration was varied from 1.6 to 8.0 s. Given the total travel, 8 mm, the average speed varied from 1 to 5 mm/s. The tests were also repeated for five trials and averaged. The RMS error with respect to the type of motion and the applied velocity is specified in Table 4.1. Similar errors were observed for the angular and transverse motions

TABLE 4.1. RMS ERRORS WITH RESPECT TO THE PLANNED TRAJECTORIES AND VARIOUS VELOCITIES

Velocity (mm/s)	X (RCM)	X (Trans.)	Y (RCM)	Y (Trans.)	Z (Trans.)
1	8	7	6	7	11
2	8	7	7	9	22
5	16	9	14	13	43

The unit of the RMS error is  $\mu\text{m}$ .

RCM = Remote center of motion, Trans. = Transverse motion.

along x and y axes, maintaining the error at less than 10  $\mu\text{m}$  up to 2 mm/s velocity. In most cases, RMS error was doubled at 5 mm/s target velocity. RMS error was more prominent in transverse motion along the z axis than in other motions, even at lower velocities. This is primarily due to the relatively large radial play of the threaded rod in the SQUIGGLE® motor in order to generate orbital motion. It may cause transverse vibration while the moving platform is going up and down. The RMS error along the z-axis is only 14-25% of the total error, whereas the ratio in the Euclidean space would be 58 % ( $=1/\sqrt{3}$ ) if error were equal in all three axes. In other words, most error in the z-axis translation was along the x and y axes. Furthermore, for the same amplitude of tip movement, a larger movement of the motors is needed for the z-axis translation than for the other motions. Since no angular motion is introduced along the end-effector, the amplitude of the end-effector is not amplified. This requires higher slew rates on the motors to make a longer stroke in the same amount of time.

#### 4.1.2 Dynamic Performance

Fig. 4.1 shows the frequency response of the manipulator under closed-loop control in five major motions: transverse translation of the moving platform along the x and y axis, axial translation (z), and rotation about the RCM. Swept sine inputs were used to generate the frequency responses. Resulting motions were measured by ASAP and analyzed using

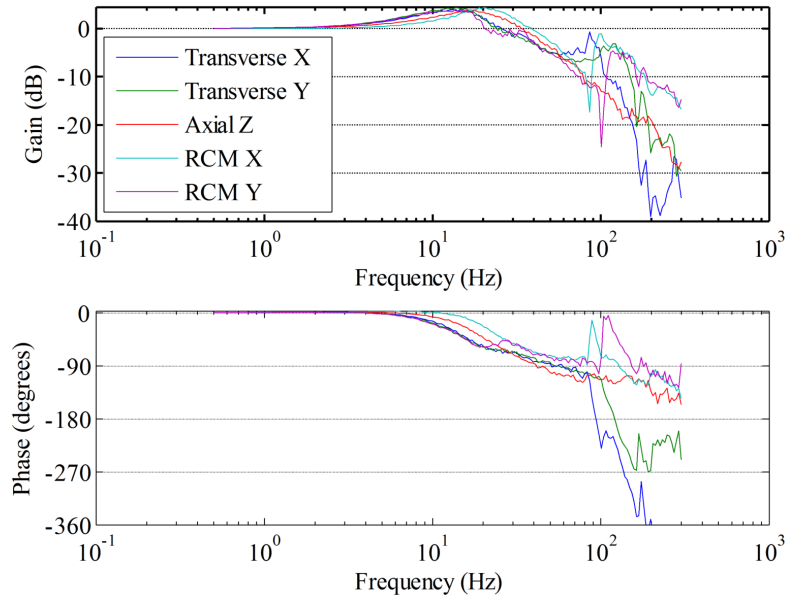


Fig. 4.1. Frequency response of the micromanipulator.

the Matlab™ system identification toolbox to generate nonparametric (spectral) frequency response estimates over the band 0.5 Hz - 300 Hz. Under closed loop control, the -3dB bandwidth was found to be around 50 Hz for the motions of interest.

## 4.2 Position Tracking Performance

The new handheld micromanipulator incorporates a new feature capable of tracking a pre-defined target or trajectory in the large range of motion, while the instrument is held in the human hand. Thus, this feature can be utilized in handheld OCT scanning and automated laser photocoagulation.

### 4.2.1 Pointing Task

A participant was asked to maintain a fixed tip position above a laser engraved rubber target for 20 s in each trial. All tasks were performed under a magnification of 25 x (Zeiss® OPMI™ surgical microscope). Once the 6-DOF Micron is activated, the current position of the tool tip is set as a goal position for control, and all disturbances from any source are rejected.

Fig. 4.2 illustrates one of the recorded trajectories for 20 s with and without the control. The RMS error and maximum error were calculated with respect to the 3D mean position of each trajectory for five trials. The RMS error drastically decreases from  $112\pm8 \mu\text{m}$  to  $12\pm2 \mu\text{m}$  on average by actively controlling the tool tip; the difference is statically significant ( $p = 3 \times 10^{-9}$ ). The maximum error is an important measure of hand tremor reduction since even a single large excursion may cause collateral damage in microsurgery. The mean maximum error is 361 and 49  $\mu\text{m}$  for the “off” and “on” cases, respectively. The

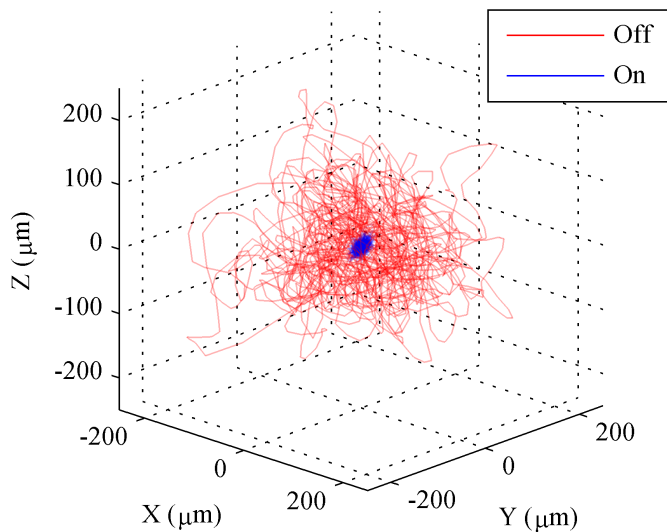


Fig. 4.2. Trajectory of the tool tip during a pointing task for 20 s. The red line indicates the trajectory without Micron assistance. The blue line is for the trajectory when Micron is activated.

difference in maximum error is also statistically significant ( $p = 7 \times 10^{-6}$ ).

The manipulator shows about 89.3% error reduction compared to unaided trials. The performance of the 6-DOF Micron is difficult to compare directly to results from other tremor-canceling devices due to the variation in hand tremor with differences in task kinematics, task ergonomics, and execution time. Nonetheless, the error-reduction ratio can be compared under similar settings. The pointing task in the 6-DOF Micron is comparable to the task done in the 3-DOF Micron with a virtual fixture which applies a constant goal position to the tool tip [113]. The result with a hard-virtual fixture control shows similar performance in tremor-reduction: 81.8% reduction in maximum error compared to unaided trials. The result is also comparable to the error reduction achieved recently by a teleoperated surgical robot operated by surgeons (from 90.0  $\mu\text{m}$  to 14.9  $\mu\text{m}$ ; an 83.6% reduction) [114].

#### 4.2.2 Circle-Tracing Task

In order to evaluate trajectory following performance during handheld operation, various sizes of circle patterns were introduced from 1 to 4 mm in diameter. Such patterns can be useful for laser retinal photocoagulation as treatment for macular degeneration in the eye [26], and for semiautomated scanning for retinal optical coherence tomography [115]. The range of velocities was varied from 1 to 5 m/s to find the most efficient velocity

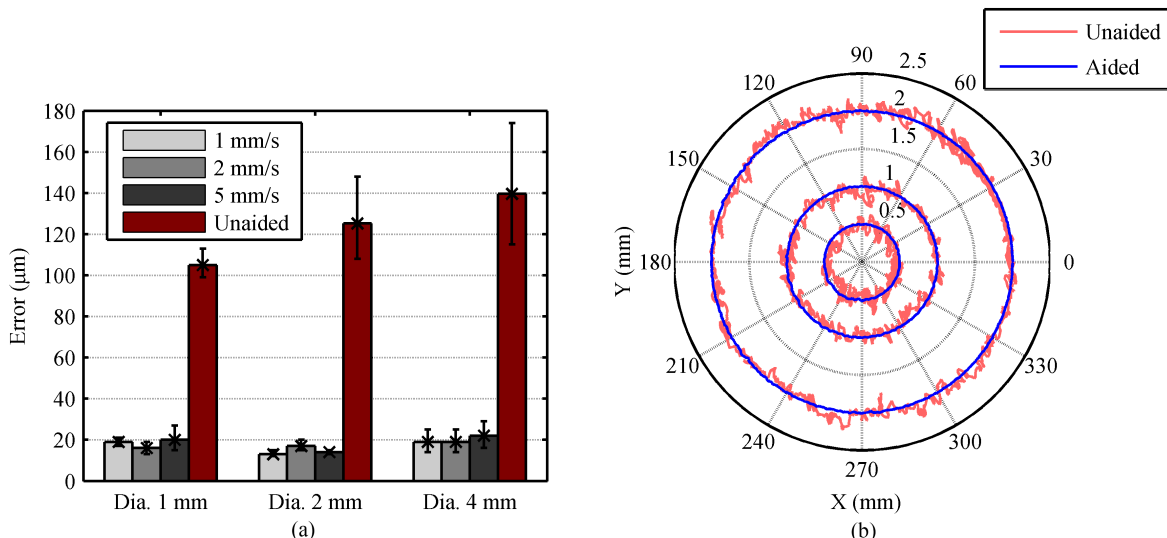


Fig. 4.3. (a) RMS error during automatic handheld circle-tracing with various circle diameters and tracking velocities. (b) Trajectory of circle-tracing for various sizes of circles.

while maintaining desired accuracy with high speed. The automated circle-tracing was also compared to manual tracing without the aid of Micron. In the manual trials, the subject traced circles as well as possible above a printed target, without velocity regulation. Fig. 4.3(a) shows the RMS error corresponding to the varying velocities and the sizes of the circles in diameter. Overall average error for five trials ranges from 10 to 20  $\mu\text{m}$  for the automated circle-tracing. The error exceeds 20  $\mu\text{m}$  under the circle tracing of 4 mm diameter with a velocity of 5 mm/s. Nevertheless, the resulting trajectory, with a velocity of 5 mm/s (shown in Fig. 4.3(b)), is still acceptable in laser surgery, given the relatively large size of a laser spot (200-300  $\mu\text{m}$ ). RMS errors in circle-tracing at 1- and 2-mm diameter are less than the error at 4-mm diameter since the manipulator operates near the edge of the workspace with large angular motion. Interestingly, the error in circle tracing of 2-mm diameter is somewhat less than the error at 1-mm diameter, possibly due to the fact that circle tracing in the smaller circle is affected by the comparable amplitude of hand tremor; i.e., the signal-to-noise ratio is lower. Compared to the automated trials, the errors in the manual tracing are significantly larger and gradually increase with the sizes of the circles, from 105 to 140  $\mu\text{m}$ . The average velocities range from 0.3–0.4 mm/s, increasing slightly with circle diameter; this is an order of magnitude slower than the automated tracing.

Accordingly, the benefit of the large range of motion in the new 6-DOF Micron was explored in fully automatic circle-tracing; the error obtained is smaller than is attainable in freehand operation [26]. The goal of these tests is to quantify the best the system is capable of, under idealized conditions, as a baseline for comparison with future performance under more realistic conditions.

### 4.3 Active Tremor Cancellation

Active tremor cancellation is the primary function of the handheld manipulator in microsurgery. To be used in real surgery, the manipulator should be able to preserve the surgeon's voluntary motion while rejecting hand tremor. Hence, we have adopted control algorithms such as lowpass/shelving filtering schemes developed in the 3-DOF Micron for this type of handheld operation [23]. Two alternatives for tremor filtering have been designed for error canceling in Micron [23]. The first is a lowpass filter with a corner frequency of 1.5 Hz. Since voluntary motion typically occurs below 2 Hz, the filter has unity gain before the corner frequency and high attenuation beyond 10 Hz in order to stabilize the instrument tip. The second alternative is a lowpass shelving filter which provides what may be considered relative motion scaling. The shelving filter features unity gain below 0.15 Hz, and gain of about 1/3 for the frequency range of 0.15 Hz to 2 Hz, with high attenuation beyond 2 Hz. The frequency response of each filter is depicted in Fig. 4.4.

In order to accurately assess the canceling performance of Micron, static and dynamic tasks were performed on a laser engraved rubber target under a board-approved protocol. All tasks were performed under magnification (Zeiss® OPMITM surgical microscope) and video was collected at 30Hz through stereo cameras attached to the microscope as shown in Fig. 4.5. The trajectory of the tool tip was overlaid on the video through custom software. 3D position data was also collected using ASAP. An algorithm was then used to align the 3D data set such that the axis corresponded to the microscope viewing plane.

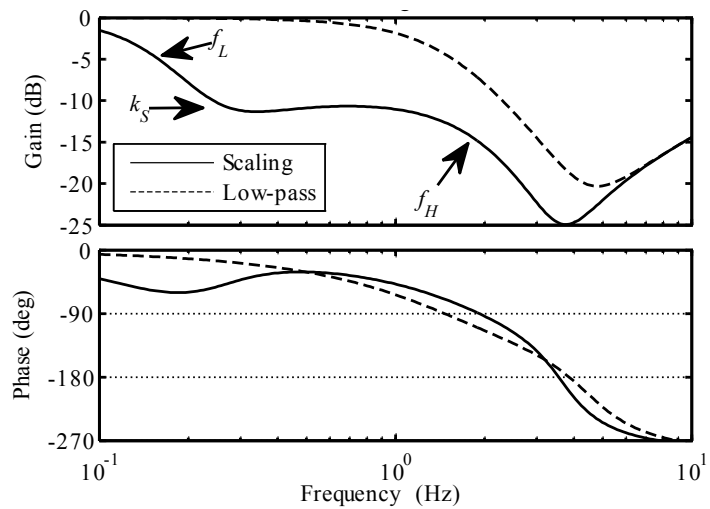


Fig. 4.4. Simulated Micron low-frequency response, hand to tip. The scaling response is labeled with the corresponding filter parameters. Photo credit [23].

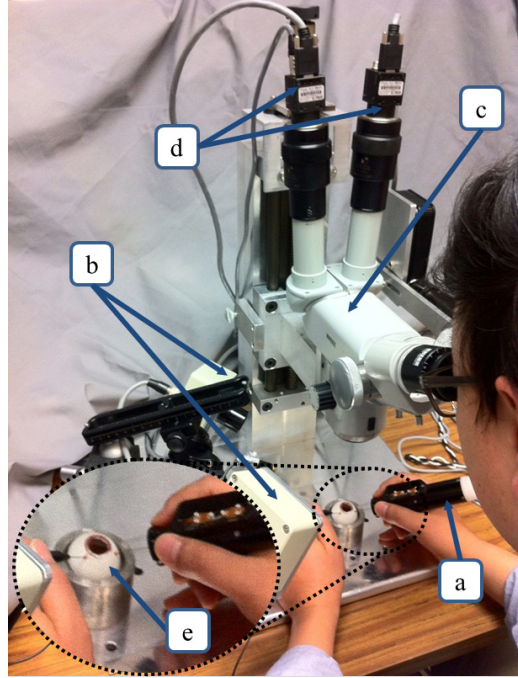


Fig. 4.5. Experimental setup. (a) Micron, (b) ASAP, (c) microscope, (d) CCD camera, and (e) eye phantom.

#### 4.3.1 Rubber Target: Hold-Still

The effect of Micron on cancelling tremor during static conditions was examined through a hold-still task. A participant was asked to locate the tip of the instrument a distance directly above a target defined on the rubber pad, then to maintain the same tip position for a 20 second duration in each trial.

The roots mean square error (RMSE) and the maximum error (ME) were evaluated across trials for each control mode (unaided, lowpass, and scaling). Evaluating the RMSE is useful for the design of the instrument and examining its overall performance. However, the maximum error may be found to be more relevant to surgical applications as even one deviation outside of the desired workspace can cause substantial damage to surrounding tissue structures. Fig. 4.6 presents RMSE (light gray bar) and ME (dark gray bar) averaged across all trials for each individual mode. The error bars in the figures indicate minimum and maximum values over the five trials for each control mode. As shown in Fig. 4.6(top), both RMSE and ME are reduced in aided trials such as lowpass and scaling. The RMSE and ME of lowpass mode are roughly 65% of the unaided trials. The scaling mode shows a statistically significant ( $p = 0.003$ ) reduction of the average maximum error to 34% of unaided maximum error. Scaling mode is shown to be most effective during the hold-still

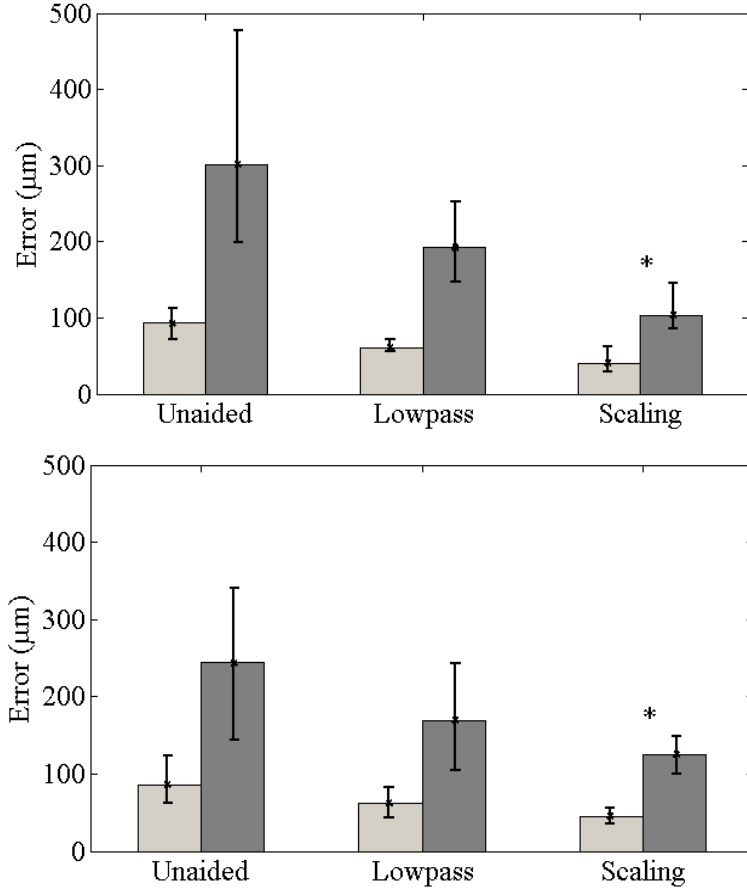


Fig. 4.6. Average RMS (light gray) and maximum (dark gray) errors for hold-still (top) and circle-tracing (bottom) tasks. Error bars indicate maximum and minimum values over 5 trials for each control mode. Scaling mode significantly reduces the errors compared to unaided trials for both hold-still and circle-tracing.

task, despite the primary intention of the control mode to scale down gross motion of the tool tip during dynamic tasks. This may be due to an ability of the scaling modes to cancel erroneous motion driven by eye-hand feedback.

#### 4.3.2 Rubber Target: Circle Tracing

A circle-tracing task was used to examine dynamic tremor cancellation. The participant was instructed to trace a 500  $\mu\text{m}$  diameter circle as accurately as possible on a rubber pad for 20 seconds while maintaining a constant height above the pad. Each activity was repeated for three modes: unaided (no cancellation), lowpass filtering, and motion scaling. The participant performed five trials for each task/mode combination. This resulted in six different task/mode combinations. During the five trials the combinations were varied

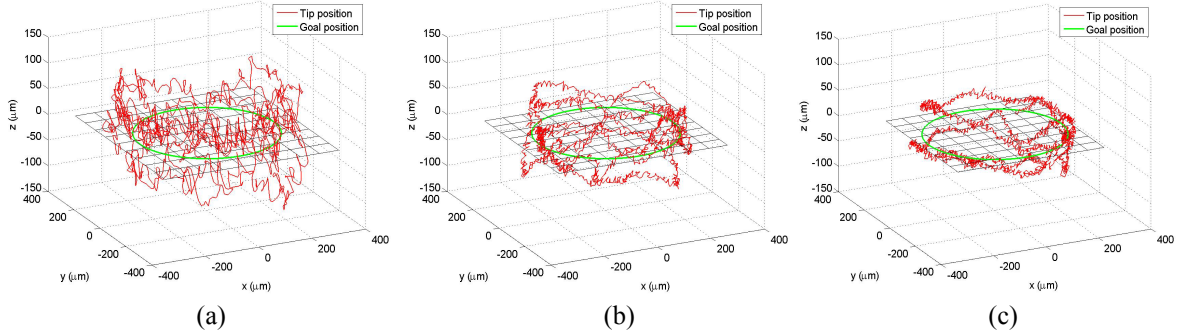


Fig. 4.7. Result of circle-tracing task according to three control modes. Red lines depict the trajectory of the tool tip for 20 seconds. (a) Unaided (off) trial, (b) aided trial with lowpass, (c) aided trial with scaling mode.

using a Latin square design to prevent bias from repeatedly performing the same task.

The circle-tracing task was analyzed by obtaining a best correlation of the data with a 500  $\mu\text{m}$  circle located in a plane parallel to the viewing plane through the microscope. Errors were calculated by comparing the distance between each point and the nearest point on the circle. Error for the circle-tracing task followed a similar trend to the hold-still task as shown in Fig. 4.6(bottom). ME in lowpass mode was reduced to an average of 70% of unaided ME. ME in scaling mode was 51% of unaided ME. The reduction in the scaling mode was statistically significant ( $p = 0.02$ ).

Depth perception is known to be hampered when performing procedures through a surgical microscope [116]. The additional benefit of scaling mode during circle-tracing is illustrated in Fig. 4.7 by the noticeable reduction of error along the viewing depth or z-axis. In unaided cases RMSE in z-axis motion is 123% greater than motion within the transverse x-y plane. In lowpass mode the RMSE in z-axis motion is reduced to 93%, and reduced slightly more to 91% during scaling mode, as compared to RMSE in the transverse plane.

### 4.3.3 Eye Phantom: Hold-Still

Five hold-still trials were also conducted for each of the three control modes within an artificial eye model (referred to as the ‘eye phantom’) for 10 seconds duration. The eye phantom was developed by Johns Hopkins University and consists of a hollow 25 mm diameter sphere molded from soft silicone to mimic the natural sclera. The eye phantom was allowed to freely rotate in a ball cup treated with water based lubricant (K-Y® jelly) as shown in Fig. 4.5. During the task, a 27 Gauge needle was inserted into the eye phantom through a cannula placed in the side wall, imposing an RCM constraint on the needle.

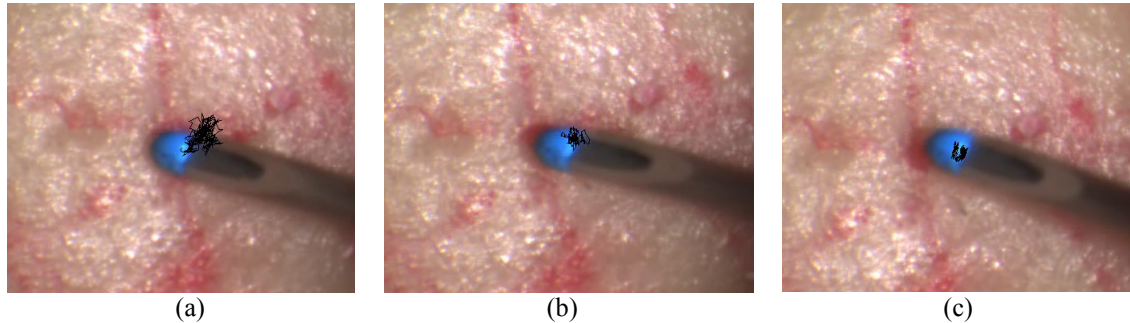


Fig. 4.8. Result of hold still task in an eye phantom. Black lines depict the trajectory of the tool tip for 10 seconds. (a) Unaided (off) trial, (b) aided trial with lowpass, (c) aided trial with scaling mode.

Although the hold still task in the eye phantom is similar to the rubber target version, the difficulty is greater due to the awkward kinematics. This includes the fulcrum imposed by the phantom, as well as the rotation of the eye phantom due to voluntary motion and/or tremor.

Fig. 4.8 shows the tip trajectory (black trace) overlaid on the recorded video clip for 10 seconds for each of the three control modes. Tremor compensation was found to decrease positioning error in the eye phantom similar to rubber target tasks. The scaling mode produced significantly lower error than the unaided mode ( $p = 0.001$ ). The quantitative results are also summarized in Table 4.2.

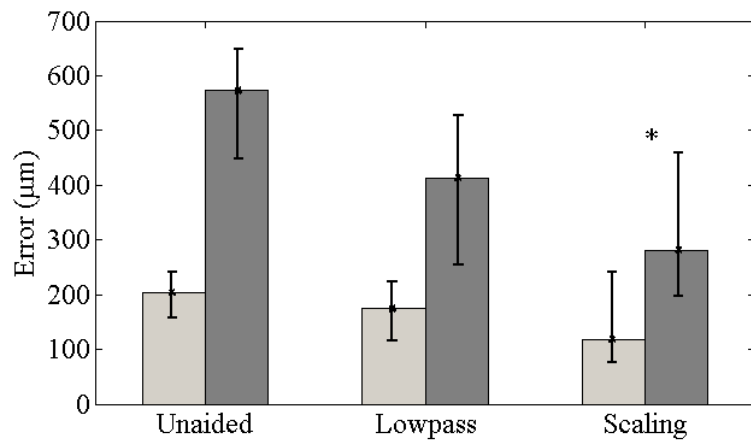


Fig. 4.9. Average RMS (light gray) and maximum (dark gray) errors for hold-still task in an eye phantom. Error bars indicate maximum and minimum values among the maximum errors over 5 trials for each control mode. Statistical significance is marked with an asterisk in the scaling mode.

TABLE 4.2. COMPARISON OF 3D RMS AND MAXIMUM ERRORS

Condition	Control	RMSE ( $\mu\text{m}$ )	ME ( $\mu\text{m}$ )
Rubber target (Hold-still)	Unaided	93 (100.0 %)	301 (100.0 %)
	Lowpass	61 (65.6 %)	192 (63.9 %)
	Scaling	40 (43.6 %)	103 (34.3 %)
Rubber target (Circle-tracing)	Unaided	86 (100.0 %)	244 (100.0 %)
	Lowpass	62 (71.8 %)	170 (69.5 %)
	Scaling	45 (52.6 %)	125 (51.2 %)
Eye phantom (Hold-still)	Unaided	204 (100.0 %)	573 (100.0 %)
	Lowpass	174 (85.3 %)	413 (72.0 %)
	Scaling	117 (57.6 %)	282 (49.2 %)

RMSE = root mean square error, and ME = maximum error.

The values in parentheses indicate percentages of average error with respect to the average error of unaided trials.

## 4.4 Summary

It is found that the 6-DOF Micron provides a statistically significant reduction in 3D positioning error. The new design offers an order-of-magnitude increase in range of motion using the novel linear actuators. As a result, the tremor reduction is improved along the viewing axis, while remaining comparable to the 3-DOF system within the transverse viewing plane [23]. In addition to positioning improvements, an RCM constraint has been implemented to enable proper operation within an eye phantom. In order to achieve higher positioning accuracy and tremor reduction, the control bandwidth of the manipulator should be increased. It is currently limited by a chattering instability in the range of 50-100 Hz. Therefore, future work involves refinement of the micromanipulator design and control. Further experiments will also be performed on various tasks *ex vivo* and *in vivo* with multiple subjects in order to rigorously confirm the handheld performance improvement.



# 5 INTRAOCULAR OPTICAL COHERENCE TOMOGRAPHY

This chapter describes the application of the proposed handheld micromanipulation in handheld OCT imaging. The stabilization of handheld imaging is presented in A-mode and free hand manual scan experiments *in vitro* and *in vivo*. In addition, we also demonstrate the feasibility of automated intraocular acquisition of B-mode and C-mode OCT scans, utilizing a greatly increased range of motion in the new Micron.

## 5.1 Related Work

Optical coherence tomography (OCT) has emerged as an established technology in biomedical imaging since its first demonstration in 1991 [117] because it is capable of noninvasively imaging 3D structures with millimeter penetration, high resolution and speed [118]. Thus, OCT has also become an important tool for ophthalmology in recent years [119]. Its importance was originally due to the confocal scanning laser ophthalmoscope, which images the retina from outside the eye [120], and which was later improved with adaptive optics to correct for natural aberrations in the eye [121]. More recently, intraocular OCT probes for surgical use have appeared [122]. In particular, endoscopic common path OCT offers several advantages such as a simple and compact configuration, a disposable and interchangeable tool usage, and cost-effectiveness. Moreover, it does not involve polarization and dispersion mismatch problems between reference and sample arms [119]. However, it is still challenging to acquire high quality OCT images during freehand operation due to hand tremor, which is defined as involuntary motion with maximum amplitude of about 100  $\mu\text{m}$  at a frequency range from 7 to 17 Hz [123]. Hand tremor distorts tomography results by disturbing the probe location and orientation.

Since hand tremor occurs not only during freehand OCT imaging but also throughout the microsurgical procedure, robotic micromanipulators have been investigated as an aid to facilitate fine movement of surgical tools, compensating tremor [21], [23], [80]. As endoscopic OCT has recently progressed, robotic platforms have been adopted for OCT imaging, offering the aforementioned benefits [124]–[126]. Balicki *et al.* introduced single fiber OCT microsurgical instruments for robot-aided retinal surgery using the Johns

Hopkins Eye Robot [124]. Given a surface profile from OCT data, the system enforces a safety barrier to prevent the surgical tip from touching a retinal surface. It can also maintain a certain distance from the surface and move the tool tip to a designated location after B-mode scanning. A handheld robotic-surgical tool, SMART, has recently been demonstrated to aid in micromanipulation by actively cancelling tremor cancellation using an OCT technique [126]. The OCT probe serves as a 1-D axial distance sensor, being incorporated with a single piezo-motor for active manipulation of the tool. However, it only provides one degrees of freedom (DOF) for both sensing and actuation along the longitudinal axis of the tool, whereas the tip fluctuates in 3-D due to hand tremor. Since the tremor in the transverse plane is not compensated, it may still cause distortion in OCT imaging.

The next challenge in the intraocular OCT imaging is how to accurately reconstruct multidimensional structures from one dimensional A-scans. For example, B-mode and C-mode scans can be generated by tracking the position of a probe as it moves across tissue. Such a scan can be performed manually [124], [127], [128]. However, the accuracy and repeatability of robotic devices provide a clear advantage for acquisition of such scans. Furthermore, with an actuated device, the distance of the probe from the tissue can be automatically controlled, which is beneficial both for safety and for image quality [129]. Spiral-scanning devices have been developed for endoscopic use [130]–[132]. Helical scans have been used for imaging luminal organs such as the esophagus [133]. Robotic B-mode and C-mode scanning has been demonstrated also for intraocular applications, using the Johns Hopkins Eye Robot [124], [125].

## 5.2 System Integration

We adopted Fourier-domain common-path OCT (FD CP-OCT) that uses a common path interference configuration [134]. As the distal end of a single mode fiber is defined as a reference plane, a surface profile and a substructure can be extracted. The OCT system is primarily composed of a fiber-optic probe, a superluminescent diode (SLED), an optical coupler, and a custom-built spectrometer as illustrated in Fig. 5.1. The light source has a center wavelength of 840 nm with a spectral width of 50 nm. The spectral interference detected by the spectrometer is transferred to a workstation for signal processing. As a result, a single axial scan (A-scan) is acquired at a system sampling rate of 5 kHz with 10 bit digitized data, providing a theoretical axial resolution of 6.2  $\mu\text{m}$  and practical imaging range of 2 mm in water.

The intraocular OCT probe consists of a standard single-mode fiber, with 9- $\mu\text{m}$  core, 125- $\mu\text{m}$  cladding, and an outer coating 245  $\mu\text{m}$  in diameter, bonded within a 25-Ga. hypodermic needle. For easy attachment of the OCT probe onto Micron, the probe is composed of multiple sheaths with hypodermic tubing of different diameters as shown in Fig. 5.2. The probe is fitted into the through hole of a Luer-Slip adaptor on Micron and

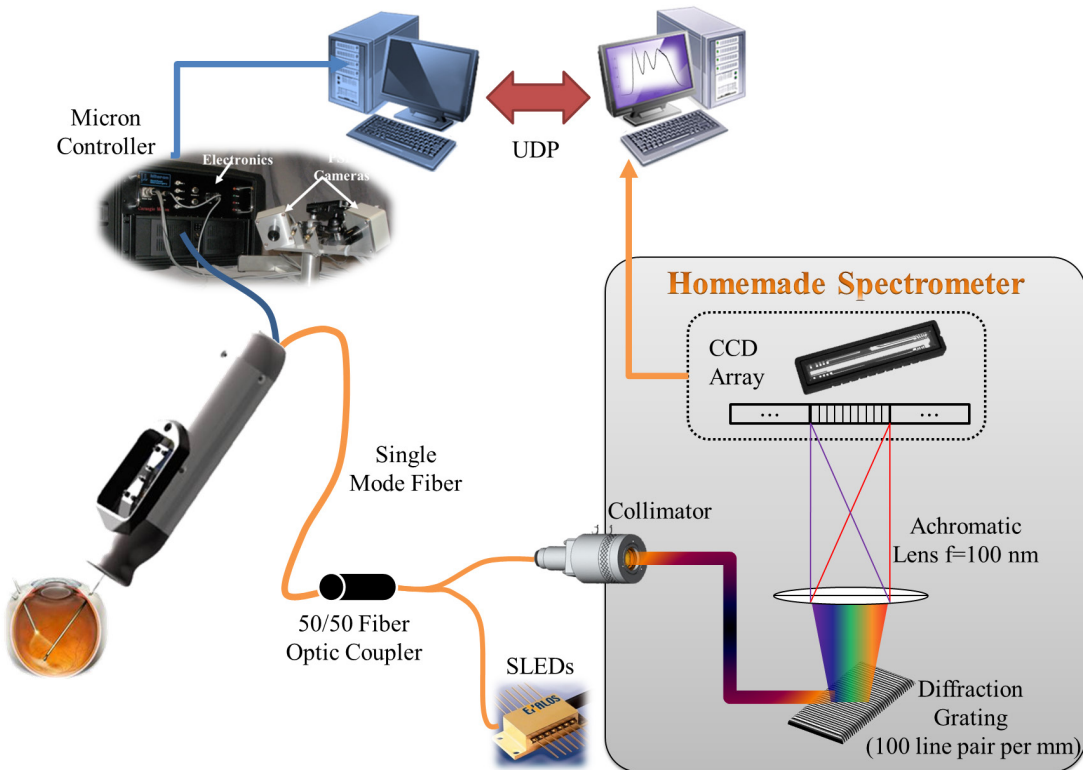


Fig. 5.1. Schematic diagram of a handheld OCT imaging system using Micron.

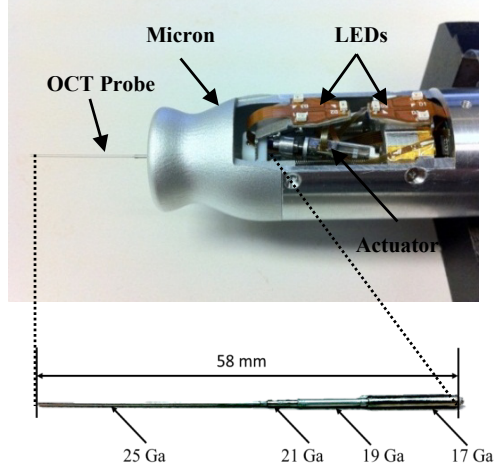


Fig. 5.2. Micron, an active handheld micromanipulator with an OCT probe (a) and the OCT probe with multiple sheaths of hypodermic tubing.

coaxially aligned with the center of the manipulator. The probe length is designed to protrude 25 mm from the front cover of Micron to freely reach within the rabbit eye (about 15 mm in diameter). Once the OCT probe passes through a guide tube inside Micron and reaches the frontal part of Micron, it is affixed to the Luer adapter by a set screw.

All Micron data and status are sent to the workstation via an Ethernet using User Datagram Protocol (UDP) to minimize latency. B-mode and C-mode scans were composed of position-tracked A-mode scans using the 6DOF pose information from the same optical tracker used for feedback control of Micron, running at a 1 kHz update rate. The OCT image data acquired from the probe is sent to a visualization workstation via an Ethernet. Both applications are developed using the *cisst-saw* open source C++ framework (<http://www.cisst.org/cisst/saw/>).

## 5.3 Stabilization of Handheld Imaging

To stabilize handheld imaging, Micron utilizes the same control filters used for active tremor cancellation. Consequently, the manipulator operates in two control modes: lowpass to suppress hand tremor, and scaling to provide both tremor cancellation and scaling.

### 5.3.1 Open-Sky: A-Mode Scan

“A-scan” tests were first conducted during hold-still tasks for three cases: unaided (no cancellation), lowpass, and scaling. A surgeon was asked to maintain the tool tip at certain height from a fundus image printed on a paper for 12 s as shown in Fig. 5.3(a). Each A-scan was accumulated as a single column in an OCT image over the 12 s duration as shown in Fig. 5.4. Fig. 5.4(a) represents A-scan images and short-time Fourier transform (STFT) of surface profiles depending on three types of control modes. The y axis depicts how the displacement between the distal end of OCT probe and the flat paper surface varies during hold-still trials of 12 s. This height variation is a combination of hand tremor and also voluntary motion to correct tip error from eye-hand feedback of the surgeon.

We found that the profiles were smoother in aided cases such as lowpass and scaling modes than in unaided cases as shown in Fig. 5.4(a). This is because the tremor was canceled during aided trials such that the profile fluctuation was decreased. The standard deviations of the profiles were reduced by approximately 56 % in both aided trials compared with unaided cases. Significant differences between lowpass and scaling modes were not evident in the quantitative results summarized in Table 5.1. Nevertheless, the

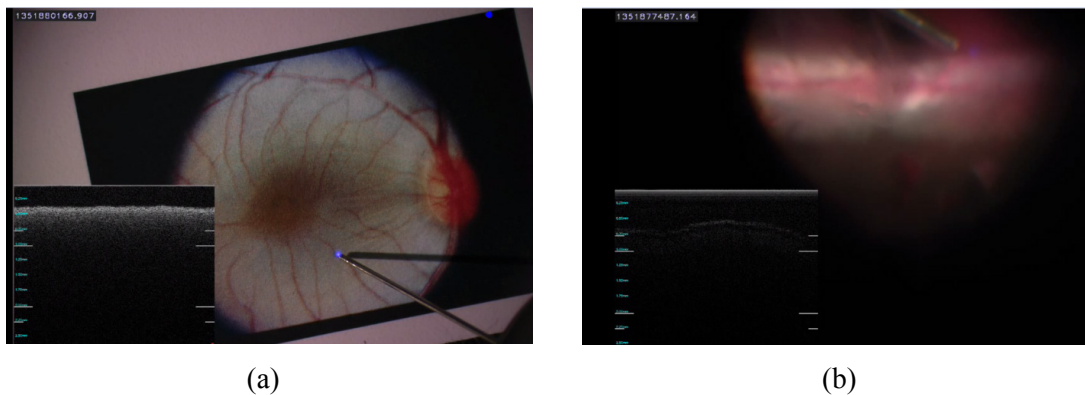


Fig. 5.3. (a) A-scans during hold-still task above a fundus image. (b) OCT scans (A-scan and M-scan) in a live rabbit eye.

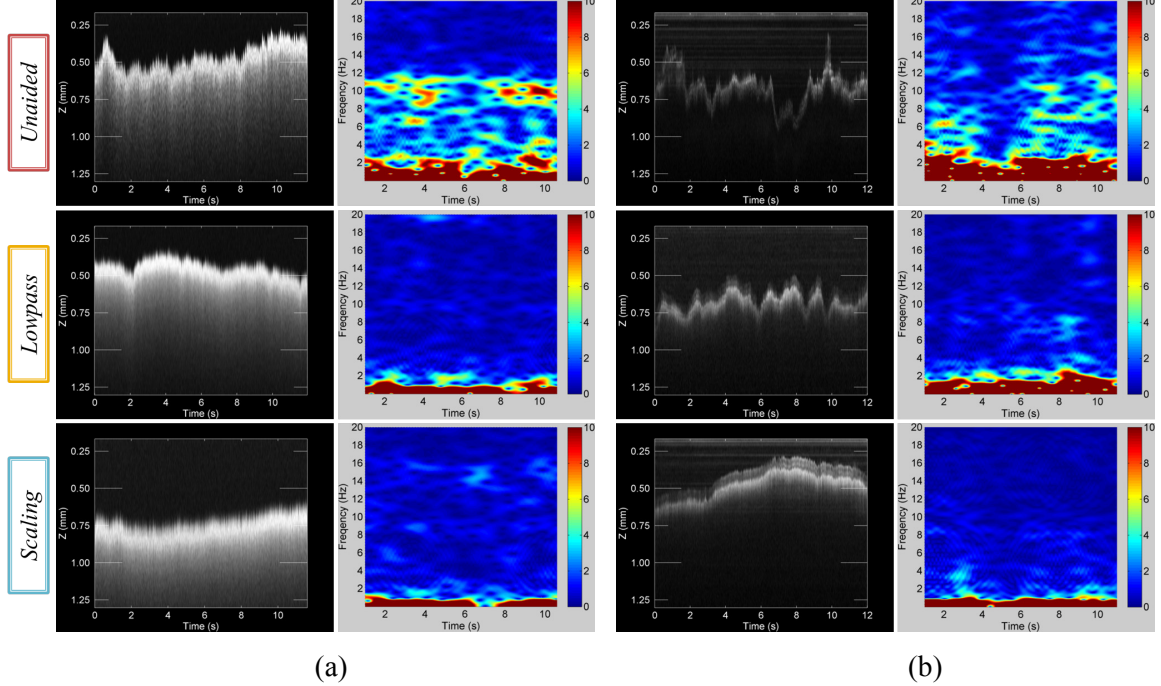


Fig. 5.4. Results of OCT scan images and short-time Fourier transform (STFT) of surface profiles for the control modes, arranged in descending order: *unaided*, *lowpass*, and *scaling*. (a) A-scans during hold-still task for 12 s in air. (b) A-scans during hold-still task in the live rabbit eye for 12 s.

profile acquired by scaling mode qualitatively appears much smoother than lowpass mode. In fact, scaling mode provides the surgeon finer control in voluntary motion and also scales excessive input by eye-hand feedback. In the spectrum analysis over the time, we definitely see noticeable difference between unaided and aided trials, specifically at the typical tremor band from 7 Hz to 15 Hz shown in STFT results of Fig. 5.4(a).

### 5.3.2 In-vivo: A-Mode Scan

In tests *in vivo*, under a board-approved protocol, a rabbit was anesthetized and the vitreous humor was removed from the eye by pars plana vitrectomy. In hold-still tasks, the surgeon followed the same protocols done in the previous freehand trials.

Similar results were discovered during *in-vivo* trials, shown in Fig. 5.4(b). Since the retina has a multilayer structure, for accurate evaluation of the performance, distance was measured from the brightest layer in the OCT images. The lowpass trial shows the most similarity to the open-sky trial in terms of reduction in both standard deviation and peak-to-peak deviation. In scaling mode, the reduction in the standard deviation is not as great as in the open-sky trial although the average spectral power density within the tremor frequency band is 4dB lower than in lowpass mode. The large standard deviation seems to

TABLE 5.1. ERRORS DURING HOLD-STILL TASKS

Condition	Control	Std. ( $\mu\text{m}$ )	Pk-Pk ( $\mu\text{m}$ )	Power ( $\mu\text{m}^2/\text{Hz}$ )
Open-Sky (A-Scan)	Unaided	80 (100.0 %)	357 (100.0 %)	6.631 (0.0 dB)
	Lowpass	45 (55.9 %)	258 (76.9 %)	0.366 (-12.6 dB)
	Scaling	46 (56.9 %)	229 (70.0 %)	0.668 (-10.0 dB)
In-Vivo (A-Scan)	Unaided	101 (100.0 %)	577 (100.0 %)	3.681 (0.0 dB)
	Lowpass	55 (55.0 %)	337 (74.9 %)	0.698 (-13.1 dB)
	Scaling	85 (84.4 %)	326 (68.7 %)	0.278 (-11.4 dB)

Std. = Standard deviation and Pk-Pk. =Peak-to-peak deviation.

be due to the gross motion of the tip by voluntary motion rather than instability from tremor. We also found that overall errors in trials *in vivo* were greater than the errors in the open-sky tasks. This seems to be a result of the awkward constraint at the sclera and the movement of the eye, which degrades the surgeon's manipulability. The data acquired through A-scan are summarized in Table 5.1 for hold-still tasks.

### 5.3.3 In-vivo: M-mode Scan

A manual scan (M-mode) under the scleral constraint is generally more challenging than hold-still tasks, since the movement of the tip creates reaction force from the sclera, and frequently moves the eye itself, rotating it in its socket. In "M-scan" tests, the surgeon was required to scan a line across an area of interest in the eye while different control modes were enabled. Fig. 5.3(b) shows the retinal image and OCT profile during M-scan on the retinal surface of the rabbit eye.

M-scan results demonstrate that there is a qualitative difference among the scanned profiles in Fig. 5.5 and Fig. 5.6(c). It is not possible to apply the same error metrics used in the hold-still task on the arbitrary profiles because each scan followed a different trajectory. However, we see there is an overall reduction in the tremor-caused variation of the profiles in Fig. 5.6(c). The reduction of the average power is given by 13.1 and 11.4 dB in the frequency band of interest (7 to 20 Hz) as compared with the unaided case.

The data presented indicate that the quality of OCT imaging is improved by a handheld micromanipulator capable of cancelling hand tremor. We found noticeable attenuation on the variation of OCT profiles in both A-scans and M-scans, reflecting reduction of the hand tremor artifact. Compared to 1 DOF micromanipulators, Micron offers the advantage of suppressing both axial and transverse components of hand tremor and it does not rely on the OCT data for feedback.

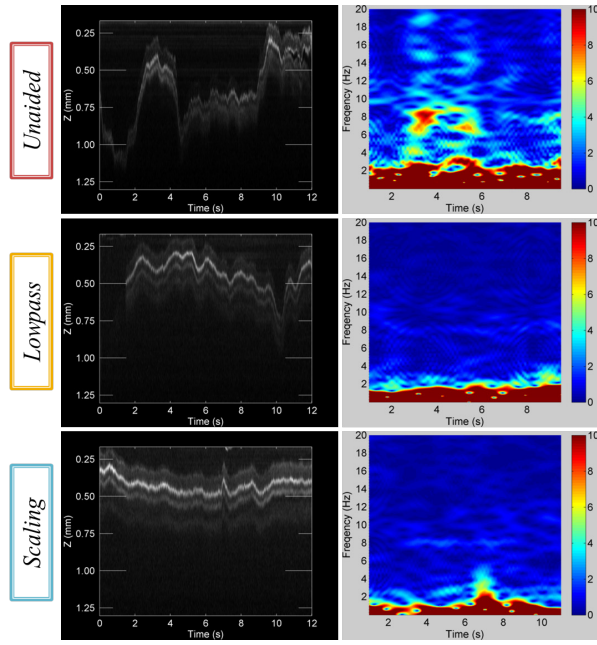


Fig. 5.5. Results of OCT M-scan images in the live rabbit eye and STFT of surface profiles.

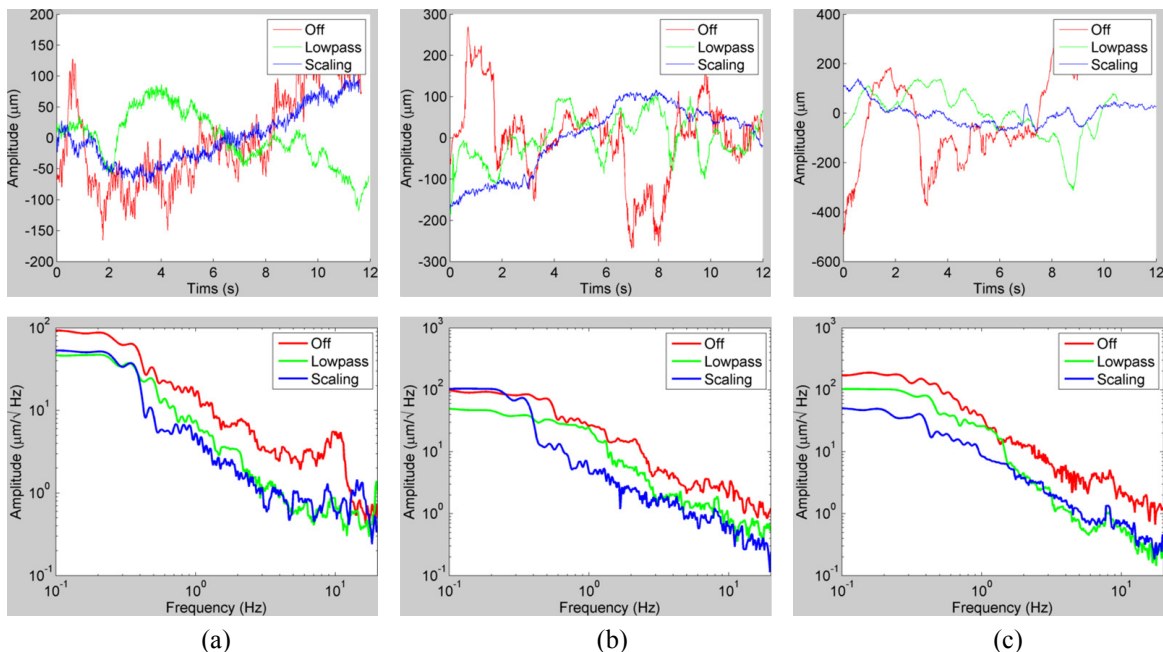


Fig. 5.6. Results of OCT scanned profiles (top) and power spectrogram (bottom). (a) A-scans during hold-still task in the air. (b) A-scans during hold-still task in the live rabbit eye. (c) M-scans, manually scanning a line of interest in the live rabbit eye. In the A-scans, the profiles are the axial deviation of the tip.

## 5.4 Multidimensional Scanning

Two handheld tests of scanning performance were conducted. During a scan, the control system of Micron acts to suppress tremor and any other hand motion, the intention being to allow no motion of the tip other than the specified scan.

### 5.4.1 C-Mode Scan

The first test of the system was a spiral C-mode scan of group 1, element 4, from a USAF 1951 MIL-STD-150A resolution test chart (Fig. 5.7(a); group 1, element 4 is slightly right of center). The probe tip speed along the spiral trajectory was set at 2 mm/s. The commanded spacing between adjacent cycles of the spiral was 50  $\mu\text{m}$ . The total diameter of the scanned spiral was 1 mm. Because the OCT system sampling rate is higher than the sampling rate of ASAP, linear interpolation between measured poses of the probe was used to estimate the pose corresponding to each OCT A-mode scan or “data point.”

The result of the spiral C-mode scan is shown in Fig. 5.7(b). A false-color representation and thresholding were used to aid visualization. The spiral contains 17862 individual A-mode scans. This included 7917 poses measured by ASAP; hence, the scan

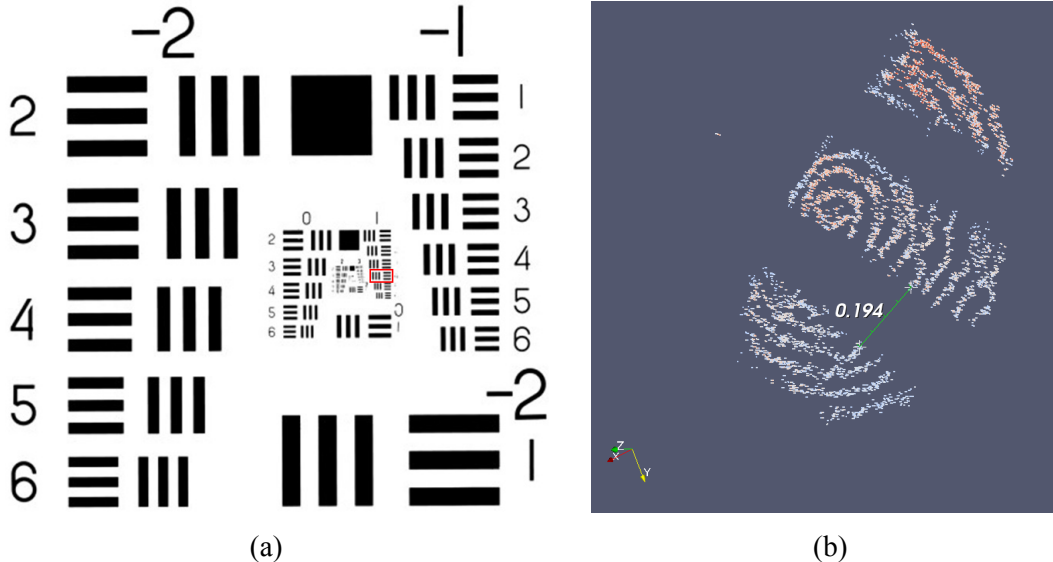


Fig. 5.7. (a) USAF 1951 MIL-STD-150A resolution test chart. (b) Result of spiral C-mode scan of USAF 1951 MIL-STD-150A resolution test chart, group 1, element 4. The three bars from the element in the chart (which are black in the original chart) are visible in the scan. The space between bars, which measures 0.176 mm on the chart, is measured at 0.194 mm in the acquired scan.

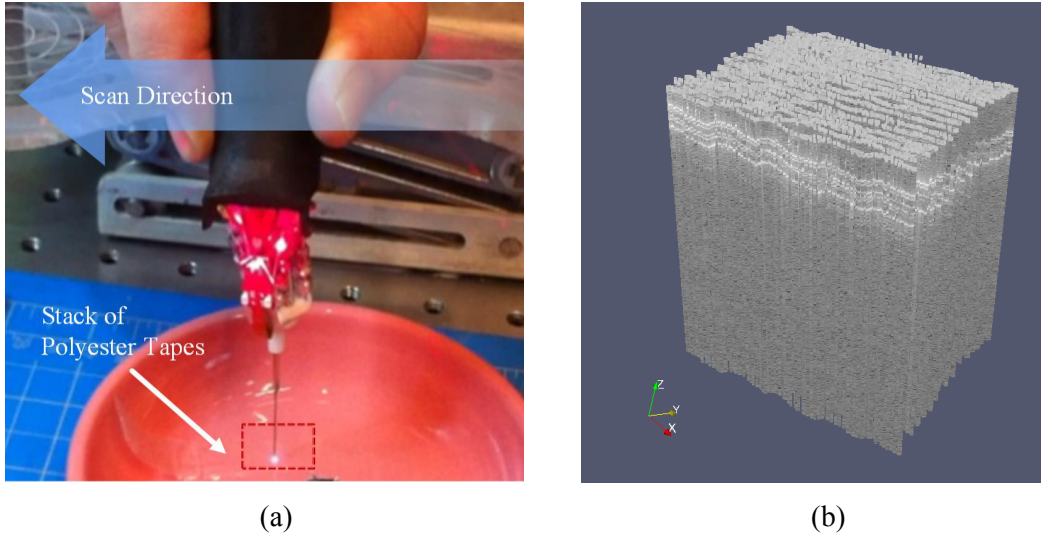


Fig. 5.8. Result of zigzag B-mode scan of a stack of 3 layers of 3M™ Polyester Tape 8911 (each layer is 50  $\mu\text{m}$  thick). B-mode scanning was performed automatically, while movement in the perpendicular direction to generate the zigzag was performed manually. The 3 layers are evident near the top of the scanned volume.

time was 7.9 s. The space between bars in the scanned image was estimated using a drawing widget in the visualization software. The space between bars, which measures 0.176 mm on the chart, is measured at 0.194 mm in the acquired scan.

#### 5.4.2 B-Mode Scan

The second demonstration was a repeated B-mode scan. The manipulator oscillated the probe in a triangular wave pattern at 5 Hz. The motion of the tip of the probe was 3 mm peak-to-peak at a speed of 30 mm/s. During execution, the tool was moved manually in the direction perpendicular to the B-mode scan, resulting in a zigzag scan pattern with a total of 50 scan lines. The scanned material in this case was a stack of 3 layers of 3M™ Polyester Tape 8911 as shown in Fig. 5.8(a). Each layer is 50  $\mu\text{m}$  thick (30  $\mu\text{m}$  adhesive and 20  $\mu\text{m}$  backing).

The result of the zigzag B-mode scan is shown in Fig. 5.8(b). The three layers of the tape can be clearly seen near the top of the scanned volume. The total pattern contains 11272 individual A-mode scans. This included 5045 poses measured by ASAP; the scan time was 5.0 s.

## 5.5 Summary

We have demonstrated the first handheld OCT imaging using Micron *in vivo*. Further experiments are required in order to obtain statistically significant results. Improvements in Micron performance and in surgeons' familiarity with each control mode are expected to yield better performance in handheld OCT imaging. We will also be able to utilize a visual cue injection system [135] to guide the operator along predefined paths for M-scans, which would facilitate quantification of M-scan performance.

The data presented indicate the general feasibility of acquiring surgically useful OCT scans in B-mode and C-mode using 6 DOF Micron. Since those results were given by the initial prototype of the 6-DOF Micron, we expect the latest 6-DOF Micron would provide enhanced OCT images in terms of speed and accuracy.



## **6 ROBOT-AIDED INTRAOCULAR LASER SURGERY I: POSITION-BASED VISUAL SERVOING**

Laser photocoagulation is a mainstay or adjuvant treatment for a variety of common retinal diseases. However, automated laser photocoagulation during intraocular surgery has not yet been established. This study presents a system for automated intraocular laser surgery using the new 6-DOF Micron. The new handheld instrument features an enlarged range of motion to enable automated scanning, and its added degrees of freedom accommodate use through a sclerotomy. The goals of the handheld robot-aided system are thus to enhance accuracy and efficiency, improve safety, and reduce cognitive load on the surgeon.

In this chapter, we describe the development of the system, focusing primarily on the feasibility of automated intraocular laser photocoagulation. To automatically treat lesions, we adopt position-based visual servoing for control, and compare its performance with manual execution in an “open-sky” environment. Finally, the technique is demonstrated in an eye phantom, including tracking the movement of the retina.

## 6.1 Related Work

Retinal laser photocoagulation is a common treatment for retinal diseases such as diabetic retinopathy, retinal detachment, and macular degeneration [34], [38], [136]. The laser treatment applies patterns of multiple burns in order to impede the growth of new abnormal blood vessels in retinopathy [34], or to seal leaking blood vessels in macular edema [38].

For optimal clinical outcomes, those procedures require high accuracy in terms of the location and size of laser spots, with delivery of the proper amount of energy [137]. However, surgeons often encounter complications due to the limited maneuverability of surgical instruments, hand tremor, and poor visualization of surgical targets during operation. This may lead to irregular laser burns on the retinal surface and/or inadvertent coagulation of healthy retina or other ocular structures, which can result in an unintended reduction in macular function, visual field defects, or choroidal neovascularization [138]. Application of laser to unintended regions such as the optic nerve and the fovea has potential to cause permanent central vision loss [42]. In addition, long treatment sessions may impose discomfort and tedium on both patients and ophthalmologists [43], [44].

Hence, automated approaches have been introduced into laser photocoagulation in order to improve treatment accuracy, increase patient safety, and reduce operating time [43], [44], [139]. Initially, the feasibility of an automated laser delivery system was demonstrated to place multiple lesions of predetermined sizes into known locations in the retina [139]. For automation, a tracking feature is essential to achieve high accuracy while compensating for the considerable movement of the eye, since the eye cannot be completely immobilized. Later research efforts led to the development of hybrid retinal tracking for automated laser photocoagulation, incorporating global tracking with digital imaging and high-speed analog local tracking [140], [141]. Finally, computer-guided retinal laser surgery system has been realized, utilizing digital fundus imaging in real time, and also controlling lesion depth [44], [142]. Blumenkranz *et al.* also introduced a semiautomated system in which the ophthalmologist has control over the treatment at all times [43]. The semiautomated system still retains the primary advantages of the automated system, while rapidly delivering up to 50 pulses with shorter pulse duration on predefined spots, using a galvanometric scanner. The semiautomated system is kept relatively simple and inexpensive by eliminating certain features that are necessary in the automated system, such as retinal tracking and automated lesion reflectance feedback. Such systems, now commercially available as Navilas® and PASCAL, have been increasingly adopted in the

clinic [137], [142]–[144]. However, these systems treat through the pupil, and are designed for use in the outpatient clinic rather than the operating room. Hence, it is still challenging to apply it to intraocular surgery for purposes such as intraoperative retinal breaks.

In order to bring such benefits of automated laser photocoagulation to intraocular surgery performed during pars planar vitrectomy [145], we presented semiautomated laser photocoagulation using an active handheld instrument known as “Micron” [26]. The semiautomated system corrected error between the preoperative target and the current beam location by deflecting the laser probe attached to Micron. However, the system was only able to correct error within a few hundred microns of the target due to its limited range of motion. The operator was thus required to deliberately move the laser probe in a raster-scan fashion in order to apply the full pattern of burns; i.e., the operator provided gross motion, while Micron provided fine motion. The distance of the tool from the retinal surface had to be manually regulated, relying on the operator’s depth perception, once again due to the limited range of motion of the active instrument. Furthermore, the limited degrees of freedom (DOF) hindered the use of the instrument through a fulcrum such as a sclerotomy in an intact eye. Accordingly, tests were performed only in “open sky” fashion on fixed surfaces, without tracking of anatomy [26].

Therefore, we introduce robot-aided intraocular laser surgery, using an improved prototype of Micron in order to overcome these drawbacks [146]. The new handheld instrument incorporates 6-DOF manipulation and provides much greater range of motion, which automates scanning of the laser probe over the entire pattern area, and accommodates use through a sclerotomy [147].

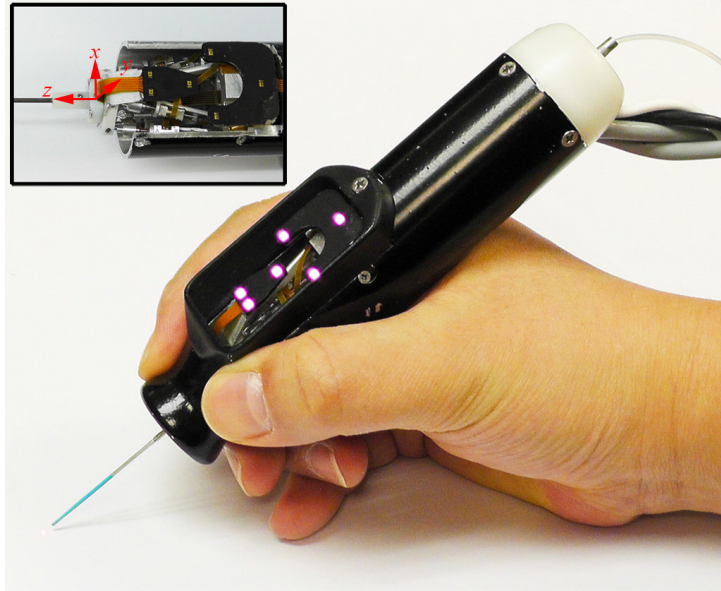


Fig. 6.1. 6-DOF handheld micromanipulator integrated with a laser probe.

## 6.2 System Overview

The robot-aided intraocular laser photocoagulation system features the 6-DOF handheld instrument, Micron, as shown in Fig. 6.1, in which the laser probe is automatically manipulated to treat preoperatively specified targets via a vision processing system. The new Micron prototype incorporates a miniature Gough-Stewart platform actuated by six piezoelectric linear motors (SQUIGGLE® SQL-RV-1.8, New Scale Technologies, Inc., USA) [147]. The manipulator provides 6-DOF motion of the end-effector within a cylindrical workspace 4 mm long and 4 mm in diameter, while allowing for a remote center of motion (RCM) at the point of entry through the sclera, enabling it to execute automated scanning for intraoperative optical coherence tomography (OCT) [115] or patterned laser photocoagulation [146].

For control, 6-DOF Micron senses the position and orientation of both the tool tip and the handle, using a custom-built optical tracking system (Apparatus to Sense Accuracy of Position, or “ASAP”) [111]. The handheld instrument is equipped with two sets of infrared LEDs for the optical tracking system: one set on the tool mount and the other on the handle (visible in Fig. 1a). The position and orientation are retrieved by detecting the pose of each LED panel at a sampling frequency of 1 kHz over a 27-cm<sup>3</sup> workspace; ASAP performs this tracking with less than 10 μm RMS noise. The specification and performance of the

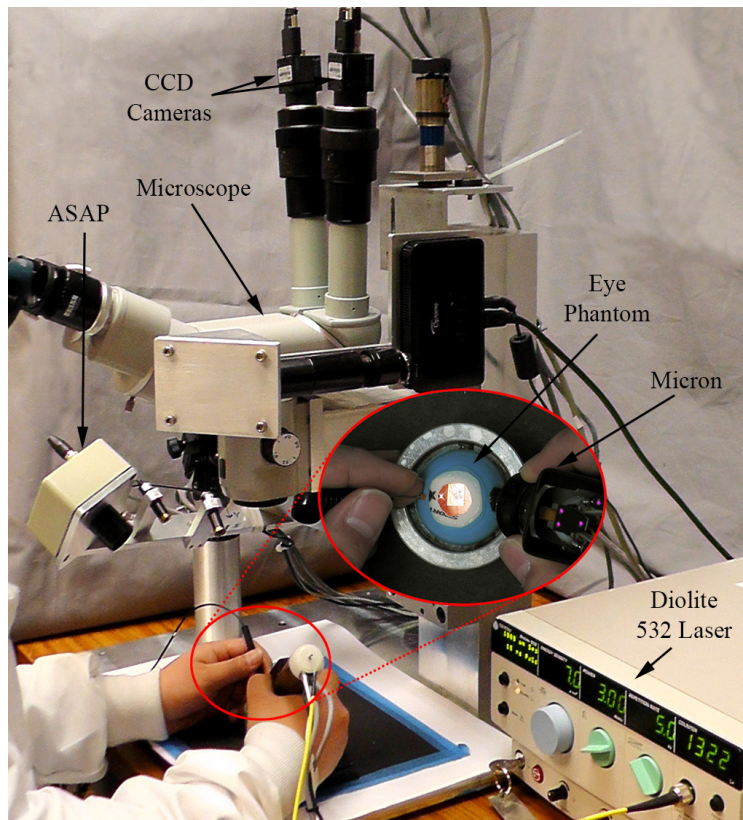


Fig. 6.2. System setup for automated intraocular laser surgery

manipulator are described in Chapter 3 and 4, in detail. Hence, the laser probe attached to the micromanipulator can be controlled accurately according to a specified 3D goal position for the laser tip, regarding undesired handle motion as a disturbance. The remaining degrees of freedom in actuation are independently controlled at the RCM by the operator.

The vision system consists of a stereo operating microscope (Zeiss OPMI<sup>®</sup>1, Carl Zeiss AG, Germany) with variable magnification (4–25 X), two CCD cameras (Flea<sup>®</sup>2, Point Grey Research, Richmond, BC, Canada), and a desktop PC. The vision system calculates the goal position of the laser tip to minimize error between the target and the detected aiming beam, and delivers the goal position to the Micron controller. The system also detects tip positions in 2D images for an initial calibration between the vision system and the Micron controller. A pair of images streams to the PC at 30 Hz with  $800 \times 600$  resolution for further processing, which is synchronized with the Micron controller via an external trigger provided by one of the cameras.

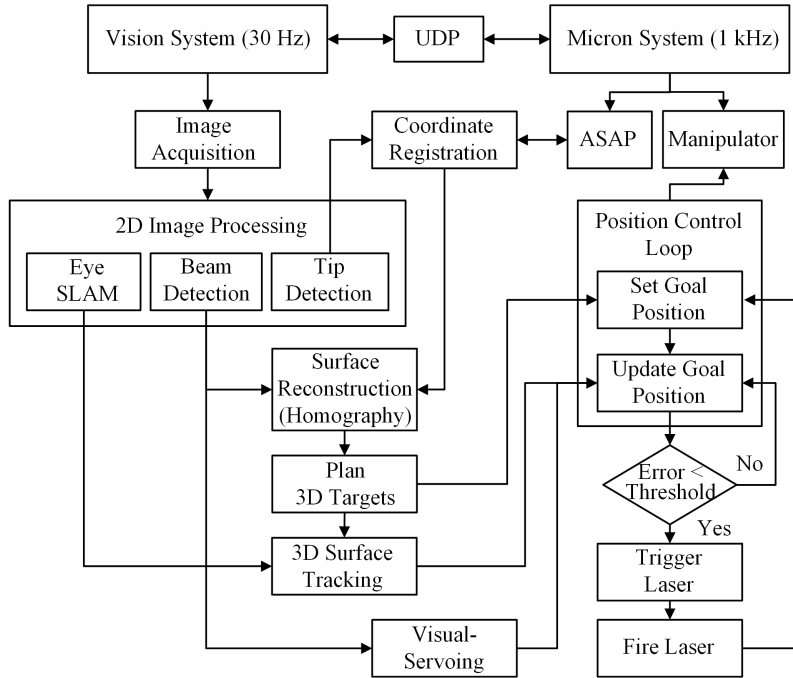


Fig. 6.3. Block diagram of the system, showing data and execution flow.

Once a target location for the treatment is defined on a retinal surface with respect to the ASAP coordinates, the corresponding 3D goal position of the laser tip is sent to the Micron controller. During the control, 3D error between the target and the aiming beam positions is minimized by displacement of the laser tip via position-based visual servoing. As the aiming beam reaches the target within a specified tolerance or threshold, the laser is triggered. Once the vision system detects the laser firing, the next target is assigned and the procedure is repeated until completion of photocoagulation of all targets. Fig. 6.2 shows the overall setup with the Micron, vision, and laser systems. The overall control flow is depicted in Fig. 6.3.

For the automated treatment, targets are first placed on the reconstructed retinal surface and then updated with respect to the movement of the eye by tracking blood vessels on the surface. The tracking feature is essential in order for the automated laser photocoagulation to compensate for movement of the eye in its socket during operation [140], [141]. For example, vitreoretinal surgeons often manipulate the eye with a surgical tool to explore region of interest due to the limited field of view of operating microscopes; the patient (often sedated but not under general anesthesia) may also move their head and rarely the eye. Accordingly, voluntary/involuntary motion is inevitably introduced to the eyeball during operation, which would lead to failure of preoperative registration. To tackle this

issue, we have developed an algorithm, called “eyeSLAM,” to both map and localize retinal vessels by temporally fusing and registering detected vessels in a sequence of frames [27].

For laser photocoagulation, an Iridex 23-gauge EndoProbe is attached to the tool adaptor of Micron, and an Iridex Iriderm Diolite 532nm Laser (Iridex, Mountain View, CA) is interfaced with the Micron controller.

### 6.2.1 System Calibration

To utilize vision information in control, we first register a pair of cameras in the stereo microscope to the Micron control system. Once the 2D camera coordinates are registered to the Micron control coordinates in 3D (called herein the “ASAP coordinates”), we can then define a target surface in the ASAP coordinates by matching multiple correspondences detected in the cameras. Since a common method relying on multiple views of a planar object would not be feasible in a microsurgical environment, we directly match a set of 3D tip positions measured by ASAP with a set of 2D positions detected by the camera. These procedures are accomplished by a single step to sweep the laser probe above the retinal surface while detecting the 2D positions of the tip and aiming beam in images.

For the registration, a set of 2D tip positions  $\mathbf{p}_c^i \in \mathbb{R}^2, \forall c \in \{L, R\}$  and  $\forall i \in [1, N]$ , in the left and right images, are matched with the corresponding 3D ASAP tip positions  $\mathbf{P}_{ASAP}^i \in \mathbb{R}^3$ , where  $N$  is the number of samples. We thus obtain camera calibration (or projection) matrices  $\mathbf{M}_c \in \mathbb{R}^{3 \times 4}, \forall c \in \{L, R\}$  to map a point in 3D to projected points in 2D in both left and right images as in (6.1) using a direct linear transformation (DLT) method [148].

$$\mathbf{p}_{tip} \equiv \mathbf{M}_c \mathbf{P}_{tip}^{ASAP}, \quad \forall c \in \{L, R\}, \quad (6.1)$$

The coordinate registration is dependent primarily on the accuracy of the tip position in 3D. However, the principle of the ASAP measurement may lead to an erroneous tip position, since we estimate the tip position from the pose of the LEDs mounted on the moving platform rather than directly measuring the tip. The resulting tip position is computed via rigid body transformation of the platform, taking into account a tool offset  $\mathbf{T}_{offset}$  at the tip, typically given by the length of the tool used, as in (6.2).

$$\mathbf{P}_{tip}^{ASAP} \equiv \mathbf{P}_{wt} \cdot \mathbf{T}_{offset}, \quad (6.2)$$

where  $\mathbf{P}_{wt}$  describes the position and orientation of the moving platform and acts as a

homogeneous transformation. Accordingly, any lateral deviations at the tip, such as  $x$ - and  $y$ -offsets due to misalignment or bending of the tool, affect the estimation of the tool tip pose, resulting in error in the coordinate calibration. As a long slender tool ( $\sim 60$  mm long with less than 1 mm diameter) is used in intraocular surgery, any small angular displacements of the tool could cause large lateral offsets at the tip.

Hence, we propose a new approach to find the tip offsets  $\mathbf{T}_{\text{offset}}$  and the projection matrices of the cameras simultaneously using an optimization technique. This idea is inspired by the observation of the projection error of the tool tip in images, given inaccurate tool offsets. The error between the projected and detected tip positions becomes significant under gross change of the orientation of the manipulator while scanning the tool over the surface. Therefore, we model the tip offsets in terms of angular variations  $\theta_x$  and  $\theta_y$ , and the length of the tool  $l_0$  in (6.3), and we collect data points while varying the orientation of Micron.

$$\mathbf{T}_{\text{offset}} \equiv \mathbf{R}_x(\theta_x) \cdot \mathbf{R}_y(\theta_y) \cdot \mathbf{T}_0, \quad \mathbf{T}_0 = [0 \ 0 \ l_0 \ 1]^T \quad (6.3)$$

The optimization minimizes the squared sum of the projection errors in the left and right camera as in (6.4).

$$\min \left( \sum_{i=1}^n \left[ (\mathbf{p}_{\text{ProjL}}^i - \mathbf{p}_{\text{DetL}}^i)^2 + (\mathbf{p}_{\text{ProjR}}^i - \mathbf{p}_{\text{DetR}}^i)^2 \right] \right), \quad (6.4)$$

where the  $i$ th projection of the tool tip using (6.1) is denoted by  $\mathbf{p}_{\text{ProjL}}^i$  and  $\mathbf{p}_{\text{ProjR}}^i$  for the left and right cameras, respectively. The tip positions detected in the corresponding images are

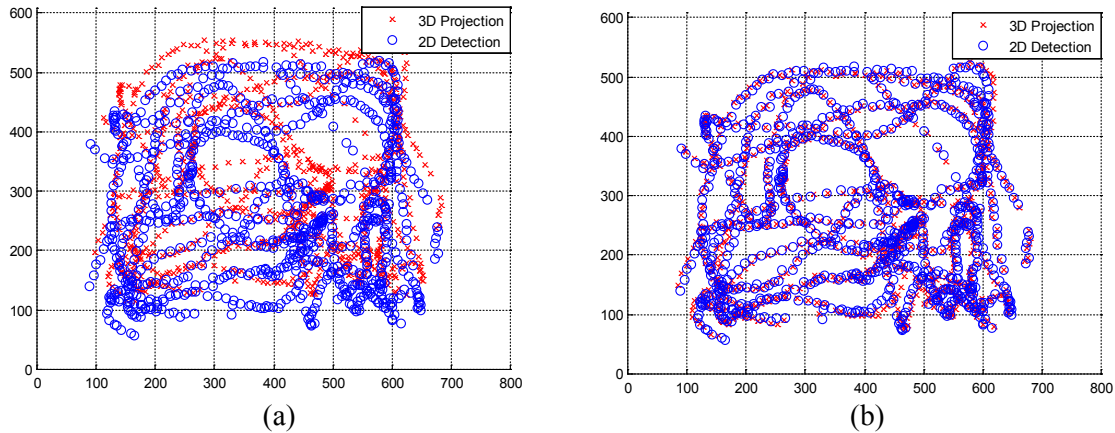


Fig. 6.4. Tip position collected during the calibration procedure. The red cross indicates the projection of the 3D ASAP tip position and the blue circle for the detected tip position in the left image. (a) Before tip-offset calibration. (b) After tip-offset calibration.

indicated as  $\mathbf{p}_{\text{DetL}}^i$  and  $\mathbf{p}_{\text{DetR}}^i$ . We utilize the Matlab<sup>TM</sup> function ‘fminsearch.m’ for unconstrained nonlinear optimization, given the initial length of the tool. Fig. 6.4 shows the projection of the tool tip (red) and the detected tip (blue) on the left image. The projection results for a fixed tool offset along the  $z$ -axis and the optimal tool offsets including  $x$ - and  $y$ -offsets are presented in Fig. 6.4 (a) and (b), respectively. The average projection error decreases from 48.1 to 8.0 pixels by the optimization, compared to the fixed  $z$ -axis offset with a length of 55.0 mm. The resulting tip offsets are given as -694, 115, and 54,153  $\mu\text{m}$  for  $x$ -,  $y$ -, and  $z$ -offsets in the Euclidean space; the corresponding angular variations are  $0.12^\circ$  and  $0.73^\circ$  along  $x$  and  $y$  axes, respectively.

### 6.2.2 Retinal Surface Reconstruction

Reconstructing the retinal surface in 3D is necessary for planning burn patterns and regulating the distance of the laser tip from the surface in the automated operation. We adopt a structured light approach to reconstruct the 3D surface instead of the common method of relying on dense stereo matching of feature points in the left and right images. This is because the traditional key point detectors such as SIFT (scale-invariant feature transform) or SURF (speeded up robust features) are prone to fail on such the textureless retina [27]. To provide the structured light, we only need to sweep the Micron back and forth above the surface without a complex coding on the light due to the simplicity of the retinal surface (i.e., no discontinuities, no large spectral reflections, no opacity, and no occlusions). A red aiming beam emitted from the laser probe allows a substantial correspondence on the left and right images.

Given the camera calibration in (6.1), we also obtain a point cloud in 3D by triangulating multiple pairs of aiming beams detected on the left and right images, which belongs to the retinal surface  $S$ .

$$S : \mathbf{P}_{\text{beam3D}}^i = \Phi(\mathbf{p}_{\text{beamLeft}}^i, \mathbf{p}_{\text{beamRight}}^i, \mathbf{M}_L, \mathbf{M}_R) \in S, \quad \forall i \in [1, N], \quad (6.5)$$

The resulting surface is then modeled as a plane in the ASAP space, rather than a curved surface such as a quadratic or spherical shape, which brings the simplicity in control as well as benefits the surface tracking. Furthermore, the least-squares type of spherical fitting would not work for such as a small area patch, compared to the entire area of the sphere, when containing noisy data points because of the nature of 3D reconstruction. For example, an area patch with 4-mm diameter covers only 2.5% of an entire sphere of the size of the typical human eyeball (25 mm in diameter), which is subject to failure to fit such noisy

data. Since only a relatively small area is observed through the microscope, the planar assumption does hold approximately in the area of interest, yielding depth error less than 100  $\mu\text{m}$ . This would be comparable to the error on the 3D points obtained from the triangulation.

Consequently, we reconstruct the retinal surface as a plane with respect to the ASAP coordinates, by applying linear least squares fitting to the point cloud  $P_{beam3D}^i$  and also combining combined the fitting with RANSAC algorithm to eliminate noisy data. The plane is described by a point  $p_0$  lying on the plane and three principal components describing the plane,  $u$ ,  $v$ , and  $n$ , where  $u$  and  $v$  are orthonormal vectors lying on the plane and  $n$  indicates a surface normal. In addition, the planar homography is also derived in use of the 3D surface tracking.

## 6.3 Position-Based Visual Servoing

### 6.3.1 Control Principle

A goal position of the laser tip  $\mathbf{P}_{goal}$  is first defined for aiming at a target,  $\mathbf{P}_{target}$ , while maintaining a specific distance  $d_{lim}$  above the surface along the tip as in (6.6).

$$\mathbf{P}_{goal} = \mathbf{P}_{target} + d_{lim} \cdot \mathbf{n}_{tool}, \quad \mathbf{n}_{tool} = \frac{\mathbf{P}_{RCM} - \mathbf{P}_{target}}{|\mathbf{P}_{RCM} - \mathbf{P}_{target}|}, \quad (6.6)$$

where  $\mathbf{n}_{tool}$  is a unit vector of the laser probe and  $\mathbf{P}_{RCM}$  is the RCM. Given the combination of the goal and RCM positions for the tool in 3D space, only five degrees of freedom are needed for control; rotation along the tool axis is not taken into account during the operation. Accordingly, a specific orientation is only allowed to the laser probe, which is constrained primarily by the location of the RCM. The corresponding parameters and control procedure are also visualized in Fig. 6.6.

However, a small error in the tip position control may induce a large error between the target and the aiming beam on the surface, as the tip becomes far from the surface. Hence,

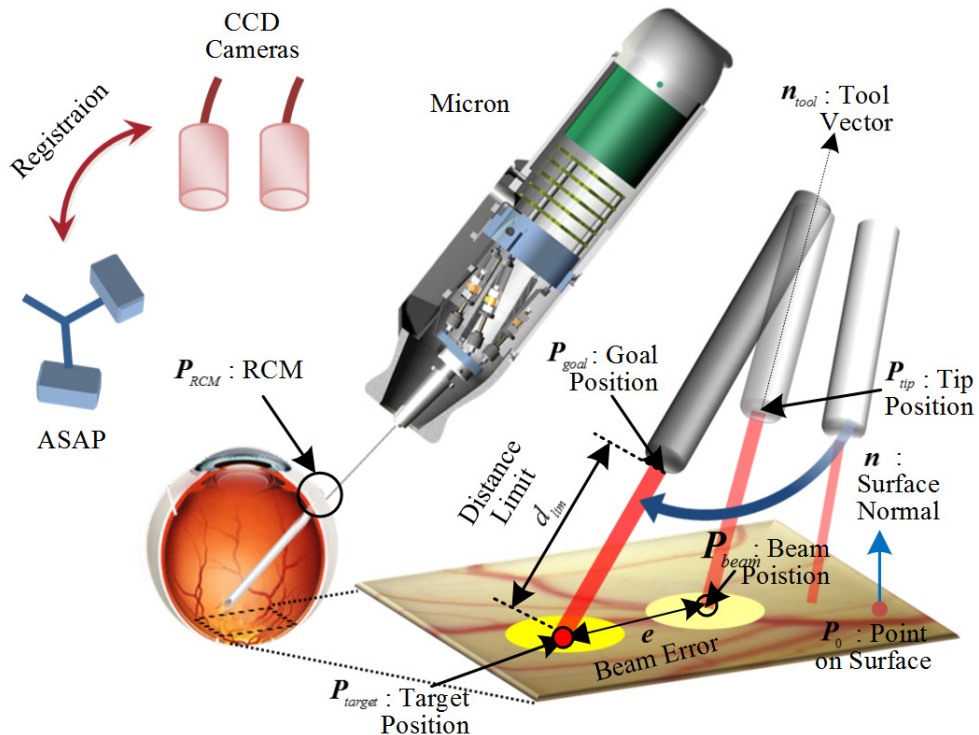


Fig. 6.5. Visualization of the control procedure.

we adopt a PD controller as in (6.7), in order to compensate for 3D error,  $\mathbf{e}$ .

$$\mathbf{P}_{goal} = \mathbf{P}_{tip} + P_k \cdot \mathbf{e} + P_d \cdot \Delta \mathbf{e}, \quad \mathbf{e} = \mathbf{P}_{target} - \mathbf{P}_{beam} \quad (6.7)$$

Since the PD controller only minimizes the beam error on the plane (i.e., no constraint on vertical motion along the normal), we still need to adjust the goal position, in order to maintain the distance limit. The point on the surface  $\mathbf{P}_{plane}$  is defined as the intersection of the ray along the laser probe with the plane, where the plane is described by a surface normal and a point on the surface ( $\mathbf{n}$  and  $\mathbf{P}_0$ ) in (6.8). Then, the axial distance from the surface  $d_{tip}$  is taken into account in the final goal position for keeping the distance limit as in (6.9).

$$d_{tip} = |\mathbf{P}_{plane} - \mathbf{P}_{tip}|, \quad \mathbf{P}_{plane} = \text{intersect}(\mathbf{P}_{RCM}, \mathbf{P}_{tip}, \mathbf{n}, \mathbf{P}_0) \quad (6.8)$$

$$\mathbf{P}_{goal\_new} \equiv \mathbf{P}_{goal} + (d_{lim} - d_{tip}) \cdot \mathbf{n}_{tool} \quad (6.9)$$

Both goal positions defined in (6.6) and (6.7) are selectively used in control because the aiming beam is not always visible. For instance, we fail to detect the aiming beam at the instant of laser firing, due to saturation on images. Furthermore, the beam is not reliably detected on a dark spot produced by a laser burn. Lastly, the visual servoing is slower than the control using a fixed goal position since the valid vision information is only allowed at 30 Hz; for the rest of the time, not receiving a new image, positions relying on vision system are estimated by a Kalman filter.

### 6.3.2 Surface Tracking

Tracking the retinal surface is an essential feature to accomplish the fully automated laser photocoagulation because of uncontrolled eye movement during operation [141], [149]. Since vitreoretinal surgeons manipulate the eye with a surgical tool to explore region of interest, and since the patient also may move the eye, the voluntary/involuntary motion is introduced to the eyeball, which causes movement in the microscope view of the retina [27]. To tackle this issue, we have developed an algorithm, called ‘eyeSLAM’, to both map and localize retinal vessels by temporally fusing and registering detected vessels in a sequence of frames [27]. Although eyeSLAM works on such a textureless surface, providing the 2D localization of the vessels at 30 Hz, it is still challenging to apply the algorithm in order to attain a 3D localization result in real time.

Thus, we propose a method to extend the 2D localization based on eyeSLAM to 3D, utilizing a planar homography for the surface. Once eyeSLAM provides the vessel map of the left camera image, the map of the right image is derived from the homography transformation  $\mathbf{H}$  in (6.10), being assumed as a plane.

$$\mathbf{p}_{vR} \equiv \mathbf{H}\mathbf{p}_{vL} \quad (6.10)$$

Given the vessel maps  $\mathbf{p}_{vL}$  and  $\mathbf{p}_{vR}$  of the left and right images, the corresponding 3D map  $\mathbf{P}_v$  is reconstructed via the triangulation of the maps as in (6.11).

$$\mathbf{P}_v = \Phi(\mathbf{p}_{vL}, \mathbf{p}_{vR}, \mathbf{M}_L, \mathbf{M}_R) \quad (6.11)$$

A common method to find a 3D transformation of such an amorphous point cloud is to run iterative closest point (ICP), but it is time-consuming due to the iteration. Hence, we utilize the 2D localization result of the left image to fully recover the 3D localization of the surface instead of applying ICP. Since the 2D localization is provided at each time step, we have a backward transformation  $(\mathbf{TR}_{2d\_local}^{t=k})^{-1}$  from time  $t = k$  to  $t = k-I$  using the successive forward transformations  $\mathbf{TR}_{2d}^{t=k-1}$  and  $\mathbf{TR}_{2d}^{t=k}$  as in (6.12).

$$(\mathbf{TR}_{2d\_local}^{t=k})^{-1} = \mathbf{TR}_{2d}^{t=k-1} \cdot (\mathbf{TR}_{2d}^{t=k})^{-1} \quad (6.12)$$

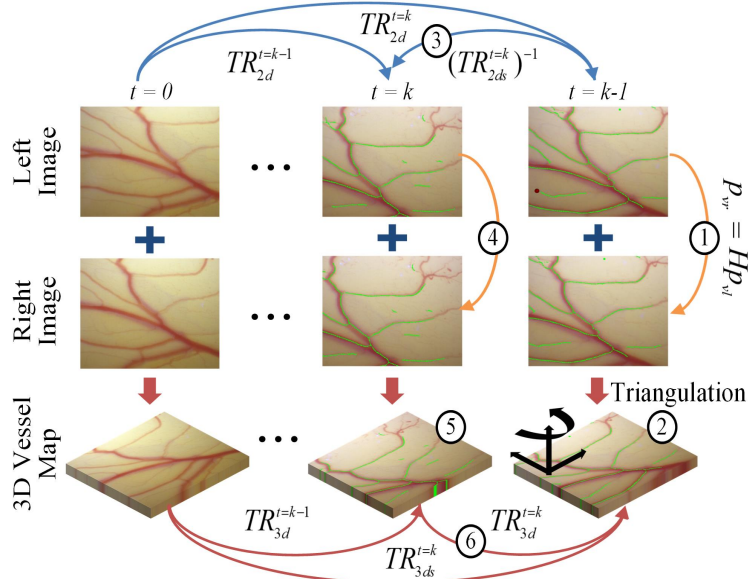


Fig. 6.6. 3D planar surface tracking, utilizing the 2D retinal vessel mapping and localization (eyeSLAM).

The vessel map on the left image at time  $t=k$  is transformed to the map at time  $t=k-1$  via the backward transform

$$\mathbf{P}_{vl}^{t=k-1} \equiv (\mathbf{TR}_{2d\_local}^{t=k})^{-1} \mathbf{P}_{vl}^{t=k} \quad (6.13)$$

The 3D vessel map  $\mathbf{P}_v^{t=k-1}$  at time  $t=k-1$  is also reconstructed using the homography mapping as we reconstruct the 3D vessel map  $\mathbf{P}_v^{t=k}$  at time  $t = k$ . Consequently, a 3D transformation between successive frames is attained from (6.10) without an effort to match an amorphous 3D point cloud.

$$\mathbf{P}_v^{t=k} \equiv \mathbf{TR}_{3d\_local}^{t=k} \mathbf{P}_v^{t=k-1} \quad (6.14)$$

The entire 3D transformation with respect to the initial position is acquired by cascading the 3D local transformations (6.15), which enables tracking of the moving surface.

$$\mathbf{TR}_{3d}^{t=k} = \mathbf{TR}_{3d\_local}^{t=k} \mathbf{TR}_{3d}^{t=k-1} \quad (6.15)$$

The overall procedures are illustrated in Fig. 6.6.

## 6.4 Experiments and Results

Multiple ring patterns are introduced in our experiments, as a typical arrangement for diabetic macular edema [38]. The targets are spaced 600  $\mu\text{m}$  along the circumferences of multiple circles: 1, 2, and 3 mm in diameter. The total number of the targets planned in a single trial was 32. To burn the targets on a paper slide, the power of the laser was set as 3.0 W with a duration of 20 ms; the colored background of the paper is a good absorptive material for the laser, yielding distinct black burns [26].

### 6.4.1 Control Performance

We investigate the control performance of the system according to various error thresholds to trigger laser firing. This aims to find an acceptable threshold, taking into account accuracy and execution time. The manipulator was firmly affixed to a solid base, in order to eliminate other disturbances such as hand tremor. The tests were repeated for three trials and averaged, given thresholds of 20, 50, and 100  $\mu\text{m}$ , resulting in the total 96 burns. The error was evaluated by the calculation of the 2D distance between the target and actual burn locations. The burn location was found using either fitting an ellipse on a black spot or  $K$ -means clustering to distinguish adjoining spots. A green enclosure indicates the fitted ellipse and the blue dot is each center of the  $K$ -means clustering in resulting figures.

The average errors are measured in a range of 26–30  $\mu\text{m}$  for all settings. The standard deviations slightly increase from 11 to 14  $\mu\text{m}$  as the threshold become larger. However, the execution time decreases from 31.9 to 21.4 s. Given the results, there is no statistically significant difference between the thresholds, 20  $\mu\text{m}$  and 50  $\mu\text{m}$ , in terms of the average

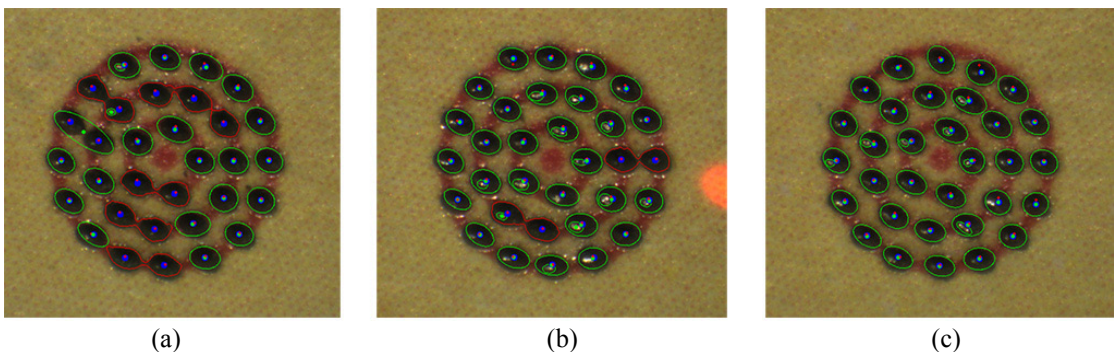


Fig. 6.7. Automated laser photocoagulation results according to various control thresholds on a fixed paper slide under a clamped condition: 20 (a), 50 (b), and 100  $\mu\text{m}$  (c). The red circles are overlaid as the indication of pattern sizes: 1, 2, 3 mm in diameter.

TABLE 6.1. SUMMARY OF EXPERIMENTAL RESULTS FOR AUTOMATED LASER PHOTOCOAGULATION

Type	Clamped			Handheld				Eye Phantom
	20 $\mu\text{m}$	50 $\mu\text{m}$	100 $\mu\text{m}$	0.5 Hz	1.0 Hz	50 $\mu\text{m}$	100 $\mu\text{m}$	
Setting <sup>a</sup>								
Avg. <sup>b</sup>	26	26	30	102	104	36	38	65
Std. <sup>b</sup>	11	13	14	57	55	19	19	32
Max. <sup>b</sup>	69	73	103	250	265	109	96	175
Time <sup>c</sup>	31.9	24.2	21.4	64.0	32.0	44.0	22.9	23.9

<sup>a</sup>The distance value for a threshold used in the automated trial.

<sup>b</sup>The frequency for a repetition rate set in the manual trial.

<sup>b</sup>The unit of error value is in  $\mu\text{m}$ .

<sup>c</sup>The unit of time is in s.

error. However, the difference is noticeable in execution times: decrease from 31.0 to 24.2 s. Although the average error with 100  $\mu\text{m}$  threshold is, of course, larger than the errors with the other lower thresholds, it is still acceptable in laser photocoagulation, compared to the size of the laser spot (200–400  $\mu\text{m}$ ). The representative results are presented in Fig. 6.7 and the analysis details are summarized in Table 6.1.

#### 6.4.2 Handheld Performance

We also evaluated the handheld performance of the automated system, comparing with manual operation, under a board-approved protocol. The user was not a trained surgeon. In manual operation, the laser was fired at a fixed rate, as is typical in laser surgery. The repetition rates were set to be 0.5 and 1.0 Hz, since acceptable results were attainable only with the rate below 1.0 Hz. For the automated trials, the thresholds were set to be 50 and 100  $\mu\text{m}$  from the results of the accuracy tests performed under the clamped setting. We also repeated these tests for three trials and averaged the errors.

In the automated trials, there is no statistically significant difference in terms of the average error between the thresholds, although it exists in the clamped tests. Noticeably, the execution time drops from 44.0 to 22.9 s with the higher threshold, whereas it was similar under the clamped condition (24.2 and 21.4 s, respectively). This is because hand tremor involved in these tests leads the control system to reset the laser triggering and repeat it, in order to satisfy such a small threshold, which is subject to the increment in execution time. In the manual trials, the average errors are about 100  $\mu\text{m}$  for both 0.5 and 1.0 Hz repetition rates as shown in Fig. 6.8 (without a statistically significant difference),

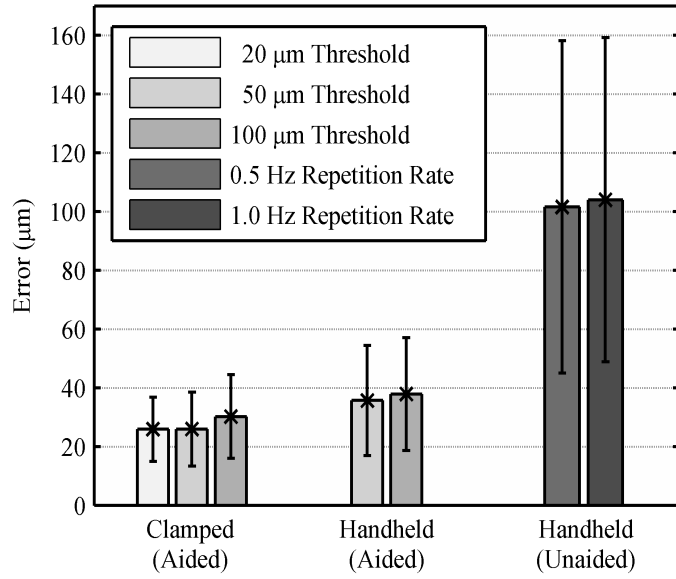


Fig. 6.8. Average errors for different tasks and settings, with error bars.

although the execution time is doubled with the 0.5 Hz repetition rate. Comparing the automated operation (100- $\mu\text{m}$  thresholds) to manual operation (1.0 Hz), the average error is reduced by 63.5% ( $p = 1 \times 10^{-12}$ ): from 104 to 38  $\mu\text{m}$ . The execution time is also decreased from 32.0 to 22.9 s ( $p = 2 \times 10^{-5}$ ). Representative results are presented in Fig. 6.9 and the overall results are summarized in Table 6.1.

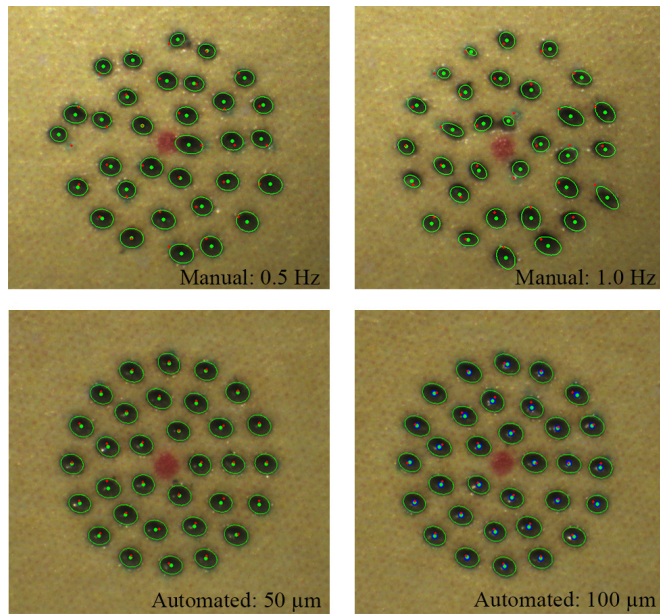


Fig. 6.9. Handheld performance on a fixed paper slide: automated vs. manual. The top row shows the results of the unaided trials with 0.5 and 1.0 Hz. The bottom presents the results of the automated trials with 50 and 100  $\mu\text{m}$  control thresholds.

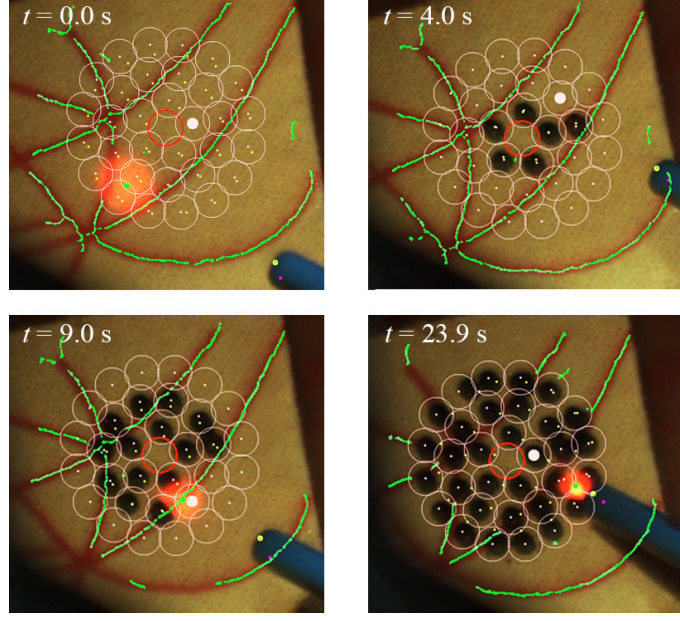


Fig. 6.10. Demonstration of the automated intraocular laser photocoagulation in an eye phantom. The pink circles indicate the preplanned targets lying on the inner surface of the eye phantom. The green lines represent the artificial vein map as detected by the eyeSLAM algorithm, which tracks the vessels throughout the operation.

#### 6.4.3 Eye Phantom

We used an eye phantom developed by Johns Hopkins University in order to evaluate the performance of the automated system on moving targets. The eye phantom consists of a hollow 25-mm-diameter sphere molded from soft silicone to mimic the natural sclera. The eye phantom was allowed to freely rotate in a ball cup treated with water-based lubricant (K-Y® jelly) as shown in Fig. 6.2. We attached a piece of a paper slide on the inner surface of the eye phantom to make a burn and analyze the accuracy. Based on the handheld experiments conducted on the fixed targets, we adopted 100  $\mu\text{m}$  as the appropriate threshold for this experiment in terms of accuracy and execution time. To compensate for eye movement, the preplanned targets were tracked during the task. The average error for three trials is 65  $\mu\text{m}$ , which is larger than the result obtained on the fixed surface. Nevertheless, there is no significant increment in the execution time between the trials on the moving and fixed targets. Fig. 6.10 shows the resulting burns according to different time stamps, while successfully tracking the targets during the operation.

## 6.5 Summary

We presented the automation of intraocular laser surgery using a newly developed 6-DOF handheld micromanipulator. The 4-millimeter range enables the automated scanning of the laser probe, regulating the height of the probe from the retinal surface. The simultaneous calibration method contributes to improving the accuracy of the coordinate registration. In addition, the 3D tracking feature realizes the automated operation in a moving target such as in the eye phantom. As a result, the feasibility of automated intraocular photocoagulation was demonstrated in an eye phantom while tracking the movement of the retina and also maintaining a constant standoff distance from the retina.

Compared to the semiautomated laser surgery using the 3 DOF Micron [26], the accuracy is significantly improved, providing 63.6% of error reduction between the manual operation with 1.0 Hz repetition rate and the automated operation with 100  $\mu\text{m}$  threshold; the semiautomated system showed 22.3% error-reduction. Furthermore, the new manipulator allows automated depth control, which was not featured in the semiautomated system due to the limited workspace of the manipulator used, especially along the axis of the tool. This is an important factor for ensuring safety operation and also for reducing the cognitive burden of the surgeon.

However, further developments are still required to apply the automated system in real vitreoretinal surgery. For instance, any large error in initial calibration may lead to the failure of servoing, because the control system relies primarily on the calibration and corresponding reconstruction of the target surface. Moreover, the automated operation is susceptible to actuator saturation, since hand-eye coordination is interrupted; during the several seconds of automated execution, the operator can easily drift to the edge of the reachable workspace without knowing it.



## 7 ROBOT-AIDED INTRAOCULAR LASER SURGERY

### II: HYBRID VISUAL SERVOING

In this chapter, we introduce hybrid visual servoing for robot-aided intraocular laser surgery, incorporating an adaptive framework to mitigate calibration problems and to improve control.

As discussed earlier, the initial prototype of the automated system still entails several drawbacks. First, the system requires accurate camera calibration and stereo reconstruction for position-based visual servoing. In that system, the servoing performance thus varied substantially depending on the accuracy of the 3D reconstruction used for describing all necessary points, such as the aiming beam and targets, and for modeling the retinal surface. Furthermore, the automated system is susceptible to actuator saturation, since manual drift is compensated and thus invisible to the operator. Accordingly, the preliminary work was limited to a single demonstration in the eye phantom without further quantitative evaluation.

To address these issues, we adopt the hybrid visual servoing which has been suggested in visual servoing research, as a compromise between position-based and image-based visual servo controls [150], [151]. A custom-built graphical overlay system in the operating microscope is also used, in order to maintain hand-eye coordination during the time of automated execution. In addition, intraoperative anatomical tracking is implemented in order to provide automatic enforcement of avoidance zones, which prevents regions such as retinal vessels or the fovea from being mistakenly photocoagulated.

Finally, its effectiveness is evaluated by trained vitreoretinal surgeons in a realistic eye phantom environment through a 23-gauge cannula based sclerotomy. We also perform comparative evaluation of automated, semiautomated, and unaided manual intraocular laser surgery with various control methods.

## 7.1 System Overview

Most of hardware setups for the new robot-aided laser photocoagulation system are identical to the initial system described in Section 6.2. The robot-aided intraocular laser photocoagulation system primarily comprises the active handheld robot, Micron, the vision system, and the laser with the endoprobe, as shown in Fig. 7.1(a). Given image streams from two CCD cameras, 2D tip and aiming beam positions are detected by image processing. The 2D tip position is then used for system calibration between the cameras and the Micron control system. The aiming beam of the laser is used for visual servoing of the laser tip. In addition, the vision system is capable of tracking the retinal surface using the ‘eyeSLAM’ algorithm [27] for compensation of eye movement. For laser

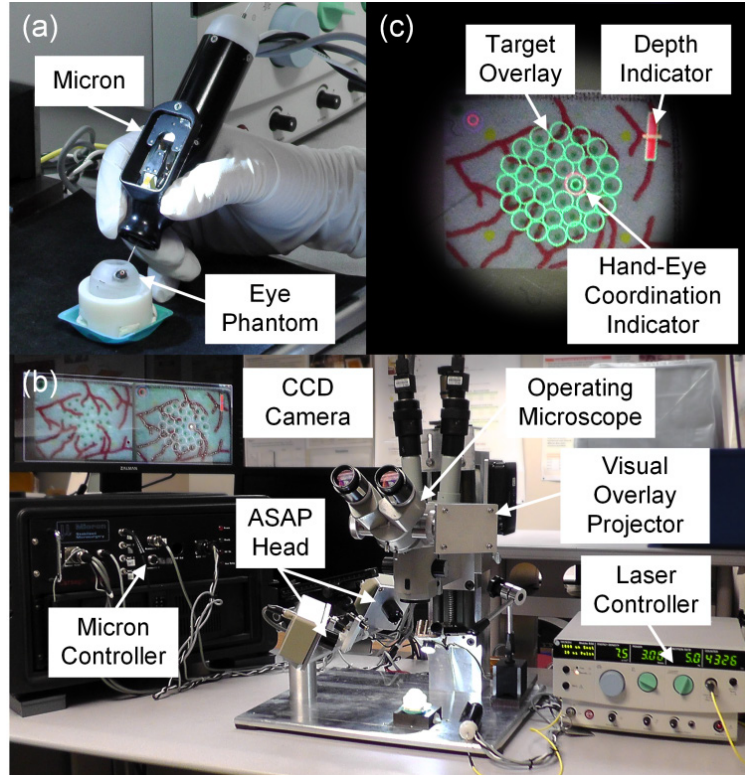


Fig. 7.1. Automated intraocular laser surgery system. (a) Handheld instrument (Micron) and eye phantom. (b) Overall system setup, including the Micron controller, the operating microscope, the graphical overlay system, and the laser controller. (c) Graphical overlays shown through the right eyepiece of the operating microscope. The green circles indicate the targets. The red bar at the upper right corner is the depth indicator representing the height of the laser probe from the retinal surface. The red circle on a target is the guidance cue to maintain the hand-eye coordination. The location and size of the circle represent the lateral and vertical positions of the laser probe, respectively.

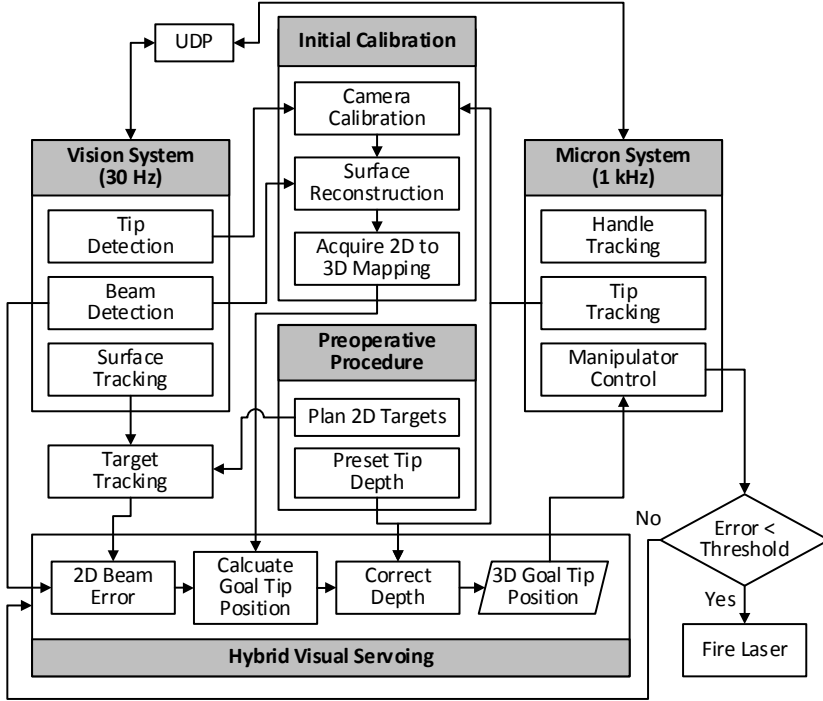


Fig. 7.2. Block diagram of the system, showing data and execution flow.

photocoagulation, an Iridex 23-gauge EndoProbe is attached to the tool adaptor of Micron, and an Iridex Iriderm Diolite 532 Laser is interfaced with the Micron controller. Fig. 7.1(b) shows the overall setup with the Micron, vision, and laser systems.

Once patterned targets are placed on a preoperative image, the laser probe is then deflected to correct 2D error between the aiming beam and the given target. During the operation, the system also maintains a constant standoff distance of the laser probe from the retinal surface. As the distance between the aiming beam and the target comes within a specified targeting threshold, the laser is triggered. Once laser firing is detected via image processing, the procedure is repeated until completion of all targets. Alternatively, the robot-aided execution can use a fixed repeat rate in place of a targeting threshold, as is normally used for manual operation. This control mode thus allows direct comparison with unaided operation. For this comparative study, we also implemented the semiautomated control algorithm used in [26], in which automatic control engages whenever the aiming beam comes within 200  $\mu\text{m}$  of an untreated target. It is particularly useful for treating a large area with laser photocoagulation because the operation is not limited by the specific range of motion of the manipulator. The overall control flow is depicted in Fig. 7.2.

### 7.1.1 Graphical Overlay System

The new automated system is also equipped with a monocular graphical overlay system in the operating microscope [135], since surgeons are much more accustomed to operating with the microscope. Overlaid graphical cues include the preoperative targets, the distance of the laser tip from the retinal surface, and instructive cues to maintain hand-eye coordination. The locations of the targets are displayed as a set of circles and the distance is represented as an indication bar, as shown Fig. 7.1(c).

To maintain hand-eye coordination during the time of robot-aided operation, two guidance cues are introduced. The first circular cue on the top-left corner of the screen represents the current displacement of the tool tip with respect to the nominal position in the manipulator. Hence, the cue is useful to prevent the manipulator from being saturated by reaching out of its workspace. The second cue overlaid on a current target shows the displacement of the null position with respect to the initial null position given at the beginning of a trial, where the null position is what the tip location would be if the actuators were turned off. The second cue is thus informative to keep hand-eye coordination, providing the operator with a virtual representation of the displacement of the instrument. As long as the operator keeps the position within a certain range of the initial position, the automated system can correct the errors and control the depth of the tool without reaching the edge of the workspace. To enhance perception of the displacement in 3D, it is represented in the display as a circle whose location and diameter correspond to lateral and vertical displacements, respectively (a larger circle indicates greater height, closer to the viewer, and vice versa). For seamless robot-aided operation, the operator is instructed to perform a hold-still task by keeping the second red circle centered as much as possible and maintaining a fixed size of the circle, with the blue circle as a reference. However, following these instructions is not strictly required as long as the manipulator is operating inside its workspace, as indicated in the first cue.

In order to project overlay patterns into the operating microscope, we also need to register the visual overlay system attached to the microscope with the vision system. This calibration is to find a mapping between a virtual image created on the right eyepiece and an actual image captured by the right CCD camera. We use a planar homography  $\mathbf{H} \in \mathbb{R}^{3 \times 3}$  for the mapping, given by manually matching several points seen through the microscope with those on the right CCD image:  $\mathbf{p}_{proj} \equiv \mathbf{H}\mathbf{p}_{CCD}, \forall i \in [1, k]$ , where  $k$  is the number of correspondences. As a result, virtual images created by the PC are overlaid on the right eyepiece with the targets via the homogenous transformation  $\mathbf{H}$ , as shown in Fig. 7.1(c).

## 7.2 Hybrid Visual Servoing

### 7.2.1 Control Principle

We propose a hybrid control scheme for robot-aided intraocular laser surgery, in order to address the issues raised by position-based visual servoing, specifically, due to inaccurate stereo-reconstruction of the aiming beam and retinal surface, including placed targets. Any large error in the calibration procedure may lead to failure of the servoing, which is a weakness of such position-based visual servoing [152]. In the hybrid control, only selected degrees of freedom are controlled using visual servo control, and the others use position servo control. Castaño and Hutchinson introduced a hybrid vision/position control structure called *visual compliance* [153]. Specifically, the 2-DOF motion parallel to an image plane is controlled using visual feedback, and the remaining degree of freedom (perpendicular to the image plane) is controlled using position feedback provided by encoders.

To apply such a partitioned control scheme to our system, the 3-DOF motion of the tool tip is decoupled into the 2-DOF planar motion parallel to the retinal surface and the 1-DOF motion along the axis of the tool. The decoupled 2-DOF motion is then controlled via image-based visual servoing, to locate the laser aiming beam onto a target position using a monocular camera. The 1-DOF axial motion is controlled to maintain a constant standoff distance from the estimated retinal surface.

The first step is to register the CCD cameras with the Micron control coordinates (called herein the “ASAP coordinates”) by sweeping the tool above the retinal surface as described in Section 6.2.1. Given multiple correspondences between 2D and 3D tip positions, projection matrices are obtained for the left and right cameras  $\mathbf{M}_c$  as in (7.1).

$$\mathbf{p}_{tip}^{image} \equiv \mathbf{M}_c \mathbf{P}_{tip}^{ASAP}, \quad \forall c \in \{\text{L, R}\}, \quad (7.1)$$

where  $\mathbf{p}_{tip}^{image}$  and  $\mathbf{P}_{tip}^{ASAP}$  are 2D and 3D ASAP tip positions, respectively. We also reconstruct the 3D beam points that belong to the retinal surface via triangulation of aiming beams detected on images. The retinal surface is then described as a plane by linear least squares fitting on the 3D points, assuming a small area of interest within the eyeball. The resulting plane is thus defined in the ASAP coordinates in terms of a point  $\mathbf{P}_0$  belonging to the surface, and principal components,  $\mathbf{u}$ ,  $\mathbf{v}$ , and  $\mathbf{n}$ . The orthonormal vectors  $\mathbf{u}$  and  $\mathbf{v}$  lies on the plane, and  $\mathbf{n}$  indicates a surface normal.

For image-based visual servoing, we formulate an analytical image Jacobian instead of using feature points on images, since it is extremely challenging to robustly extract the feature points during intraocular operation. We first assume that the image plane is parallel to the retinal surface (regarded as a task plane), resulting in an interaction matrix  $\mathbf{J}_p \in \mathbb{R}^{2 \times 2}$  for differential motions, as in (7.2).

$$\Delta\mathbf{x}^{image} = \mathbf{J}_p \Delta\Theta^{task}, \quad (7.2)$$

where  $\Delta\mathbf{x}^{image}$  and  $\Delta\Theta^{task}$  are differential motions in image and task planes, respectively. Herein, the task space  $\Theta_{plane}$  defined at the ASAP coordinates is subject to the plane that models the retinal surface. The 2-DOF planar motion of the laser tip is thus allowed above the task space, where the tip motion is assumed to be parallel to the task space within a small range of motion.

To derive the interaction matrix  $\mathbf{J}_p$ , two differential motions are taken in the task plane with respect to the 3D point  $\mathbf{P}_0$  lying on the surface, using the orthonormal bases of the plane,  $u$  and  $v$ :

$$\mathbf{P}_u - \mathbf{P}_0 = u \text{ and } \mathbf{P}_v - \mathbf{P}_0 = v. \quad (7.3)$$

The corresponding differential motions in the image plane,  $\Delta\mathbf{p}_u$  and  $\Delta\mathbf{p}_v$  are then defined, using the projection matrix of the left camera in (7.4):

$$\Delta\mathbf{p}_u = \mathbf{M}_L \mathbf{P}_u - \mathbf{M}_L \mathbf{P}_0 \text{ and } \Delta\mathbf{p}_v = \mathbf{M}_L \mathbf{P}_v - \mathbf{M}_L \mathbf{P}_0. \quad (7.4)$$

Hence, the matrix  $\mathbf{J}_p$  between the task and image coordinates is composed by the two vectors,  $\Delta\mathbf{p}_u$  and  $\Delta\mathbf{p}_v$ , as in (7.5).

$$[\Delta\mathbf{p}_u \quad \Delta\mathbf{p}_v] = \mathbf{J}_p \mathbf{I}^{2 \times 2}, \quad (7.5)$$

where  $\mathbf{I}^{2 \times 2}$  is an identity matrix; the differential motions in the task space,  $u$  and  $v$ , are subject to canonical bases with respect to the task plane coordinates. The inverse of the interaction matrix,  $\mathbf{J}_p^{-1}$ , is obtained by taking the inverse of the matrix  $[\Delta\mathbf{p}_u \quad \Delta\mathbf{p}_v]$  that has full rank. The inverse matrix can also be decomposed by the magnitude and direction of mapping between the image and task plane coordinates as in (7.6).

$$\mathbf{J}_p^{-1} = \begin{bmatrix} s_x & 0 \\ 0 & s_y \end{bmatrix}^{-1} \begin{bmatrix} \Delta\mathbf{p}_u & \Delta\mathbf{p}_v \\ |\Delta\mathbf{p}_u| & |\Delta\mathbf{p}_v| \end{bmatrix}^{-1}, \quad (7.6)$$

where scale factors,  $s_x$  and  $s_y$ , are defined by  $|\Delta\mathbf{p}_u|$  and  $|\Delta\mathbf{p}_v|$ , respectively. It is noted that

the scale factors can be substituted by zoom factors for a corresponding magnification of the operating microscope, while preserving the direction of motion. Hence, it would be useful for accommodating zoom optics frequently used in intraocular surgery.

To control the tool tip in the ASAP coordinates, we extend the 2D vector  $\Delta\Theta^{task}$  to the 3D vector  $\Delta\mathbf{X}^{plane}$  using the orthonormal bases of the plane described in the ASAP coordinates:

$$\Delta\mathbf{X}^{plane} = [\mathbf{u} \quad \mathbf{v}] \Delta\Theta^{task}. \quad (7.7)$$

Since the tool tip is located above the plane by  $d_{surf}$ , the actual displacement of the tool tip, corresponding to the motion of the aiming beam on the plane, is scaled down by the ratio of the lever arms,  $r_{lever} = d_{RCM} / (d_{RCM} + d_{surf})$ :

$$\Delta\mathbf{X}_{tip}^{actual} = r_{lever} \Delta\mathbf{X}_{tip}^{plane}, \quad (7.8)$$

where  $d_{RCM}$  is the distance of the tool tip from the RCM. Small angular motion pivoting around an RCM is assumed, as the displacement of the aiming beam is much smaller than the distance of the tool tip from the RCM. Finally, an image Jacobian  $\mathbf{J}$  is derived for visual servoing, given an error  $\Delta\mathbf{e}_{beam}^{image}$  between target and current beam positions on the image plane:

$$\Delta\mathbf{E}_{tip}^{ASAP} = \mathbf{J}^{-1} \Delta\mathbf{e}_{beam}^{image}; \quad (7.9)$$

$$\mathbf{J}^{-1} = r_{lever} [\mathbf{u} \quad \mathbf{v}] \mathbf{J}_p^{-1}. \quad (7.10)$$

The goal position of the tool tip is set by a PD controller as in (7.11), subject to minimizing the error between the current aiming beam and the target positions.

$$\mathbf{P}_{goal} = \mathbf{P}_{tip} + p_k \Delta\mathbf{E}_{tip} + p_d \Delta \dot{\mathbf{E}}_{tip} \quad (7.11)$$

When the aiming beam reaches the target via visual servoing, we still have a remaining degree of freedom along the axis of the tool in control. Hence, this 1-DOF motion is regulated to maintain a specific distance  $d_{lim}$  between the tool tip and the retinal surface. Consequently, we incorporate a depth-limiting feature with image-based visual servoing in our control to fully define the 3-DOF motion of the tool tip, as in (7.12).

$$\mathbf{P}_{goal\_3dof} = \mathbf{P}_{goal} + (d_{lim} - d_{surf}) \cdot \mathbf{n}_{tool}, \quad (7.12)$$

where  $\mathbf{n}_{tool}$  is a unit vector describing the axis of the tool. As a result, the 2D error is subject to being minimized via the visual servoing loop, while the distance of the tool tip from the

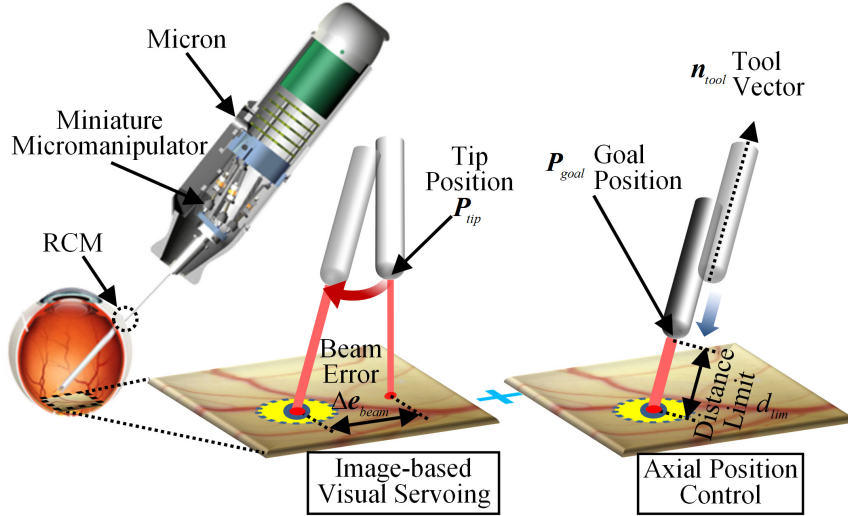


Fig. 7.3. Visualization of the control procedure. The 2D beam error is minimized by image-based visual servo control parallel to the retinal surface, while maintaining the predefined distance of the laser tip from the retinal surface along the axis of the probe.

retinal surface is regulated by the position control loop. The corresponding parameters and control procedure are also depicted in Fig. 7.3.

### 7.2.2 Image Jacobian Update

Our control scheme also incorporates an image Jacobian update during control in order to compensate any error in deriving such an analytical and static Jacobian. Although image-based visual servoing is achievable with an inaccurate Jacobian, the update framework is still beneficial to increase operation speed and particularly to avoid erroneous movement of the tool tip in microsurgery.

Jacobian estimation has been widely adopted for uncalibrated visual servoing [154]–[157]. The first approach was to apply an exponentially weighted recursive least-squares (RLS) update for Jacobian estimation [154]. Jagersand *et al.* presented a nonlinear least-squares optimization method using a trust-region method and Broyden estimation [155]. However, these earlier works demonstrated the feasibility of uncalibrated visual servoing only for stationary targets. Later, Piepmeyer *et al.* introduced dynamic visual servo control for target tracking [156].

In our control, an initial goal position for the tip is set primarily by the image Jacobian derived as in (7.9), which acts as an open-loop controller. The feedback controller in (7.11)

is then applied, in order to correct the remaining error between the target and current beam positions. This switching scheme is particularly crucial to address issues raised by unreliable beam detection, especially saturation in images at the instant of laser firing. Accordingly, accurate Jacobian mapping would reduce error in the open-loop control, leading to minimal closed-loop control. In addition, the accurate Jacobian allows us to apply high gains to the control without losing stability, which is desirable for control of such a handheld manipulator.

Hence, we update the inverse of the partial Jacobian  $\mathbf{J}_p^{-1}$  primarily to compensate the error given by the open-loop control. First, we define a desired displacement of the aiming beam  $\Delta\mathbf{x}_{beam}^{desired}$  from a previous target to the next one.

$$\Delta\mathbf{x}_{beam}^{desired} = r_{lever}(\mathbf{x}_{final} - \mathbf{x}_{init}) \quad (7.13)$$

The actual displacement of the tool tip is also defined as  $\Delta\mathbf{P}_{tip}^{actual}$  in the ASAP coordinates as below.

$$\Delta\mathbf{P}_{tip}^{actual} = \mathbf{P}_{final} - \mathbf{P}_{init} \quad (7.14)$$

Using Broyden's method [155], a new inverse Jacobian  $\left[\mathbf{J}_p^{-1}\right]^{k+1}$  is formulated:

$$\left[\mathbf{J}_p^{-1}\right]^{k+1} = \left[\mathbf{J}_p^{-1}\right]^k + \frac{(\Delta\mathbf{P}_{tip} - \mathbf{J}_p^{-1}\Delta\mathbf{x}_{beam})\Delta\mathbf{x}_{beam}^T}{\Delta\mathbf{x}_{beam}^T \Delta\mathbf{x}_{beam}}; \quad (7.15)$$

$$\Delta\mathbf{P}_{tip} = \begin{bmatrix} \mathbf{u}^T \Delta\mathbf{P}_{np} & \mathbf{v}^T \Delta\mathbf{P}_{tip} \end{bmatrix}^T. \quad (7.16)$$

## 7.3 Experiments and Results

### 7.3.1 Experimental Setup

We used an eye phantom made of a hollow polypropylene ball with 25-mm diameter, in order to evaluate the performance of the automated system on moving targets. The portion presenting the cornea was open, and the sclerotomy locations for insertion of a light-pipe and the tool are formed by rubber patches. The eye phantom can freely rotate in a ball cup treated with water-based lubricant (glycerin and hydroxyethyl cellulose), as shown in Fig. 7.1(a). A slip of paper was attached to the inner surface of the eye phantom, as a target surface for burns.

Multiple ring patterns were also introduced in our experiments, as a typical arrangement for the treatment of proliferative retinopathy [38]. The targets were uniformly placed 600  $\mu\text{m}$  apart around the circumference of rings 1, 2, and 3 mm in diameter. The arrangement thus provided 5, 11, and 16 targets on each circle, respectively, for a total of 32 targets per trial. As an indication of the targets, 200- $\mu\text{m}$  green dots were printed on the paper slide so that they were used for targeting cues in manual trials. In addition to the circular arrays of targets, artificial blood vessels were also printed on the paper. This artificial vasculature allows tracking the movement of the eye, based on the eyeSLAM algorithm [27]. We also introduced four fiducial markers outside the targets to align the preoperative targets with the printed green dots. After completion of automated trials, the markers were postoperatively re-aligned to provide the ground truth for further evaluation. Hence, we evaluated errors caused by both control and tracking performance.

For laser photocoagulation, an Iridex 23-gauge EndoProbe was attached to the tool adaptor of Micron and an Iridex Iriderm Diolite 532nm Laser (Iridex, Mountain View, CA) was interfaced with the Micron controller. To burn the targets on a paper slide, the power of the laser was set at 3.0 W with a duration of 20 ms.

We evaluated the performance of the automated system, comparing with manual operation, under a board-approved protocol. Two retinal surgeons participated in the experiments; one had prior experience with Micron, whereas the other did not. For automated operation, the targeting thresholds to trigger laser firing were set in a range of 50–200  $\mu\text{m}$ , in order to investigate the effectiveness of the operation in terms of accuracy and execution time. In manual operation, the laser was fired at a fixed rate, regardless of convergence on the target, as is typical in intraocular laser surgery. According to typical settings used clinically, the firing rates were in the range 1.0–2.5 Hz with a step increment of 0.5 Hz. We also repeated these tests for three trials.

To demonstrate the avoidance feature, we applied the eyeSLAM algorithm, capable of identifying blood vessels. The ring patterns used in performance evaluation were also placed on the eye phantom, but the system was programmed not to treat any target within a distance of 200  $\mu\text{m}$  from the vessels identified. This limit of 200  $\mu\text{m}$  was selected based on the size of a laser burn and the targeting threshold; since the radius of a burn is approximately 150  $\mu\text{m}$ , and the targeting threshold was set to be at least 50  $\mu\text{m}$ , the edge of the burn could potentially touch a blood vessel located 200  $\mu\text{m}$  from the center of a target.

### 7.3.2 Data Analysis

To evaluate the accuracy of operation for each trial, the resulting image was binarized to identify black dots, and then underwent  $K$ -means clustering to find the centroid of each burn. Nearest-neighbor matching was then used to find corresponding targets. Since preoperative targets are subject to moving during operation, the targets were re-aligned after completion of each task for the error analysis, using the fiducial markers printed on the paper slide. Hence, we were allowed to evaluate the overall error composed of both positioning and tracking errors, by calculation of the 2D distance between the target and actual burn locations. In addition, the execution time of each trial was measured, and also represented as an equivalent frequency of burns per second.

We collected the data from 48 trials in total, given that the two subjects repeated each of the four test conditions of the automated and manual operation modes three times. As a result, 6 frequency measurements and 192 burn errors were obtained for each test condition, and then averaged for further analysis.

Two-sample  $t$ -tests were conducted to examine statistical differences between automated and manual operation, and also differences between the subjects in each control setting. Since frequencies obtained from the automated trials were not necessarily equal to those used in the manual trials, the average error and standard deviation were interpolated within a frequency range of 1.0–1.75 Hz with a 0.25-Hz step size in order to run the  $t$ -tests under equivalent frequency settings.

In addition to the error analysis, we dealt with invalid or spurious burns, which were found particularly in manual trials. For example, the operator sometimes failed to burn a target due to lack of energy delivered from the laser probe because the probe was too far from the retinal surface; this is noted as “untreated” in our analysis. Moreover, we call any burn “misaimed” if the error is greater than the half of the target spacing (i.e., 300  $\mu\text{m}$ ) or

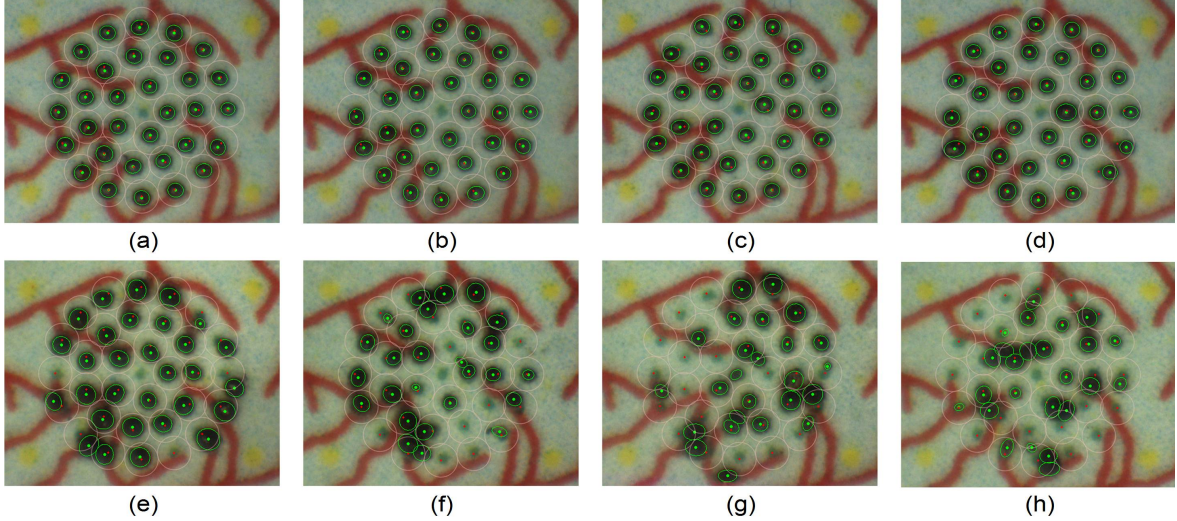


Fig. 7.4. Results from eye phantom trials. The top row (a–d) presents automated trials with targeting tolerances of 50–200  $\mu\text{m}$ : (a) 50  $\mu\text{m}$ , (b) 100  $\mu\text{m}$ , (c) 150  $\mu\text{m}$ , and (d) 200  $\mu\text{m}$  targeting threshold. The bottom row (e–h) shows manual trials with laser repeat rates of 1.0–2.5 Hz: (e) 1.0 Hz, (f) 1.5 Hz, (g) 2.0 Hz, and (h) 2.5 Hz repetition rate.

if multiple burns are aggregated around a single target, such that a misaimed burn would be totally off from an originally aimed target, or would be closer to other targets than the aimed target. Thus, only detectably one-to-one correspondences between burns and targets were taken into account in the data analysis.

### 7.3.3 Results

Fig. 7.4 shows representative results from automated and manual trials. In the automated trials, the visibly regular sizes of burns are attained, whereas the sizes vary considerably in the manual trials because of the difficulty in maintaining a consistent distance from the target surface.

Fig. 7.5 presents average error from automated trials in blue, with error bars indicating standard deviation. The average error gradually increases from  $45 \pm 27$  to  $60 \pm 37$   $\mu\text{m}$  as the targeting threshold increases from 50 to 200  $\mu\text{m}$ , while execution time drops from 46.6 to 18.7 s (i.e., effective frequency increases from 0.69 to 1.71 Hz). There is no statistically significant difference in average error between the subjects for each threshold setting in the automated trials ( $p$  ranges from 0.10 to 0.64). Fig. 7.6 shows the normalized histograms of error for the total 192 burns measured in each setting. According to the distributions, the errors in automated operation are tightly clustered around the average, shown as a vertical

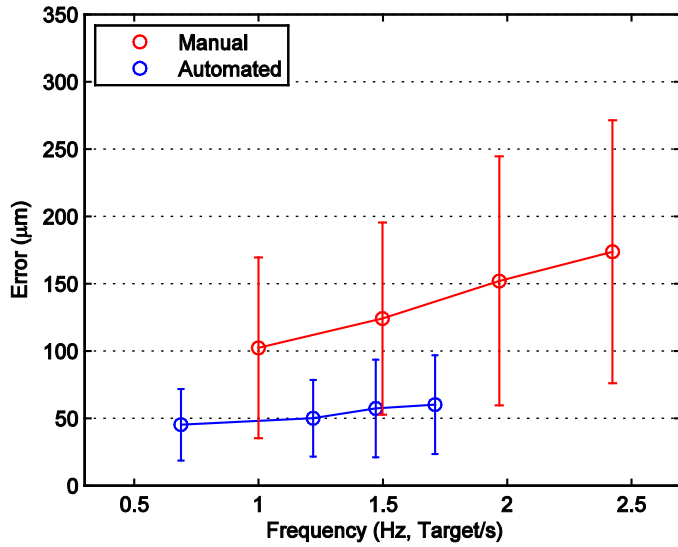


Fig. 7.5. Overall mean error for automated and manual trials at various speeds. Error bars indicate standard deviations from the analysis of the total 192 burns at each setting.

green line.

It is noted that the error is sometimes noticeably lower than the targeting thresholds specified, due to internal latency within the laser system, between triggering of the system and actual firing of the laser. The laser probe is thus kept in control during the delay (about

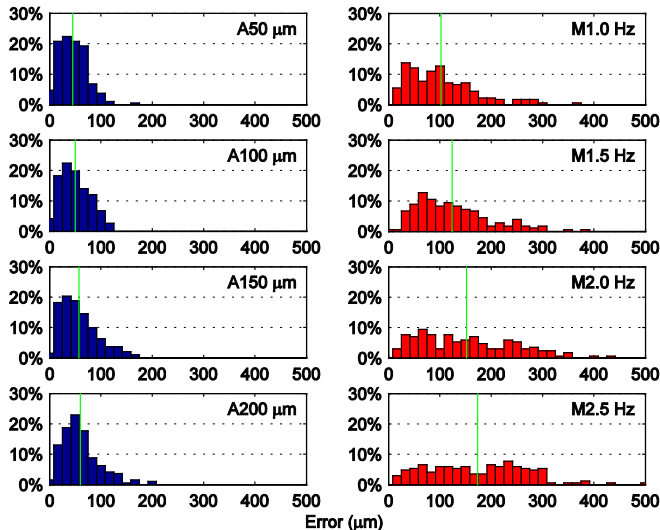


Fig. 7.6. Normalized histograms of error for automated and manual trials. The left column shows the normalized histograms of error obtained in the automated trials. The right column shows the normalized histograms of error for the manual trials. A green vertical line indicates the mean error of each distribution.

180 ms), even after being triggered by entering of the aiming beam into the specified targeting zone. The fastest operation is allowed under a setting of the 200- $\mu\text{m}$  threshold, while its average error is slightly greater than at lower thresholds. Even the largest error in the automated trials is still acceptable in laser photocoagulation, compared to the size of the laser spot (200–400  $\mu\text{m}$ ). The execution time is noticeably reduced by 20.3 s when the threshold is increased from 50 to 100  $\mu\text{m}$ ; the reduction is less than 5.0 s between the other higher thresholds. This is because error due to hand tremor becomes a prominent source of error when the threshold is as low as 50  $\mu\text{m}$ . To satisfy such a small threshold, the control system is prone to resetting the laser trigger and then repeating it, which increases execution time.

The average error in the manual trials rises rapidly from  $102 \pm 67$  to  $174 \pm 98$   $\mu\text{m}$  according to the increment of repetition rates used (shown as the red line in Fig. 7.5), compared to the error increment in the automated trials. As we found no statistically significant difference between the subjects in the automated trials, the same holds also for the manual trials ( $p$  ranges from 0.16 to 0.41), except at 1.0 Hz ( $p = 0.003$ ). Compared to the distribution of errors obtained in automated trials, the errors in manual operation are more widely spread over the error range of interest, as seen on the right side in Fig. 7.6.

Erroneous outcomes (untreated and misaimed burns) become pronounced in the manual trials as the firing rate increases, whereas such erroneous burns are not found in any of the automated trials, as shown in Fig. 7.7. Hence, the manual operation is marginally

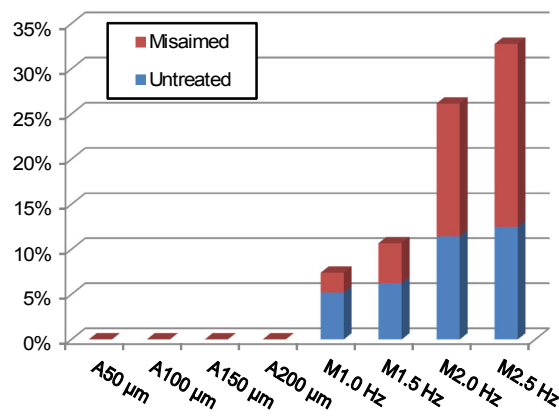


Fig. 7.7. Proportion of erroneous outcomes over the entire targets. The blue bar indicates the percentage of untreated targets due to lack of energy delivered to targets. The red bar stacked over the blue bar shows the percentage of misaimed burns, either yielding extraordinary error or aggregating around a single target.

TABLE 7.1. SUMMARY OF EXPERIMENTAL RESULTS

Trial	Control Setting	Execution Time (s)	Frequency (Target/s)	Error ( $\mu\text{m}$ )	Untreated Rate	Misaimed Rate	<i>p</i> -value between subjects
Automated	50 $\mu\text{m}$	46.55	0.69	$45 \pm 27$	0.0%	0.0%	0.643
	100 $\mu\text{m}$	26.25	1.22	$50 \pm 28$	0.0%	0.0%	0.162
	150 $\mu\text{m}$	21.75	1.47	$57 \pm 36$	0.0%	0.0%	0.169
	200 $\mu\text{m}$	18.72	1.74	$60 \pm 37$	0.0%	0.0%	0.101
Manual	1.0 Hz	32.01	1.00	$102 \pm 67$	5.2%	2.1%	0.003
	1.5 Hz	21.35	1.50	$124 \pm 71$	6.3%	4.7%	0.300
	2.0 Hz	16.26	1.97	$152 \pm 92$	11.5%	15.0%	0.411
	2.5 Hz	13.20	2.42	$174 \pm 98$	12.5%	20.1%	0.164

accomplished at the higher repetition rates due to lack of time to precisely maneuver the laser probe and also to adjust the height of the tool from the retinal surface. As a result, for example, in the manual trials at a firing rate of 2.5 Hz, erroneous burns represent 30% of the entire pattern. The analysis details for automated and manual trials are summarized in Table 7.2.

Given the interpolated data at the equivalent frequency settings, the average error in the automated trials is reduced by 53.0–56.4% compared to the manual trials, resulting in statistically significant differences for all equivalent frequencies (*p* ranges from  $10^{-20}$  to  $10^{-24}$ ). The interpolated data and analysis results are described in Table 7.1.

Finally, the result of the avoidance feature is demonstrated in Fig. 7.8, where white circles mark the targeted locations to be burned and black circles mark the target locations to be avoided. The 200- $\mu\text{m}$  threshold set for the demonstration caused half of the initial targets to be bypassed.

TABLE 7.2. COMPARISON OF AUTOMATED AND MANUAL TRIALS WITH THE INTERPOLATED DATA AT EQUIVALENT FREQUENCIES.

Frequency (Target/s)	Automated Error ( $\mu\text{m}$ )	Manual Error ( $\mu\text{m}$ )	Error Reduction (%)	<i>p</i> -value
1.00 Hz	$48 \pm 28$	$102 \pm 67$	53.0	$3.29 \times 10^{-20}$
1.25 Hz	$51 \pm 29$	$113 \pm 69$	55.0	$1.16 \times 10^{-23}$
1.50 Hz	$58 \pm 36$	$124 \pm 71$	53.6	$4.13 \times 10^{-24}$
1.75 Hz	$61 \pm 37$	$139 \pm 83$	56.4	$9.17 \times 10^{-25}$

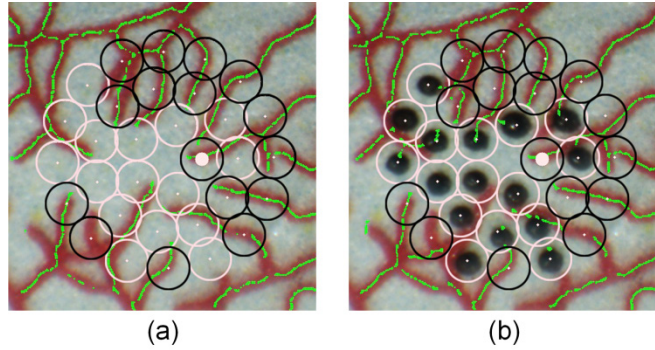


Fig. 7.8. Automated avoidance of blood vessels in automated laser photocoagulation. (a) Target placement before the photocoagulation. Empty black circles show avoided targets within 200  $\mu\text{m}$  of a vessel. The green lines represent blood vessels automatically identified by the eyeSLAM algorithm. (b) After completion of the automated laser photocoagulation.

## 7.4 Comparative Evaluation

We investigated the performance of robot-aided intraocular laser surgery for both “automated” and “semiautomated” operations under a board-approved protocol. Performance was evaluated in terms of accuracy and speed of operation, compared to unaided operation (with Micron turned off). The aided operation was controlled by setting a targeting threshold or a fixed repetition rate. We conducted the experiments under two test conditions: unconstrained (or “open-sky”) and constrained (eye phantom) environments. The open-sky test focuses primarily on the control performance of the robot-aided operation itself, while eliminating effects caused by the retinal tracking algorithm. On the other hand, the eye phantom provides much similar environment to realistic intraocular surgery. However, the overall performance may be affected by disturbance at the RCM, and the accuracy and robustness of the retinal tracking algorithm. Moreover, in the unconstrained experiment, the operator is allowed to freely move the instrument (e.g., both translation and rotation). On the other hand, in the constrained experiment, rotation (pivoting around the RCM) and axial motions are rather desirable, since transverse motion leads to the movement of the eye ball, resulting in the movement of the targets.

### 7.4.1 Experimental Setup

The experimental setup is similar to the prior setup used for the evaluation of the hybrid visual servoing. We introduced the same triple ring patterns, and the targets were preoperatively placed on along the circumferences of multiple circles with 600- $\mu\text{m}$  spacing: 1, 2, and 3 mm in diameter. As an indication of the targets, 200- $\mu\text{m}$  green dots were printed on a paper slide, which were used for targeting cues in unaided trials. In addition, four fiducials were introduced to align the preoperative targets with the printed green dots before the procedure. The fiducials were also postoperatively used to provide the ground truth for error analysis, taking into account error resulting from both the servo control and the retinal tracking. To burn targets on the paper slide, the power of the laser was set as 3.0 W with a duration of 20 ms, which yields distinct black burns on the paper. To evaluate the accuracy of operation for each trial, the resulting image was binarized to find black dots and then underwent  $K$ -means clustering to find the center of each burn. Error between the burn and the target locations was measured.

### 7.4.2 Open-Sky

A slip of paper was fixed on a flat surface under the operating microscope. In automated trials, five targeting thresholds were set in a range of 30–200  $\mu\text{m}$ , in order to characterize the resulting error and speed of operation, depending on the thresholds. The same setting was also adopted in semiautomated trials. For unaided operation, repetition rates were set to be 0.5–2.5 Hz with a step increment of 0.5 Hz, as acceptable results were attainable only with the rate below 2.5 Hz. We also repeated these tests for four trials and averaged errors, resulting in a total of 128 burns.

The mean error in automated operation slightly increases as the targeting threshold increases, whereas the execution time drops significantly from 29.4 to 14.3 s with higher thresholds. Similar trends are also found in the automated trials with fixed repeat rates. However, the mean error in semiautomated operation exponentially increases as the execution time decreases, as shown in Fig. 7.9. Interestingly, the semiautomated operation could not be performed at a 2.5 Hz repetition rate, while the unaided operation could marginally be done. This is because the operator instantaneously loses the hand-eye coordination, while the tip is being deflected to correct the aiming beam error, which requires extra time to accommodate the transition for switching the control back to the manual operation.

Representative results for the 1.0 Hz repetition rate are presented in Fig. 7.10 (a)–(c).

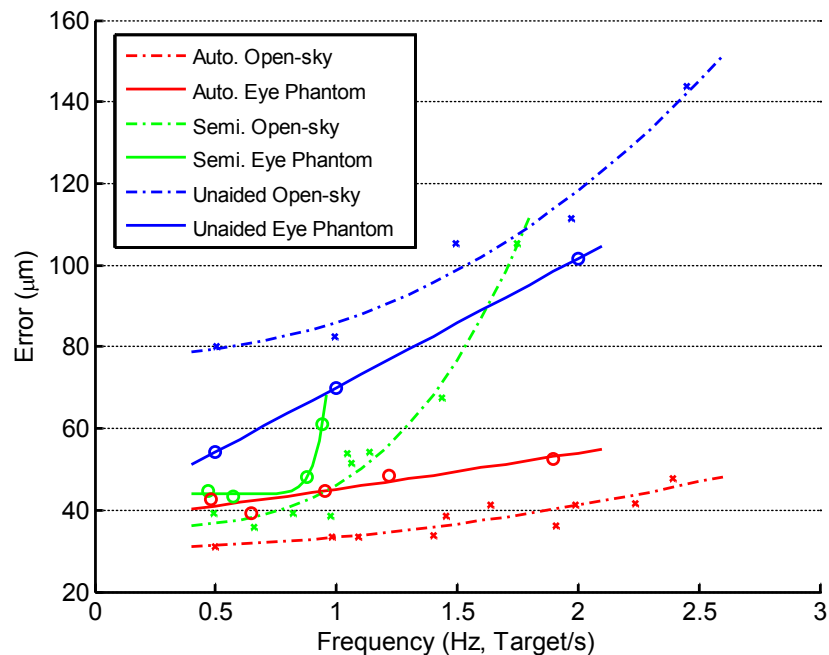


Fig. 7.9. Targeting error vs. effective frequency in both open-sky and eye phantom tasks.

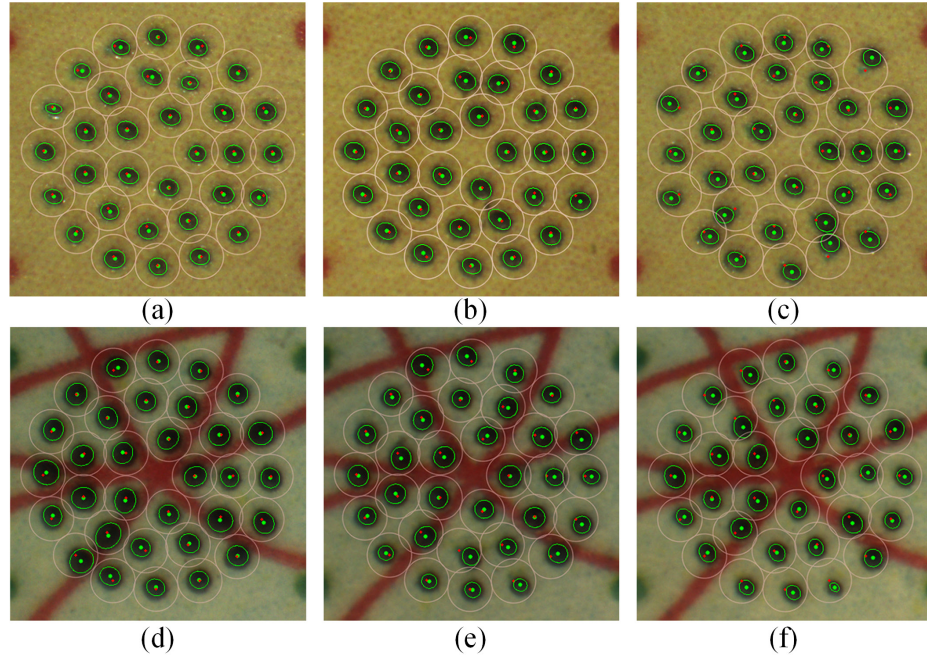


Fig. 7.10. Representative figures for a 1.0 Hz repetition rate in the open-sky and the eye phantom tasks. The top row shows the results from the open-sky task: (a) automated, (b) semiautomated, and (c) unaided trials. The bottom row shows the results from the eye phantom task: (d) automated, (e) semiautomated, and (f) unaided trials.

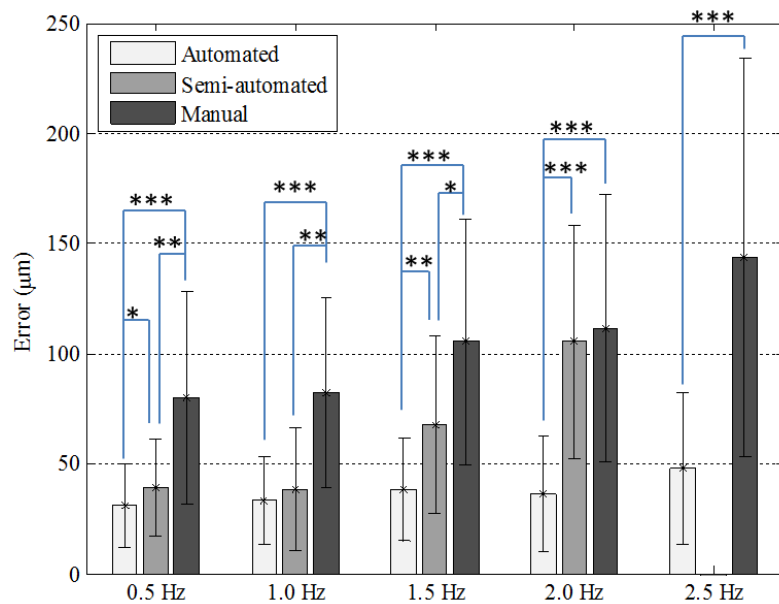


Fig. 7.11. Average error for various repetition rates in the open-sky task. Error bars indicates the standard deviation of the average error over 128 burns. Statistical significances from the ANOVA tests are presented as blue lines: \*\*\* $p < 1.0 \times 10^{-20}$ , \*\* $p < 1.0 \times 10^{-10}$ , and \*\* $p < 1.0 \times 10^{-2}$ .

TABLE 7.3. SUMMARY OF EXPERIMENTAL RESULTS IN OPEN-SKY TASK

Control Type	Execution Time (s) (Auto/Semi or All)	Automated ( $\mu\text{m}$ )	Semi-automated ( $\mu\text{m}$ )	Manual ( $\mu\text{m}$ )	Error Reduction (%)		
					Auto/Semi	Auto/Media	Semi/Media
30 $\mu\text{m}$	29.4/48.6	33	36	-	6.7	-	-
50 $\mu\text{m}$	22.8/39.1	34	39	-	13.9	-	-
100 $\mu\text{m}$	19.5/30.7	41	54	-	23.0	-	-
150 $\mu\text{m}$	16.1/30.1	41	52	-	19.7	-	-
200 $\mu\text{m}$	14.3/28.2	42	54	-	23.1	-	-
0.5 Hz	64.0	31	39	80	21.1*	61.4***	51.0**
1.0 Hz	32.0	33	39	82	13.2	59.3***	53.1**
1.5 Hz	21.3	39	68	105	42.9**	63.4***	35.9*
2.0 Hz	16.0	36	105	111	65.6***	67.4***	5.4
2.5 Hz	12.8	48	-	142	-	66.2***	-

“Auto” and “Semi” stand for automated and semiautomated, respectively.

Statistical significances from the ANOVA tests: \*\*\*  $p < 1.0 \times 10^{-20}$ , \*\*  $p < 1.0 \times 10^{-10}$ , and \*  $p < 1.0 \times 10^{-2}$ .

The overall results are summarized in Table 7.3, including statistical analysis for three possible combinations via the ANOVA tests: automated/semautomated, automated/unaided, and semiautomated/unaided. Statistically significant differences between the automated and the unaided trials are found across all repetition rates ( $p < 1.0 \times 10^{-20}$ ).

### 7.4.3 Eye Phantom

In the eye phantom task, we selectively adopted a few control settings from the open-sky task, considering the effectiveness of operation in terms of accuracy and execution time. As a result, the targeting thresholds were set to 50 and 100  $\mu\text{m}$  for automated and semiautomated trials. The repetition rate was varied up to 2.0 Hz, at which the unaided operation could marginally be performed in the eye phantom, since maneuverability of the tool was limited by the fulcrum at the scleral entry.

The interruption of hand-eye coordination became pronounced, specifically, in semiautomated operation, as the operation speed increased, due to limited dexterity in the eye phantom. As a result, semiautomated trials were possible only up to 1.0 Hz. Noticeably, the mean error is increased in both automated and semiautomated trials, compared to the

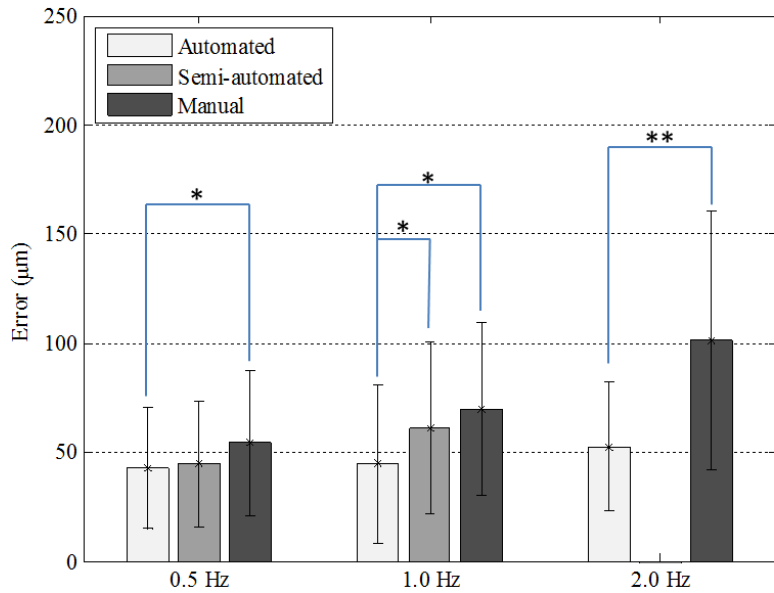


Fig. 7.12. Average error for various repetition rates in the eye phantom task. Error bars indicates the standard deviation of the average error over 128 burns. Statistical significances from the ANOVA tests are presented as blue lines:  $**p < 1.0 \times 10^{-10}$  and  $***p < 1.0 \times 10^{-2}$ .

results obtained in the open-sky tests, whereas the errors in the unaided operation are lower. It is considered that the fulcrum supports the laser probe during the unaided operation, resulting in stabilization of the tool. On the other hand, the fulcrum degrades control performance in the aided operation by applying external force to the tool, creating a disturbance to the control system. Due to these effects, the semiautomated trials do not show any statistically significant difference from the unaided trials. On the other hand, high accuracy is still achieved in the automated trials, all of which were significantly better than unaided performance.

Representative results for the 1.0 Hz repetition rate in the eye phantom are shown in Fig. 7.10(d)–(f), and the overall results are summarized in Table 7.4

TABLE 7.4. SUMMARY OF EXPERIMENTAL RESULTS IN EYE PHANTOM TASK

Control Type	Execution Time (s) (Auto/Semi or All)	Automated (μm)	Semi-automated (μm)	Manual (μm)	Error Reduction (%)		
					Auto/Semi	Auto/Manual	Semi/Manual
50 μm	49.6/55.8	39	43	-	8.9	-	-
100 μm	26.2/36.3	48	48	-	0.0	-	-
0.5 Hz	64.0	43	45	54	4.2	21.1*	17.7
1.0 Hz	32.0	45	61	70	27.0*	36.3*	12.7
2.0 Hz	16.0	53	-	102	-	48.2**	-

“Auto” and “Semi” stand for automated and semiautomated, respectively.

Statistical significances from the ANOVA tests: \*\*\*  $p < 1.0 \times 10^{-20}$ , \*\*  $p < 1.0 \times 10^{-10}$ , and \*  $p < 1.0 \times 10^{-2}$ .

## 7.5 Summary

The improved system presented in this study demonstrates robot-aided laser photocoagulation for intraocular surgery using hybrid visual servoing. The proposed hybrid control scheme is well suited to robot-aided intraocular laser surgery, as it deals well with inaccuracy in 3D reconstruction. The image Jacobian update also improves the control performance by allowing the increment of gains used for visual servoing. Consequently, the automated system greatly improves the accuracy of laser photocoagulation, compared to conventional manual operation, showing statistically significant differences in average error. It is also found that the hybrid control approach improves the accuracy of robot-aided operation, compared to the position-based visual servo control [146]; the average error is reduced by 26.2%.

In addition, the graphical overlay system allows the surgeon to operate the system in a user-friendly fashion while directly viewing through the operating microscope. The visual cues designed to maintain hand-eye coordination were useful in robot-aided operation, allowing repeatable experiments in both in the open-sky and eye phantom tasks, alleviating the limitations of previous work [146]. Automated avoidance of critical anatomy was also demonstrated by localizing and tracking of blood vessels; this can reduce the cognitive load of the surgeon when operating near critical structures such as the fovea.

In the comparative evaluation, the fixed-repeat-rate control in aided operation allowed direct comparison to unaided operation at equal firing rates. Hence, it is found that the automated operation still shows significantly lower errors, compared to the unaided operation, although the performance is slightly degraded by constraints in the eye phantom. Compared to semiautomated laser surgery using the 3-DOF Micron [26], the performance was significantly improved in terms of the mean error: from 129 to 39  $\mu\text{m}$  at the 1.0 Hz repeat rate. As a result, the error is reduced by 53.1%, whereas the error reduction with the 3-DOF Micron was only 22.3%.

The comparative study presented in this paper could be a general guideline for development of robot-aided intraocular surgery using handheld instruments. For example, the investigation of the semiautomated operation under both constrained and unconstrained environments would be meaningful for design of a human-in-the-loop system. Transition between unaided and aided operations should be considered for further study.



## **8 ROBOT-AIDED INTRAOCULAR LASER SURGERY USING MONOCULAR VISION**

The ultimate goal of this thesis is to extend the benefit of the handheld micromanipulator to automated microsurgery in conjunction with image-guidance. In particular, we aim to accomplish automated intraocular laser surgery in an intact eye. To achieve this goal, we need to address problems in visual servoing in the eye, such as unreliable detection of image features due to illumination changes and optical distortion by the complex eye and imaging system. We therefore propose hybrid visual servoing of the handheld micromanipulator using a monocular camera, which involves retinal surface estimation based on structured light and partitioned visual servoing with image Jacobian updates.

## 8.1 Related Work

In earlier work, we have shown that the new handheld micromanipulator can perform automated tasks such as intraocular OCT probe scanning or laser photocoagulation with an enlarged workspace [115], [146]. Specifically, automated laser photocoagulation systems presented so far necessitate the registration of camera coordinates with the global coordinates (referred as the ASAP coordinates), in order to maneuver a laser probe on the retinal surface. As described earlier, we have adopted a conventional camera calibration technique (DLT: the Direct Linear Transformation) for the registration, and then reconstructed the retinal surface by the triangulation of feature points on the surface using stereo cameras [146]. However, it would not be suitable to apply the same technique in an intact eye, since camera calibration and resulting surface reconstruction are prone to failure in such a complex eye due to considerable optical distortion and unreliable vision detection. Most calibration methods primarily assume a classical perspective camera model in a single medium such as air, but the assumption would not hold for a complex eye model entailing the refraction of the light [158]; the eye is filled with vitreous humor (replaced with saline or silicon oil during operation to maintain constant intraocular pressure) and is also covered with a cornea and contact lens (or BIOM lens: Binocular Indirect Ophthalmomicroscope) to provide a wide-angle view during operation.

This difficulty in intraocular surgery has led to the development of new 3D localization methods for controlling a microrobot inside the eye, taking the unique optical characteristics into account [158], [159]. Bergeles *et al.*, introduced a focus-based method accounting for the optics of the human eye in the imaging and localization of the microrobot with a single stationary camera [158]. They adopted an optical model called the Navarro schematic eye, based on biometric data. The study showed the feasibility of the technique on a variety of ophthalmic microscopes even with uncertainties of optical parameters used in modeling. However, the localization error is limited to a few hundred micrometers, and drift compensation and servoing of the microrobot were not demonstrated due to the real-time problem [159]. Visual servoing of the microrobot was recently demonstrated in a phantom eye model, under a setup close to ophthalmic microscopy [159]. A new intraocular projection model (*Raxel*-based projection model) was introduced to accurately localize the microrobot in real time. However, the servoing error still stays at the level of a few hundred micrometers, which is substantially large in microsurgery. In addition, it is complicated to model the eye with a large set of optical parameters, each of which brings its own uncertainty.

In contrast to the microrobot relying on vision feedback for localization, Micron always provides the tool tip pose with respect to the ASAP coordinates. Consequently, we do not require localizing the tool tip, but do still need to register the imaging system in the ASAP coordinates to utilize vision feedback for control. This unique feature of the Micron system allows us to avoid complex modeling of the imaging system in intraocular surgery, since we can partition degrees of freedom in controlling the tool tip as demonstrated by hybrid visual servoing in Chapter 7; the 3-DOF tip control can be decomposed into 2-DOF transverse control parallel to the retinal surface and 1-DOF control along the axis of the tool. If the retinal surface can be approximated in the ASAP coordinates, we can use a monocular camera for control, instead of using a stereomicroscope and considering the complex optical system to reconstruct the surface in 3D space.

Therefore, we propose a new method to estimate the retinal surface with a monocular camera, utilizing the scanning capability of the 6-DOF Micron. The estimation can be realized by introducing a structured light approach and analyzing the projective geometry of aiming beam trajectories on images. Moreover, we update an image Jacobian used for the aiming beam control because the estimated Jacobian potentially includes error due to the approximation of the system and nonlinearity. Consequently, the proposed method does not rely on the complicated calibration of the entire system.

The proposed approach includes four steps as follows:

- Estimate the retinal surface in the 3D ASAP coordinates, by scanning an aiming beam;
- Find an image Jacobian from the surface estimation, which is initially assumed to be parallel to the image plane;
- Apply the hybrid visual servoing for the 3-DOF tool tip control;
- Update the initial Jacobian, given error measured while servoing the tool.

Since the hybrid visual servoing and an adaptive framework have been already validated in the previous chapter, we focus primarily on the monocular surface estimation in this chapter.

## 8.2 Retinal Surface Estimation using Monocular Vision

We propose a new method to estimate the retinal surface with a monocular camera, by introducing predefined beam scanning on the surface. To find the surface in the ASAP coordinate with a single camera, we use the projective geometry of a beam trajectory created by scanning a laser probe, because the aiming beam is highly detectable in the eye, regardless of illumination change. The retinal surface is assumed to be parallel or near parallel to an image plane. As depth of field in microscopic imaging is quite shallow, focused images can be obtained only when the surface is located within a very narrow region perpendicular to the optical axis of the microscope [160]. Hence, the projective geometry of the aiming beam is allowed by assuming the retinal surface to be locally planar in an area of interest.

Regardless of optical distortion, the ray of an aiming beam always intersects with the

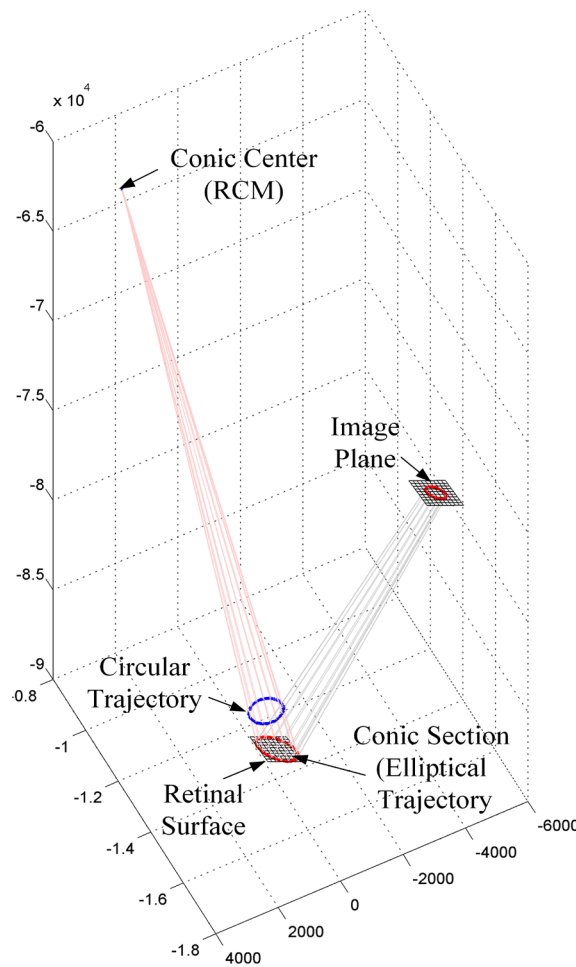


Fig. 8.1. Illustration of a conic section shown as an ellipse on the retinal surface.

surface. For example, the circular motion of the laser probe with an RCM results in a conic shape of the beam trajectory about the nominal axis of the tool. The trajectory is shown as an ellipse on a plane, subject to a conic section cut by the retinal plane, which is assumed planar, as depicted in Fig. 8.1. It is then found that the shape of the ellipse, i.e., the aspect ratio, is related to the tilted angle of the plane that cuts the cone. Therefore, our goal is to find a plane regarded as the retinal surface, in terms of a plane normal and a point that lies on the plane, using the relationship of the projected ellipses.

A similar interpretation utilizing such a circle-ellipse relationship has been investigated in computer vision and tomography [161], [162]. Chen *et al.* introduced a camera calibration method using two coplanar circles, analyzing the shape of ellipses shown on a camera [161]. The relationship was also explored for the calibration of a cone-beam scanner used in both x-ray computed tomography and single-photon emission computed tomography [162]. Interestingly, it also uses circular traces subject to ellipses on the detector and the calibration geometry is determined analytically using the parametric description of these ellipses.

### 8.2.1 Projective Geometry Analysis

We use circular scanning of the laser probe to project an ellipse on the plane to be estimated. First, the laser probe is scanned to generate a circular pattern around a pivot point, which could be regarded as an RCM in vitreoretinal surgery. The ray from the laser probe results in a cone beam in 3D space as shown in Fig. 8.1. Once the resulting trajectory is detected in a sequence of images, it is fitted as an ellipse. The fitted ellipse is then parameterized by following descriptions:

- $c_e$  : The center of the ellipse;
- $m_a$  : The half length of the major axis;
- $m_b$  : The half length of the minor axis;
- $\theta_e$  : The inclination angle from the  $x$ -axis of the image plane.

The ellipse is regarded as the conic section cut by the tilted plane to be estimated. Thus, the plane can be described by the rotation of the plane initially perpendicular the axis of the cone. It is found that the axis of the rotation to form the ellipse can be any vector orthogonal to the axis of the cone. Fig. 8.2 shows the tilted plane and corresponding ellipse on the conic section, given rotation about the  $y$ -axis of the cone. We then define the angle

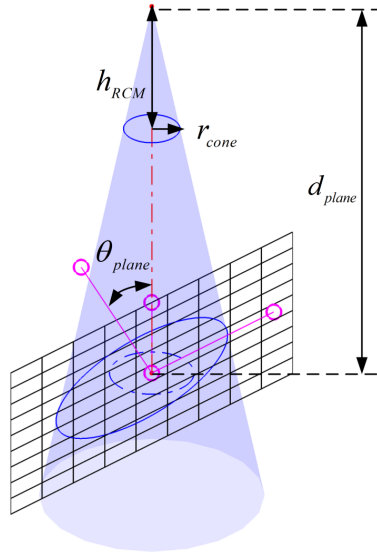


Fig. 8.2. Cone beam analysis and corresponding parameters to describe a target plane.

of rotation  $\theta_{plane}$ , using the aspect ratio of the ellipse and the opening angle of the cone as in (8.1).

$$\theta_{plane} = \pm \arcsin\left(\sqrt{\frac{1 - \frac{1}{(\gamma)^2}}{1 + \frac{1}{\tan^2 \theta_{cone}}}}\right), \quad (8.1)$$

where the aspect ratio  $\gamma$  and the opening angle  $\theta_{cone}$  are defined in (8.2) and (8.3), respectively.

$$\gamma = \frac{m_b}{m_a} \quad (8.2)$$

$$\tan \theta_{cone} = \frac{h_{RCM}}{r_{cone}} \quad (8.3)$$

Given the angle of rotation  $\theta_{plane}$ , we can estimate a point belonging to the plane as an offset  $d_{plane}$  from a vertex  $P_{RCM}$  along the axis of the cone. If the scale factor of the image,  $s_{cam}$ , is known, the point on the plane can be described as  $P_{plane}$  in the ASAP coordinates, using (8.4) and (8.5).

$$d_{\text{plane}} = \frac{\cos \theta_{\text{plane}} (\tan^2 \theta_{\text{cone}} - \tan^2 \theta_{\text{plane}})}{\tan \theta_{\text{cone}}} m_a s_{\text{cam}} \quad (8.4)$$

$$\mathbf{P}_{\text{plane}} = \mathbf{P}_{\text{RCM}} - d_{\text{plane}} \mathbf{v}_{\text{cone}}, \quad (8.5)$$

where  $\mathbf{v}_{\text{cone}}$  is a unit vector representing the axis of the cone.

From the derivation, it is noted that the angle  $\theta_{\text{plane}}$  related to the plane normal is scale-free to the images, whereas the point on the plane needs the image scale because of the value  $s_{\text{cam}}$ . Such an image scale can also be specified according to the zoom factor of an operating microscope.

However, the angle  $\theta_{\text{plane}}$  itself does not uniquely describe the tilted plane, since any arbitrary vector orthogonal to the axis of the cone can be taken as the axis of rotation. Thus, the plane normal can also be any vector, taking such the tilting angle from the axis of the cone as illustrated in Fig. 8.3; the identical ellipse would be formed, given any rotation of a true normal vector about the axis of the cone. Accordingly, we need at least two circle scans to uniquely define the surface normal: finding a common vector from two infinite sets of normal vectors, called herein *dual cone beam reconstruction*. This approach relies only on the shapes of the two ellipses.

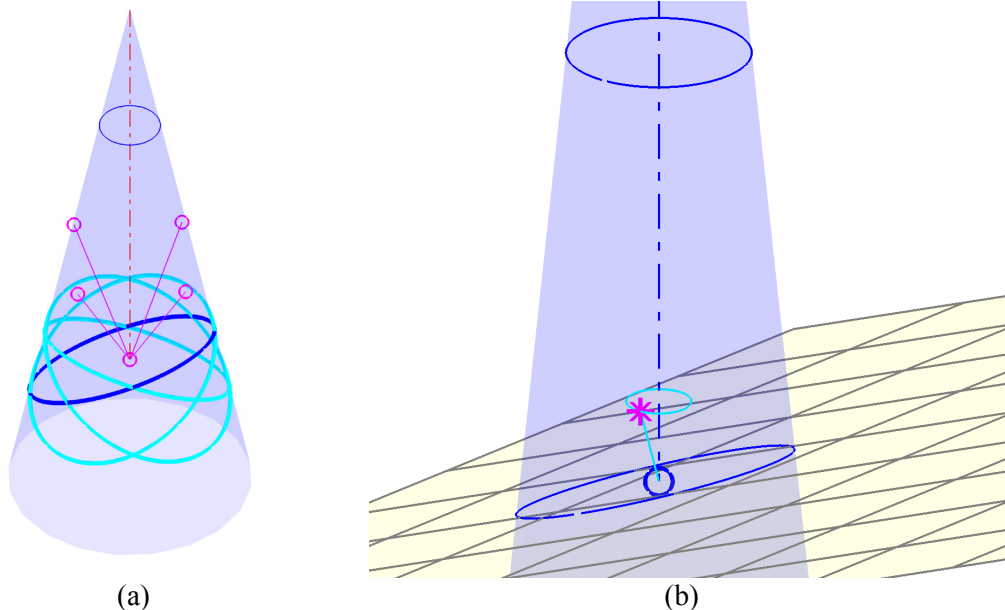


Fig. 8.3. An infinite set of surface normal vectors existing along the axis of the cone. (a) The identical shapes of ellipses according to different axes of rotation. (b) The infinite set of normal vectors is represented as a 3D circle (the cyan color) in the ASAP coordinates.

## 8.2.2 Dual Cone Beam Reconstruction

### 8.2.2.1 Surface Normal Estimation

We introduce dual cone beam reconstruction in order to uniquely define the surface normal. Given the two circle scans at the tool tip, we obtain two projected ellipses on the image plane as shown in Fig. 8.4. The resulting ellipses are then described by two sets of the angle and the point that describe the surface using (8.1) and (8.5).

$$\theta_{\text{plane}}^i \text{ and } \mathbf{P}_{\text{plane}}^i, \text{ where } i \in \{1, 2\}. \quad (8.6)$$

Here, the absolute value of the angle is taken at this moment for further steps; the sign of the angle will be determined later. First, we set coordinate transformation  $\mathbf{R}_{C_i}^{\text{ASAP}}$  for the  $i$ th cone that describes the coordinates of the cone with respect to the ASAP coordinates:

$$\mathbf{R}_{C_i}^{\text{ASAP}} = \begin{bmatrix} \mathbf{v}_x^i & \mathbf{v}_y^i & \mathbf{v}_z^i \end{bmatrix}, \quad (8.7)$$

where  $\mathbf{v}_z^i$  is aligned with the axis of the  $i$ th cone, and is also identical to  $\mathbf{v}_{\text{cone}}$  in (8.5). The tilted plane is then regarded as the rotation of the  $xy$ -plane defined in the coordinates of the  $i$ th cone,  $C_i$ . Hence, we initially define the normal vector of the plane as the rotation of the vector  $\mathbf{v}_z^i$  about the  $y$ -axis  $\mathbf{v}_y^i$  by the angle  $\theta_{\text{plane}}^i$ :

$$\mathbf{n}_{\text{init}}^i = \mathbf{R}(\widehat{\mathbf{v}_y^i}, \theta_{\text{plane}}^i) \mathbf{v}_z^i. \quad (8.8)$$

As these normal vectors are not unique, the infinite sets of the normal vectors are interpreted as two 3D circles in a unit sphere as depicted in Fig. 8.5. Therefore, the true

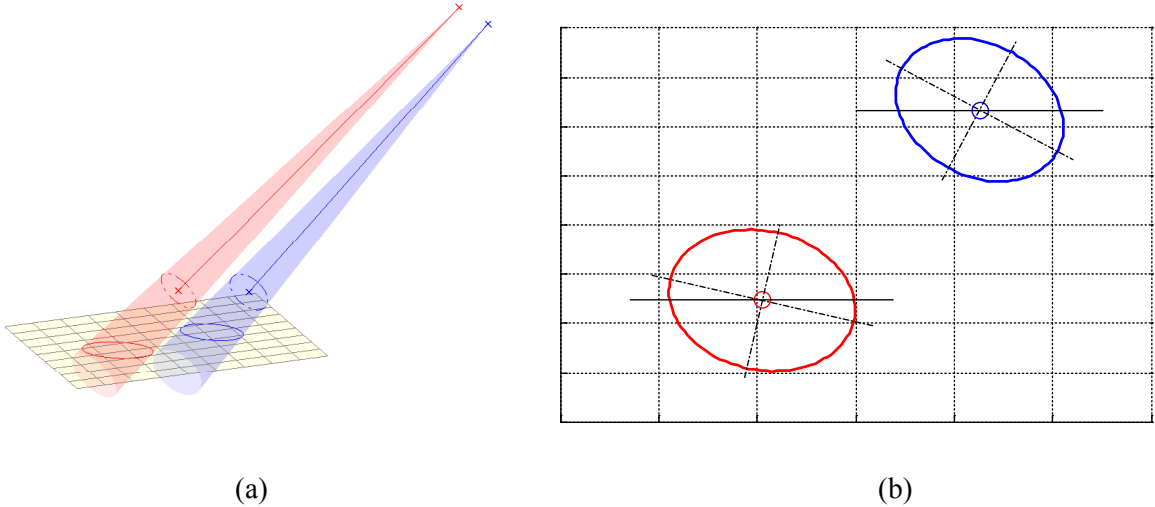


Fig. 8.4. (a) Conic sections forming two ellipses on the retinal surface by circular scanning of the laser probe about the axis of the tool. (b) Resulting ellipses shown in the image plane.

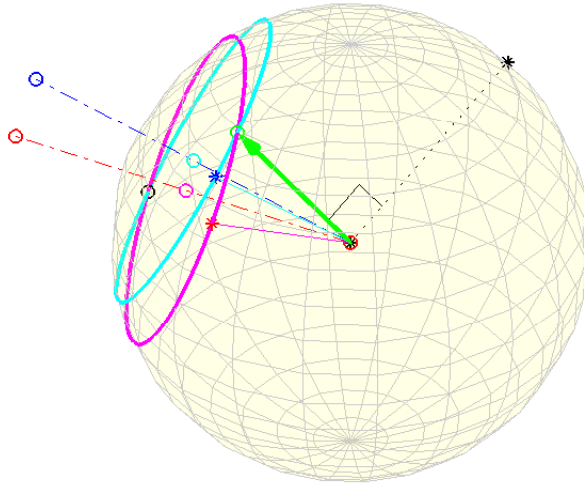


Fig. 8.5. Illustration of the infinite sets of two initial normal vectors in the unit sphere. The true surface normal is indicated as the green arrow.

normal vector must be located at the intersection of the two circles in the sphere. A degenerate case occurs when the axes of the two cones are parallel to each other; an infinite number of solutions then exist for the normal.

To analytically find the intersection of the two circles, we introduce a supplementary plane that describes each circular trajectory in 3D. Each supplementary plane is then defined by a plane normal  $\mathbf{v}_z^i$  and a point  $\mathbf{n}_{init}^i$  in the unit sphere. Consequently, the intersection of the resulting planes is attained as a common line in 3D, which is subject to passing through the intersection of the two circles. The common line  $l(s)$  is described by a unit vector  $\mathbf{u}$  and a point  $\mathbf{p}_0$ :

$$l(s) = \mathbf{p}_0 + s\mathbf{u}, \quad (8.9)$$

where  $\mathbf{u}$  is orthogonal to the two vectors,  $\mathbf{v}_z^1$  and  $\mathbf{v}_z^2$ , and  $\mathbf{p}_0$  is one of points that lies along the line as in (8.10).

$$\mathbf{u} = \frac{\mathbf{v}_z^1 \times \mathbf{v}_z^2}{\|\mathbf{v}_z^1 \times \mathbf{v}_z^2\|} \quad \text{and} \quad \mathbf{p}_0 = [(\mathbf{n}_{init}^1 \cdot \mathbf{v}_z^1)\mathbf{v}_z^2 - (\mathbf{n}_{init}^2 \cdot \mathbf{v}_z^2)\mathbf{v}_z^1] \times \mathbf{u} \quad (8.10)$$

Since the common line also passes through the unit sphere, we calculate the intersection between the line and the unit sphere, instead of directly calculating the intersection of the two 3D circles:

$$\|\mathbf{p}_0 + s\mathbf{u}\| = 1. \quad (8.11)$$

As a result, the solution subject to the surface normal is analytically derived in the Cartesian coordinates, as in (8.12).

$$\mathbf{n}_{plane} = \mathbf{p}_0 + \left[ -\mathbf{p}_0^T \mathbf{u} \pm \sqrt{(\mathbf{p}_0^T \mathbf{u})^2 - (\mathbf{p}_0^T \mathbf{p} - 1)} \right] \mathbf{u} \quad (8.12)$$

Finally, we obtain one or two possible normal vectors  $\mathbf{n}_{plane}$  for the estimated plane, depending on the number of intersections. If two normal vectors are found, one is identified as the true normal. The cross product of  $\mathbf{n}_{plane}$  with a unit vector  $\mathbf{v}$  is subject to zero or nearly zero, where the vector  $\mathbf{v}$  is defined by the two points on the plane as in (8.13).

$$\mathbf{n}_{plane} \cdot \mathbf{v} \approx 0, \text{ where } \mathbf{v} = \frac{\mathbf{P}_{plane}^1 - \mathbf{P}_{plane}^2}{\|\mathbf{P}_{plane}^1 - \mathbf{P}_{plane}^2\|}. \quad (8.13)$$

### 8.2.2.2 Coordinate Mapping

Given the true normal, the final step is to find the principal vectors,  $\mathbf{u}_{plane}$  and  $\mathbf{v}_{plane}$ , of the plane, which are aligned with the image coordinates.

First, the tilt angle  $\theta_{plane}^i$  is now redefined with the signed angle as in (8.14).

$$\theta_{plane}^i = \text{sign}(\mathbf{n}_{plane} \cdot \mathbf{v}_x^i) |\theta_{plane}^i| \quad (8.14)$$

We can then specify the coordinates of the plane  ${}^0\mathbf{R}_{plane}^{ASAP}$  by rotating the coordinates of the cone beam,  $\mathbf{R}_C^{ASAP}$  as in (8.15).

$${}^0\mathbf{R}_{plane}^{ASAP} = \mathbf{R}(\hat{\mathbf{v}}_y, \theta_{plane}) \mathbf{R}_C^{ASAP} = [\mathbf{u} \quad \mathbf{v} \quad \mathbf{n}]_{plane}, \quad (8.15)$$

where the axis and angle of rotation are defined by the  $y$ -axis of the cone beam coordinates  $\mathbf{v}_y$  and the angle  $\theta_{plane}$ , respectively.

Since we assumed the rotation about the  $y$ -axis of the cone beam coordinates, the initial step for the coordinate mapping is to align the minor axis of the ellipse with the  $y$ -axis of the cone beam coordinates as shown in Fig. 8.2. For this step, we regard the normal vector  $\mathbf{n}_{plane}$  as a rotation of the initial vector  $\mathbf{n}_{init}$  about the axis of the cone  $\mathbf{v}_z$ , by taking into account the rotation of transverse vectors,  $\mathbf{t}_{init}^{ASAP}$  and  $\mathbf{t}_{plane}^{ASAP}$ . The transverse vectors are defined with respect to the ASAP coordinates as below:

$$\mathbf{t}_{init}^{ASAP} = \mathbf{n}_{init} - (\mathbf{n}_{init} \cdot \mathbf{v}_z) \mathbf{v}_z \text{ and } \mathbf{t}_{plane}^{ASAP} = \mathbf{n}_{plane} - (\mathbf{n}_{plane} \cdot \mathbf{v}_z) \mathbf{v}_z. \quad (8.16)$$

To calculate the angle of rotation  $\theta_t$ , the transverse vectors are transformed back to the cone beam coordinates by  $[\mathbf{R}_C^{ASAP}]^T$ .

$$\mathbf{t}_{init}^{C1} = [\mathbf{R}_C^{ASAP}]^T \mathbf{t}_{plane}^{ASAP} = \begin{bmatrix} \mathbf{\omega}_x^{init} & \mathbf{\omega}_y^{init} & 0 \end{bmatrix}^T \text{ and } \mathbf{t}_{plane}^{C1} = [\mathbf{R}_C^{ASAP}]^T \mathbf{t}_{plane}^{ASAP} = \begin{bmatrix} \mathbf{\omega}_x^{final} & \mathbf{\omega}_y^{final} & 0 \end{bmatrix}^T \quad (8.17)$$

By applying the angle of rotation  $\theta_t$  about the cone axis, we obtain a new coordinates  ${}^1\mathbf{R}_{plane}^{ASAP}$  of which the  $x$ -axis (the first column vector in  ${}^1\mathbf{R}_{plane}^{ASAP}$ ) is aligned with the major axis of the ellipse as shown in Fig. 8.6 with dotted lines:

$${}^1\mathbf{R}_{plane}^{ASAP} = \mathbf{R}(\hat{\mathbf{v}}_z, \theta_t) {}^0\mathbf{R}_{plane}^{ASAP}, \quad (8.18)$$

$$\theta_t = \text{atan}2(\mathbf{\omega}_y^{final}, \mathbf{\omega}_x^{final}) - \text{atan}2(\mathbf{\omega}_y^{init}, \mathbf{\omega}_x^{init}). \quad (8.19)$$

We then consider the inclination angle of the first ellipse  $\theta_e^1$ , in order to completely describe the principal vectors,  $\mathbf{u}_{plane}$  and  $\mathbf{v}_{plane}$ , aligned with the image coordinates. Given the homogenous coordinate transform  $\mathbf{T}_{ASAP}^{plane}$ , the plane point  $\mathbf{P}_{ASAP}^2$  on the second ellipse at the ASAP coordinates is transformed to the point  $\mathbf{P}_{plane}^2$  at the plane coordinates with respect

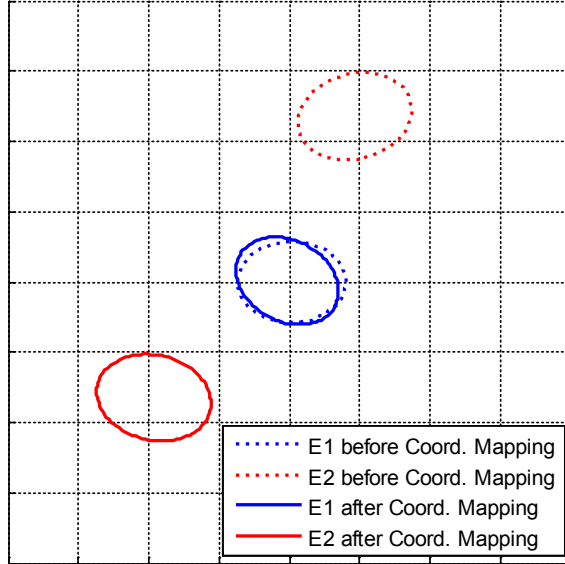


Fig. 8.6. The dotted lines indicate the ellipses when the major axis of the first ellipse (blue) is aligned with the  $x$ -axis. The solid lines represent the final trajectories after applying the coordinate mapping, which is subject to being identical to the trajectories in the camera view as shown in Fig. 8.4(b).

to the first cone beam:

$$\mathbf{P}_{\text{plane}}^2 \equiv \frac{1}{S_{\text{cam}}} \mathbf{T}_{\text{ASAP}}^{\text{plane}} \mathbf{P}_{\text{ASAP}}^2. \quad (8.20)$$

Consequently, we obtain a corresponding 2D point  $\mathbf{p}_{\text{plane}}^2$  by disregarding the  $z$ -component of the 3D point  $\mathbf{P}_{\text{plane}}^2$ ; the  $z$ -value is subject to zero on the plane. Because the inclination angle of an ellipse can be defined only within a range from  $-\pi/2$  to  $+\pi/2$ , the inclination angle may be ambiguous; the second ellipse (the red one in Fig. 8.6) could be located either above or below (' $\pi$ '-flipped) the first ellipse (the blue). To determine the configuration, we consider a vector described by two points,  $\mathbf{p}_{\text{plane}}^2$  and the center of the second ellipse  $\mathbf{c}_e^2$ . Since the point  $\mathbf{p}_{\text{plane}}^2$  is supposed to be located along the major axis of the second ellipse, the vector should be parallel to the major axis of the second ellipse, denoted by the vector  $\mathbf{v}_{e2}$ :

$$(\mathbf{P}_2^{\text{plane}} - \mathbf{c}_e^2) \cdot \mathbf{v}_{e2} \approx 0, \text{ then } \mathbf{R}_{\text{image}}^{\text{ASAP}} = \mathbf{R}(\hat{\mathbf{n}}_{\text{plane}}, -\theta_e^1)^T \mathbf{R}_{\text{plane}}^{\text{ASAP}}; \quad (8.21)$$

$$\text{Otherwise, } \mathbf{R}_{\text{image}}^{\text{ASAP}} = \mathbf{R}(\hat{\mathbf{n}}_{\text{plane}}, \pi - \theta_e^1)^T \mathbf{R}_{\text{plane}}^{\text{ASAP}}. \quad (8.22)$$

Finally, we obtain the plane coordinates  $\mathbf{R}_{\text{image}}^{\text{ASAP}}$ , in which the transverse components,  $\mathbf{u}_{\text{plane}}$

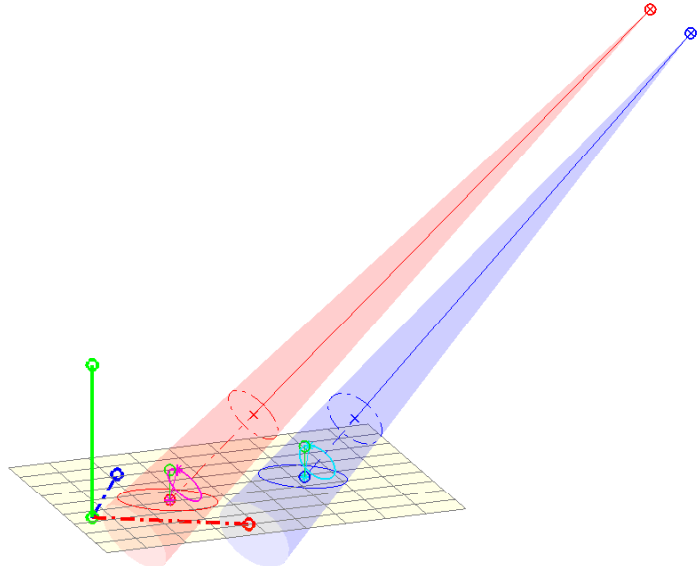


Fig. 8.7. Estimated surface via dual cone beam reconstruction. The green line indicates the surface normal, and the blue and red lines represent the other principal vectors of the plane aligned with the image coordinates.

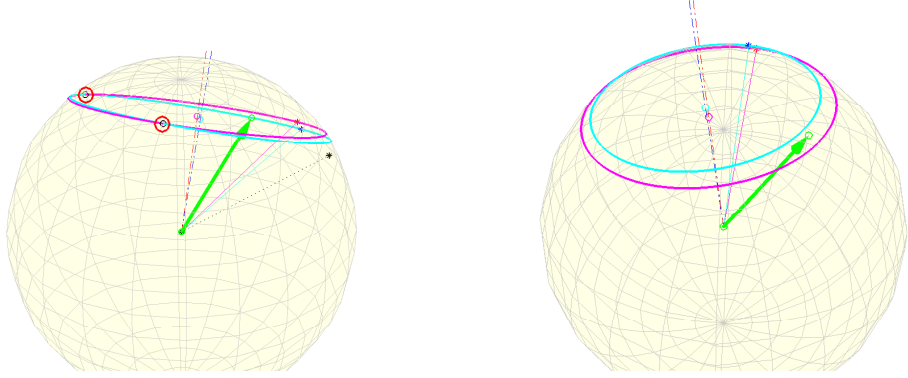


Fig. 8.8. Failure cases of dual cone beam reconstruction with real data. The green arrow indicates the true normal vector supposed to be estimated. The red circles indicate the estimated surface normal vectors.

and  $v_{plane}$  are aligned with the  $x$ - and  $y$ -axes in the camera coordinates as depicted in Fig. 8.7.

### 8.2.3 Single Cone Beam Reconstruction

We have formulated a surface reconstruction method using dual cone beam scans. However, given real data, the method may fail in finding the intersection of two circles that represent sets of infinite normal vectors in 3D, as the estimated angle of the tilted plane in (8.1) could also be imprecise; such that imprecise estimation would yield incorrect circles in 3D. This could thus lead to either an incorrect surface normal or no solution on the unit sphere as depicted in Fig. 8.8.

Therefore, we propose a new method using a single cone beam scan, taking into account point correspondences in a beam trajectory. As mentioned earlier, the surface normal would not uniquely be defined with a single ellipse itself, leading to an infinite set of normal vectors. We thus incorporate point correspondences between 3D tip and 2D beam positions, which are not considered in the dual cone beam reconstruction. For example, we assume that a data point is virtually projected on a plane from a ray resulting from the tip and RCM positions. We then utilize the fact that the relative angle of the data point with respect to the major axis of the virtual ellipse varies depending on which vector is chosen from the infinite set of normal vectors.

Fig. 8.9 depicts ellipse trajectories for visualizing each step of the single cone beam reconstruction. The first data point on each trajectory is marked as either a cross or a circle. The red solid line shows the beam trajectory acquired from images, and the cross marker indicates its first data point. The green dotted line is created by the initial estimation of the

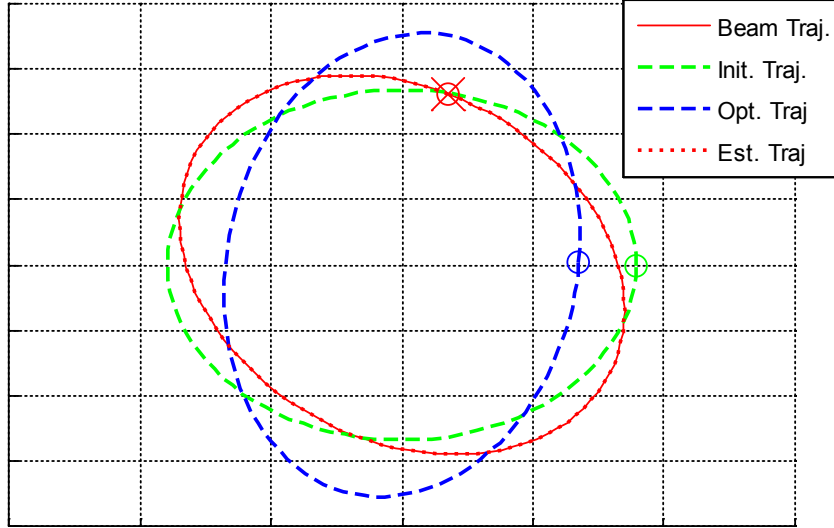


Fig. 8.9. Ellipse trajectories for demonstration of the single cone beam reconstruction. The first data point on each trajectory is marked as either cross or circle. The solid red line represents the beam trajectory acquired in the image plane. The green dotted line is for the projected ellipse from the initial estimation of the surface. The blue dotted line indicates the trajectory undergone the optimization for machining the relative angles of data points. The red dotted line is finally obtained after the transverse vectors of the estimated plane are aligned with the image coordinates.

surface, assuming rotation of the  $xy$ -plane about the  $y$ -axis of the cone, where the green circle marker is corresponding to the first data point. Hence, it is noted that the relative angle of the green circle marker with respect to the major axis is different from the angle of the first data point on the red trajectory. If we could find a specific axis of rotation instead of the  $y$ -axis of the cone, the blue trajectory would be attained, in which the relative angles of data points are matched with the actual angles from the beam trajectory. For instance, the relative angle of the first point becomes identical to the angle in the red beam trajectory, as shown by the blue circle in Fig. 8.9. Finally, the transverse coordinates of the plane are matched with the image coordinates as shown by the red dotted line, with the red circle marker indicating the first data point.

Hence, our goal is to find the best normal vector that aligns the angles of projected data points with the angles of actual data points in the 2D beam trajectory.

#### 8.2.3.1 Surface Normal Estimation

We also use the projective geometry formulated in Section 8.2.1 for the initial surface estimation. Given the analysis of an ellipse trajectory in the image plane, an initial normal vector of the surface is set, by rotating the axis of the cone  $v_z$  about the  $y$ -axis of the cone

coordinate,  $\mathbf{v}_y$ , by the angle  $\theta_{plane}$ :

$$\mathbf{n}_{init} = \mathbf{R}(\hat{\mathbf{v}}_y, \theta_{plane})\mathbf{v}_z \text{ and } \mathbf{P}_{plane} = \mathbf{P}_{RCM} - d_{plane}\mathbf{v}_z, \quad (8.23)$$

where the coordinates of the cone beam is represented as  $\mathbf{R}_C^{ASAP} = [\mathbf{v}_x \quad \mathbf{v}_y \quad \mathbf{v}_z]$ . It is also noted that the estimation of the point  $\mathbf{P}_{plane}$  is independent of the estimation of the surface normal. Since the true surface normal exists in a 3D circle representing an infinite set of normal vectors, we regard the surface normal to be found  $\mathbf{n}_{plane}$  as a rotation of the initial normal  $\mathbf{n}_{init}$  about the axis of the cone as in (8.24),

$$\mathbf{n}_{plane} = \mathbf{R}(\hat{\mathbf{v}}_z, \theta_c)\mathbf{n}_{init}, \quad (8.24)$$

where the angle of rotation is denoted by  $\theta_c$ .

Give the number  $k$  of data points on the trajectory, we define an object function as in (8.25), in order to find the angle  $\theta_c$ .

$$\arg \min_{\theta_c \in [-\pi, +\pi]} \sum_{k=1}^n (\theta_{beam}^k - \theta_{proj}^k)^2, \quad (8.25)$$

where the angles of the  $k$ th data point with respect to the major axis of each ellipse are denoted by  $\theta_{beam}^k$  and  $\theta_{proj}^k$  for the beam trajectory on the image and the estimated plane, respectively.

First, we calculate the relative angle of each data point,  $\theta_{beam}^k$ , using (8.26) and (8.27).

$$\mathbf{p}_{beam}^k = \mathbf{p}_{beam}^k - \mathbf{c}_e \text{ and } [\mathbf{p}_{bx}^k \quad \mathbf{p}_{by}^k]^T = \mathbf{R}(-\theta_e)\mathbf{p}_{beam}^k \quad (8.26)$$

$$\theta_{beam}^k = \text{atan2}(p_{by}^k / m_b, p_{bx}^k / m_a) \quad (8.27)$$

In order to calculate the angle  $\theta_{proj}^k$ , the projected point  $\mathbf{P}_{proj}^k$  needs to be found by the intersection between the estimated plane and a ray created by the tip  $\mathbf{P}_{tip}^k$  and RCM  $\mathbf{P}_{RCM}$  positions.

$$\mathbf{P}_{proj}^k = \Phi(\mathbf{P}_{tip}^k, \mathbf{P}_{RCM}, \mathbf{n}_{plane}, \mathbf{P}_{plane}) \quad (8.28)$$

Given transformation from the ASAP to the plane coordinates  $\mathbf{T}_{ASAP}^{plane}$ , the projected point belonging to the estimated plane is represented as a 2D point  $\mathbf{p}_{proj}^k$ , by disregarding the  $z$ -component of the 3D vector  $\mathbf{P}_{proj}^k$  on the plane:

$$\mathbf{p}_{proj}^k \equiv \frac{1}{S_{cam}} \mathbf{T}_{ASAP}^{plane} \mathbf{P}_{proj}^k, \quad (8.29)$$

where the point is scaled down by the image scale  $S_{cam}$ . Once we are given a set of 2D points that forms a virtual ellipse on the estimated plane, the relative angle of the point,  $\theta_{proj}^k$ , is calculated using the parameters of the projected ellipse, in the same manner as in (8.26) and (8.27).

As a result, we finally obtain the angle  $\theta_e$  that minimizes the object function in (8.25), using the Matlab™ function 'fminbnd.m,' which finds the minimum of a function within a fixed interval for a single variable. It should be noted that two possible solutions for the angle  $\theta_e$  exist, due to the ‘ $\pi$ ’ ambiguity of an ellipse; the inclination angle of the major axis is only defined within a range of  $[-\pi/2, \pi/2]$ . In order to identify the true surface normal, we use prior knowledge, such that the  $y$ -component of the surface normal should be negative, as the ASAP always sits head-down for receiving the LED light emitted from the Micron handle; head-up orientation is impractical given that an operator would not hold the tool at an obtuse angle from the surface.

### 8.2.3.2 Coordinate Mapping

The coordinate mapping in the single cone beam reconstruction is relatively simple, compared to the dual cone beam reconstruction, because the point correspondences are already taken into account in the estimation of the normal vector. Given the surface normal  $\mathbf{n}_{plane}$  in (8.24), we define a 3D rotation  $\mathbf{R}_v^n$  from the axis of the cone  $\mathbf{v}_z$  to the normal vector  $\mathbf{n}_{plane}$ . By applying the transformation  $\mathbf{R}_v^n$  to the coordinate representation of the cone beam  $\mathbf{R}_{C1}^{ASAP}$ , we attain a new coordinate representation  $\mathbf{R}_v^n \mathbf{R}_{C1}^{ASAP}$ ; the resulting trajectory is shown as the blue dotted line in Fig. 8.9. Finally, the coordinate mapping is accomplished by applying rotation about the surface normal  $\mathbf{n}_{plane}$  by the angle  $\theta_{uv}$  as in (8.30).

$$\mathbf{R}_{image}^{ASAP} = \mathbf{R}(\mathbf{n}_{plane}, \theta_{uv}) \mathbf{R}_v^n \mathbf{R}_{C1}^{ASAP}, \text{ where } \theta_{uv} = \theta_{proj} - \theta_e. \quad (8.30)$$

The angle  $\theta_{uv}$  is set by the difference between the inclination angles of the two ellipses, in order to align the major axes of those ellipses:  $\theta_e$  from the actual beam trajectory, and  $\theta_{proj}$  from projected ellipse.

## 8.3 Evaluation of Cone Beam Reconstruction

We use the single cone beam reconstruction for further experiments, since the dual cone beam reconstruction is relatively sensitive to estimation of two circles in 3D as shown in Fig. 8.8. For instance, it could yield a totally erroneous solution even by a certain error in one of the two circles, although the other can still offer a quite close normal vector to the true one. In contrast, the single cone beam reconstruction can still provide a reasonable solution, by keeping point correspondences to be matched up. Of course, the single cone beam reconstruction also has the ambiguity in finding the surface normal; this would easily be addressable by taking into account the practical orientation of the ASAP head.

We first analyze the sensitivity of the single cone beam reconstruction with synthetic data, depending on various parameters that may lead to error in the estimation. Then, the performance of the cone beam reconstruction is evaluated using real data.

### 8.3.1 Simulation

We first investigate how the tilt angle of the estimated plane varies upon the aspect ratio retrieved from the ellipse in the image plane, since the aspect ratio is a primary parameter that determines the angle of rotation for yielding the initial surface normal. In addition, the resulting angle does not change over the next procedures to find the true surface normal.

As shown in Fig. 8.10, the angle of the scanning tip with respect the estimated plane rapidly increases, as the aspect ratio of the ellipse decreases: getting closer to a perfect

TABLE 8.1. SETTINGS FOR EVALUATION OF CONE BEAM RECONSTRUCTION

Description	Values
Major axis	82.486 pixels
Minor axis	63.651 pixels
Aspect ratio	1.296
Scan diameter	1.0 mm
RCM distance from the tool tip	21 mm
Image scale	8.588 $\mu\text{m}/\text{pixel}$
Estimated tip angle	50.516°
Estimated tip distance from surface	1.509 mm

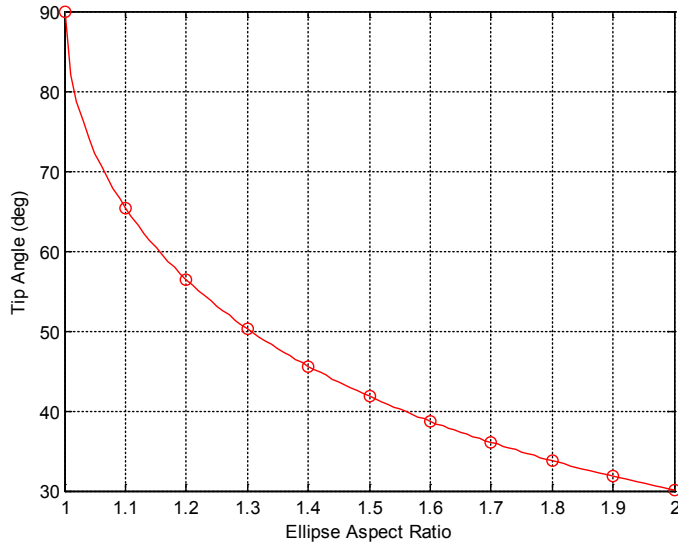


Fig. 8.10. The tip angle with respect to the estimated plane, according to the aspect ratio of an ellipse.

circle. Hence, as the tip becomes perpendicular to the surface, estimation of the angle is less resolvable.

The angle at which an operator holds the Micron handle is typically in the range of 40–65°. For example, a natural angle at which the tool is held without the scleral constraint is about 45°. The angle becomes larger when holding the tool in vitreoretinal surgery due to the location of a trocar used; the typical angle in use of the eye phantom is about 60°. Therefore, we can conclude that the tilt angle of interest exists within an acceptable range for our cone beam reconstruction. If Micron were held at an angle close to the 90° (nearly perpendicular to the surface), the cone beam construction would not have such high resolvability. Parameters used for the simulation are taken from real data and summarized in Table 8.1.

We also evaluate how the resulting surface normal and depth are affected by uncertainty in measurement of the major and minor axes of an ellipse. For simulation, the major and minor axes vary by  $\pm 3$  pixels from the initial values described in Table 8.1; the pixels correspond to  $\pm 26 \mu\text{m}$  under the 10X magnification of the operating microscope used. Fig. 8.11 shows the resulting errors in estimation of the surface normal and depth, regarding variation on estimation of the ellipse. According to the simulation, the angle error is found to be between -5.31° and 6.48°, leading to a maximum depth error of  $\pm 800 \mu\text{m}$ . From this analysis, we can determine an acceptable threshold for running the RANSAC algorithm to remove outliers on an ellipse trajectory; details will be discussed later in the test of real

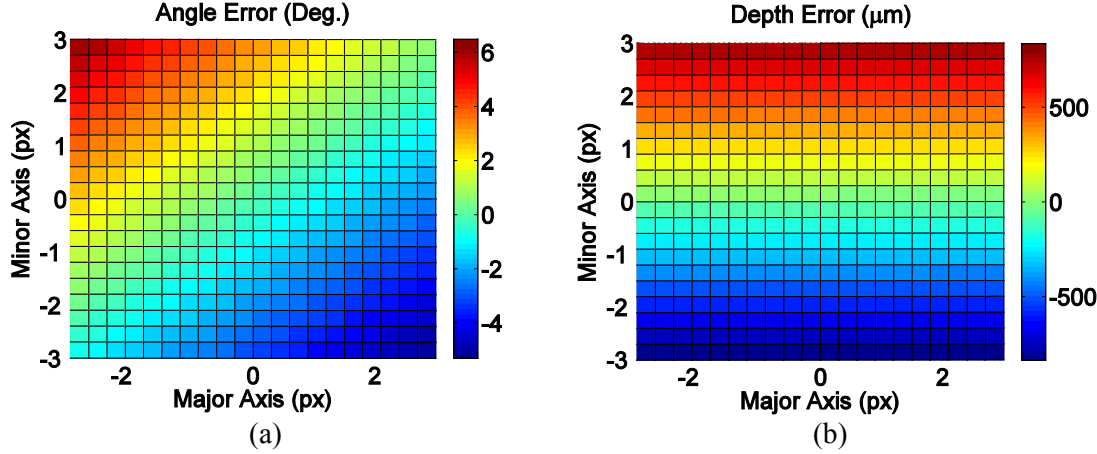


Fig. 8.11. (a) Angle error in surface normal estimation, led by errors in lengths of the major and minor axes in pixels. (b) Surface depth error by variation on lengths of the major and minor axes.

data. Since the depth error is relatively high, compared to the angle error, the depth error is further investigated.

Although we assume the image plane is parallel to the retinal surface in a small area of interest, it is not necessarily true. In the configuration of a stereo microscope, two CCD cameras have a certain distance offset with respect to each other, in order to offer disparity for stereo depth perception, which results in inclination of their optical axes. Accordingly, we need to admit a certain error in estimation of the angle. We thus set the acceptable range of the angle variation as  $\pm 10^\circ$  in the following simulation, and see how depth error would occur. For the angle variation, the length of the minor axis is changed, while the length of the major axis is fixed. As a result, the depth error is estimated as from -3000 to

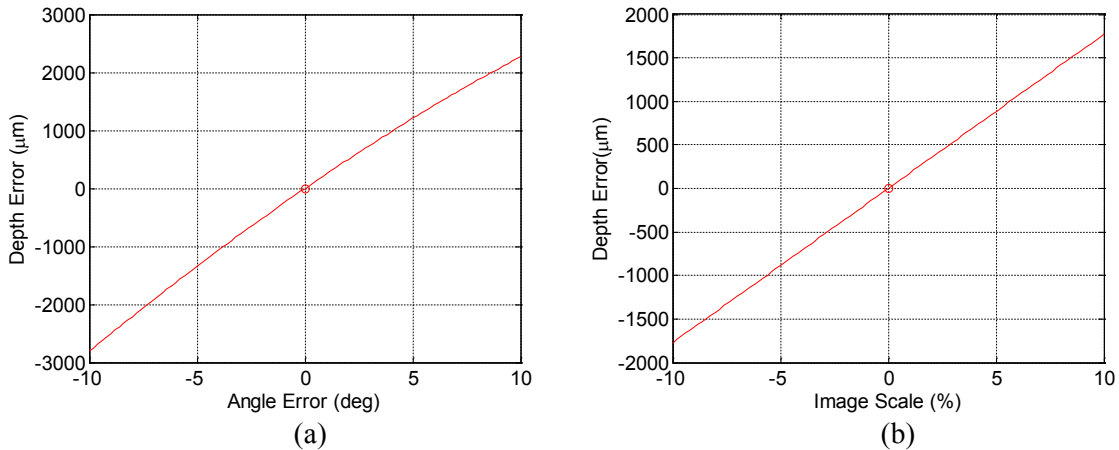


Fig. 8.12. (a) Depth error in surface estimation, led by the angle error in estimation of the surface normal. (b) Depth error according to uncertainty on the image scale.

2000  $\mu\text{m}$  as shown in Fig. 8.12(a). The depth estimation error can also be exacerbated by error in the image scale used. Fig. 8.12(b) presents the variation in depth error depending on uncertainty on the image scale, within a range of  $\pm 10\%$  from the nominal value.

It is thus found that the depth estimation of the surface is relatively sensitive, and could yield a large error, because it is derived by the large offset value  $d_{\text{plane}}$  from the RCM in (8.4). For instance, the offset  $d_{\text{plane}}$  defining a plane on the plane should be greater than the distance  $h_{\text{RCM}}$  (e.g., 20 mm) between the RCM and the tool tip. Accordingly, small error in the major axis and/or image scale can amplify error in depth estimation.

### 8.3.2 Tests with Real Data

The single cone beam reconstruction was also evaluated on real data acquired by circular scanning of the laser probe. Tests were conducted under two test conditions: “open-sky” and eye phantom environments. First, we performed open-sky tasks, which were designed to primarily evaluate performance of the cone beam reconstruction itself, without involving optical distortion and any constraint on the RCM (herein regarded as a pivot point for scanning). The reconstruction was then evaluated in the eye phantom with water inside and a contact lens on top. Hence, the final goal of these tests is to investigate the feasibility of the cone beam reconstruction in a realistic environment.

#### 8.3.2.1 Open-Sky

First, we need to determine the most effective size of scan diameter at the tool tip. For instance, if a smaller size is used for the scan, the resulting ellipse in the image plane could also be small, and may form an inaccurate shape of the ellipse due to low signal-to-noise ratio. On the other hand, if too large a size is used, the resulting trajectory might be degraded as the manipulator reaches the edge of its workspace. Hence, it is important to determine an appropriate size of scan diameter, for attaining reliable results.

Scan diameters for these tests were set in a range of 300–1500  $\mu\text{m}$  as presented in Fig. 8.13. All tests were performed under 10X magnification, for which the image scale is 8.59  $\mu\text{m}$  per pixel. To exclude other effects, Micron was firmly affixed to a solid base. For comparison, a reference plane was reconstructed using stereo vision. The plane was thus regarded as the ground truth for investigating the angle difference between two surface normal vectors: one from the reference and the other from the estimated plane. In addition, we also defined depth error of the estimated plane with respect to the reference plane.

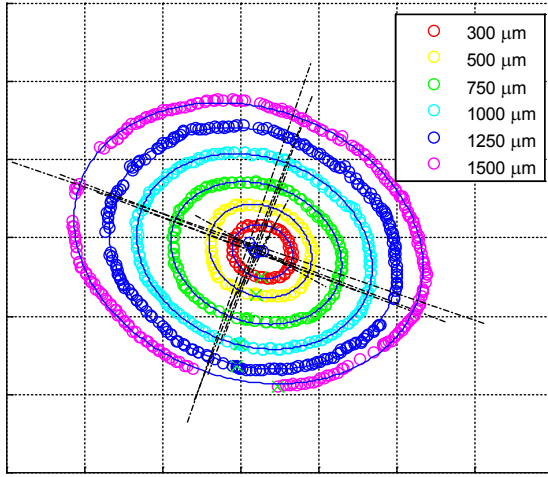


Fig. 8.13. Ellipse trajectories with respect to the size of scanning diameter.

As shown in Fig. 8.14, the surface normal was reliably estimated at scanning diameters greater than 750  $\mu\text{m}$ . In contrast, large errors were produced by small scanning diameters, such as 300 and 500  $\mu\text{m}$ . The depth error also shows a similar trend as the scanning diameter increases. Small error was thus found with scanning diameters greater than 1000  $\mu\text{m}$ . From these results, the effective size of scanning diameter was determined as 1000–1250  $\mu\text{m}$  for further experiments.

We then evaluated how reliably the cone beam reconstruction could estimate the surface for multiple measurements. These tests were repeated for a total of 10 trials, with the manipulator firmly fixed. In addition to the repeatability test, the results of the cone beam

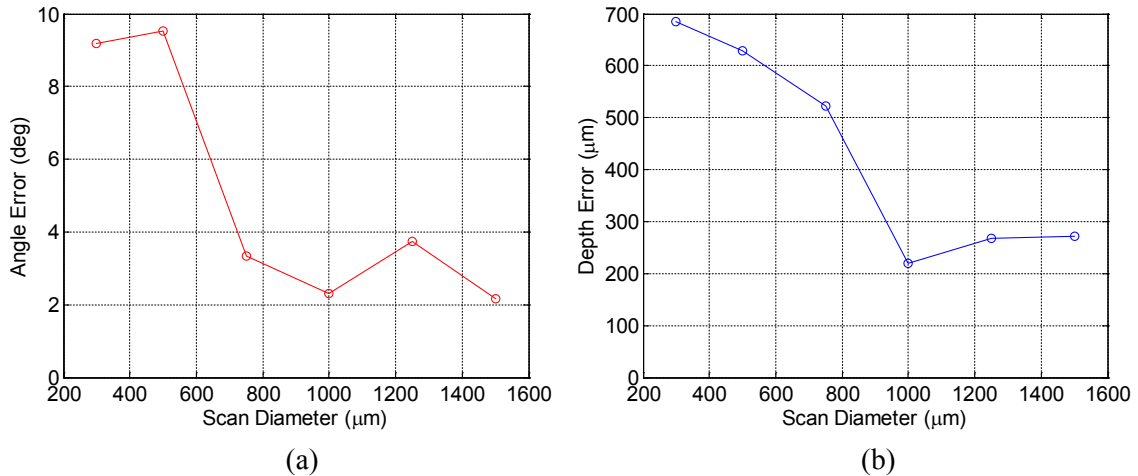


Fig. 8.14. Angle and depth errors in surface estimation with respect to the size of scan diameter: (a) angle error and (b) depth error.

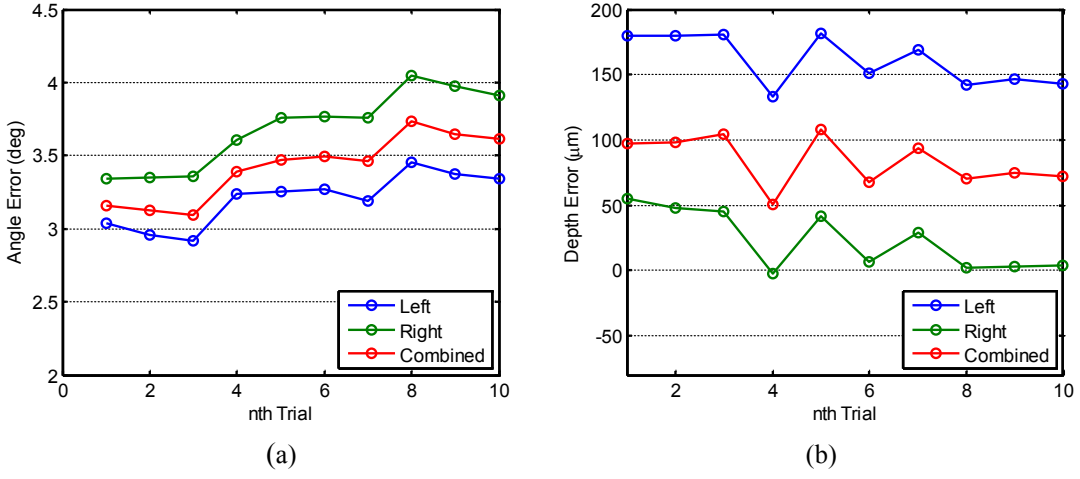


Fig. 8.15. (a) Repeated measurements of angle errors for 10 trials. (b) Depth errors for 10 trials.

reconstruction are compared, given ellipse trajectories obtained in both the left and right image plane. We also applied the cone beam reconstruction on the combined ellipse trajectory, by taking averages of the corresponding ellipse parameters, because a typical operating microscope incorporates stereo cameras for depth perception. Hence, the major and minor axes of the two ellipses were averaged for estimating the tilting angle of the plane with respect to the axis of a scanning cone. The point on the plane was also calculated using the average angle.

The average angle errors over the total 10 trials were measured in a range of 3–4° for all cases: the left, right, and combined data. The combined data shows the average behavior of the results obtained in the left and right image plane, for both angle and depth errors, as presented in Fig. 8.15. Fig. 8.15 also shows that the angle error obtained in the left image plane is larger than the error from the right plane for all repeated measurements, whereas the depth error is lower in the right image plane. However, these trends did not hold in other tests. In addition, it is found experimentally that depth estimation from the combined data is slightly more robust than results from a single camera, yielding lower standard deviations.

The last test in the open-sky setting was to investigate the reconstruction accuracy under handheld conditions, whereas all former tests were conducted in firmly fixed conditions. Since data obtained by handheld scanning are likely to be noisy, the RANSAC algorithm is adopted to remove outliers from the data, and retrieve an actual elliptical trajectory as closely as possible. A threshold for determining outliers was set at 20 μm by taking into

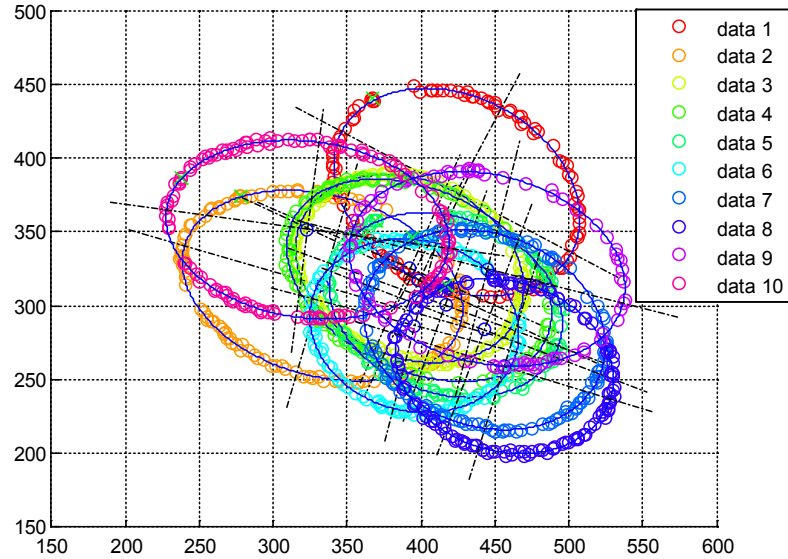


Fig. 8.16. Ellipse trajectories obtained by handheld beam scanning. The circles represent the data points yielded by the RANSAC algorithm. The blue trajectories depict the fitted ellipses after removing outliers

account the positioning accuracy of the micromanipulator, as described in Section 4.2.2.

In total, 10 trajectories were obtained for the analysis, as presented in Fig. 8.16. After applying the RANSAC algorithm, about 60% of the data points were used for fitting ellipses. The levels of average errors in both surface normal and depth estimation are similar to the results from the clamped tests. However, a larger standard deviation is

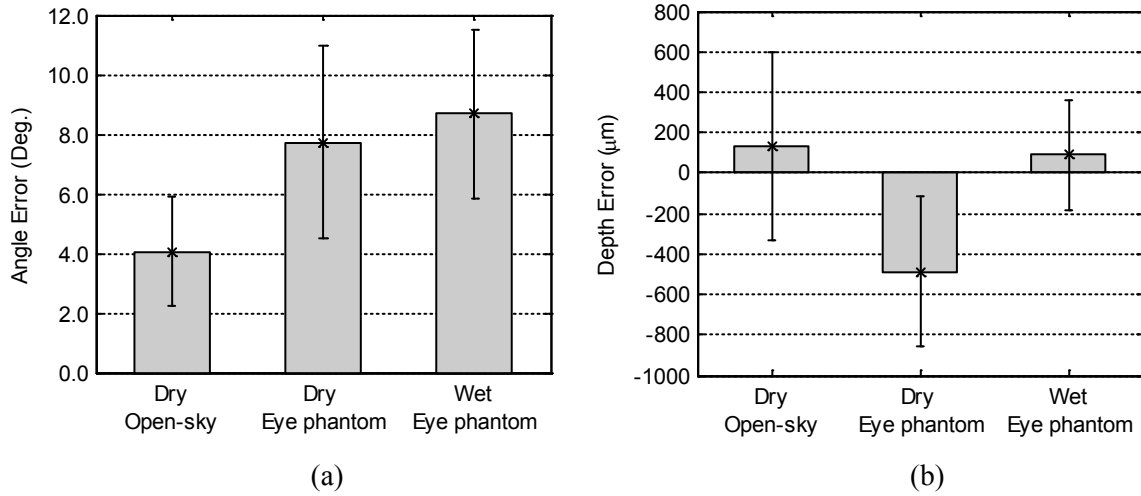


Fig. 8.17. Angle and depth errors in surface estimation by handheld cone beam scanning: (a) angle errors and (d) depth errors.

observed in handheld tasks, compared to the clamped tests, because various locations and orientations of the scanning probe were taken at the beginning of each scan. The average angle and depth error were measured as  $4.05\pm1.83^\circ$  and  $38\pm464 \mu\text{m}$  for the total 10 trials, which are still acceptable in use, compared to the accuracy of stereo reconstruction.

### 8.3.2.2 Eye Phantom

The performance of the cone beam reconstruction was evaluated in the eye phantom. We used the same eye phantom model introduced in Section 7.3.1. Before running the cone beam reconstruction, the surface of a paper slide sitting on the bottom of the eye phantom was reconstructed using stereo cameras, in order to offer the ground truth plane. First, we tested the cone beam reconstruction in the dry phantom. In contrast to the experiments performed open-sky, the laser probe was inserted into the eye phantom through a trocar and supported at the point of entry. The final test was conducted in the water-filled eye phantom, including a contact lens on the top, as shown in Fig. 8.18(a), in order to evaluate the reconstruction accuracy under optically distorted imaging conditions, in particular for depth; the image scale under the wet setting was calibrated before experiments. For evaluation, we compared the estimated plane via the cone beam reconstruction with the reference plane given by stereo reconstruction, in terms of the angle and depth errors.

For the total 10 trials in the dry phantom, the average angle error was measured as  $7.73\pm3.26^\circ$ , the depth error was  $-487\pm371 \mu\text{m}$ . Both angle and depth errors were larger

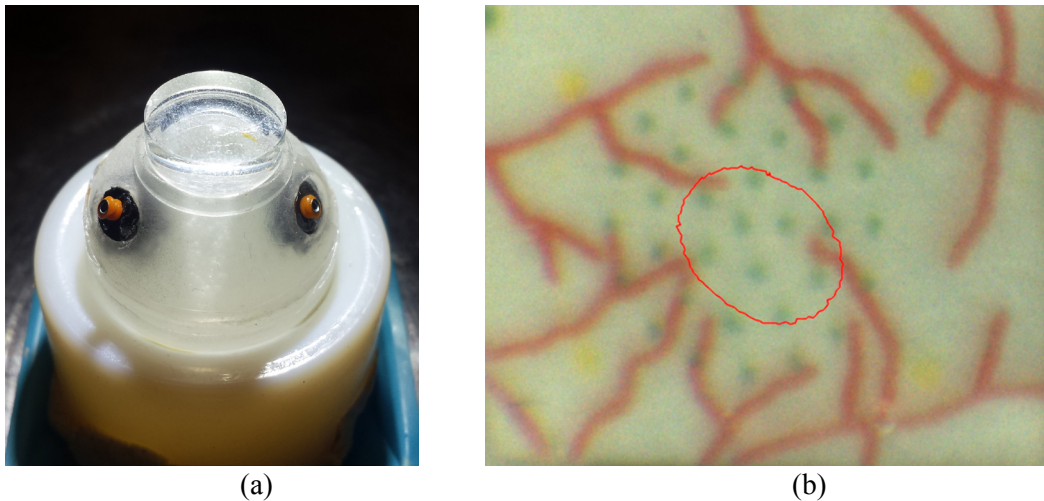


Fig. 8.18. (a) Eye phantom filled with water and also covered with the contact lens. (b) Resulting ellipse trajectory obtained by handheld scanning in the eye phantom.

than those attained in the flat surface with the scleral constraint. Moreover, the standard deviations were also larger than the results from the flat surface.

In the wet phantom model, imaging quality was relatively poor, and also the depth of field became shallow due to the contact lens used, compared to imaging in air. As a result, the average angle error is slightly larger than in the dry phantom, whereas depth error is significantly reduced, as shown in Fig. 8.17. It is noted that we disregarded certain erroneous reconstruction results in the analysis, in which the tip angle with respect to the plane was greater than  $70^\circ$ ; such a high incident angle is ergonomically very unnatural in holding Micron. It occasionally occurred in eye phantom tasks, leading to erroneous surface normal estimation, while it was not observed in the open-sky tasks. It can be caused primarily by the horizontal alignment of the contact lens, which is primarily assumed to be parallel to the retinal surface and the image plane. However, the lens could get tilted when a large rotation is introduced to the eye ball, in order to aim an off-centered area. It may also be due to error in tip position measurement, primarily led by inaccurate tip offset calibration. For that case, a perfect circular trajectory would not be created with respect to the real tip, which is subject to an erroneous elliptical trajectory. In addition, another possible source of the error could be resting the tool at the RCM during operation of scanning, which could degrade the scan trajectory due to transverse force acting on the middle of the long and slender tool. Furthermore, it is found that the higher the estimated incident angle is, the larger the angle error is. This is also true in stereo reconstruction used for creating the reference plane, especially in the eye phantom, due to inaccuracy in detection of the tool tip for the camera calibration. Accordingly, it may be hard to conclude that the depth error is really smaller in the wet eye phantom, compared to the dry phantom. However, for both cases, the surface normal could be estimated to an acceptable level, yielding angle errors less than  $10^\circ$ ; such an angular error would result in  $\pm 260 \mu\text{m}$  error in depth in the area of interest (3 mm in diameter).

## 8.4 Visual Servoing Experiments and Results

We finally perform visual servoing of a laser probe in the wet eye phantom and porcine eyes *ex vivo*, which had not been feasible previously, due to erroneous stereo reconstruction of the retinal surface. Since the concept of hybrid visual servoing was successfully validated in Chapter 7, the cone beam reconstruction is applied in place of stereo reconstruction for demonstration in realistic eye models.

In Chapter 7, the image Jacobian was derived by projecting points along the principal vectors of the target plane onto the image planes, using the camera projection matrices. In cone beam reconstruction, the interaction matrix defined in (7.6) can be described by an image scale used, because the image coordinates are already matched with the principal vectors,  $\mathbf{u}_{\text{plane}}$  and  $\mathbf{v}_{\text{plane}}$  for the plane as in Section 8.2.3.2. Accordingly, we can simply formulate the inverse of the interaction matrix that describes the complete image Jacobian:

$$\mathbf{J}_p^{-1} = \begin{bmatrix} s_{\text{cam}} & 0 \\ 0 & s_{\text{cam}} \end{bmatrix} \begin{bmatrix} 1 & 0 \\ 0 & -1 \end{bmatrix}, \quad (8.31)$$

where the image scale  $s_{\text{cam}}$  is determined by the zoom factor of the operating microscope. It is noted that the negative value is set for the second column vector of the right-side matrix in (8.31). This is because ASAP takes a right-handed coordinate system, whereas the image is described by a left-handed coordinate system. By substituting (8.31) into (7.10), the image Jacobian for control is completely defined in (8.32). Then, the identical control principle is applied for hybrid visual servoing, as in (7.10)–(7.12).

$$\mathbf{J}^{-1} = r_{\text{lever}} s_{\text{cam}} [\mathbf{u} \quad -\mathbf{v}] \quad (8.32)$$

### 8.4.1 Eye Phantom

The hybrid visual servoing was first tested in the wet eye phantom, using the cone beam reconstruction. The eye phantom was filled with water in place of the vitreous humor in the human eye, and also covered with a contact lens on the portion representing the cornea. In order to compensate eye movement during operation, the eyeSLAM algorithm was also used to track artificial blood vessels, as shown in Fig. 8.19. However, it was not possible to make distinct black burns on a paper slide attached to the eye phantom with the laser, since the paper was wet from the water. Therefore, we could only evaluate the feasibility of hybrid visual servoing, using the newly formulated image Jacobian in (8.32). For

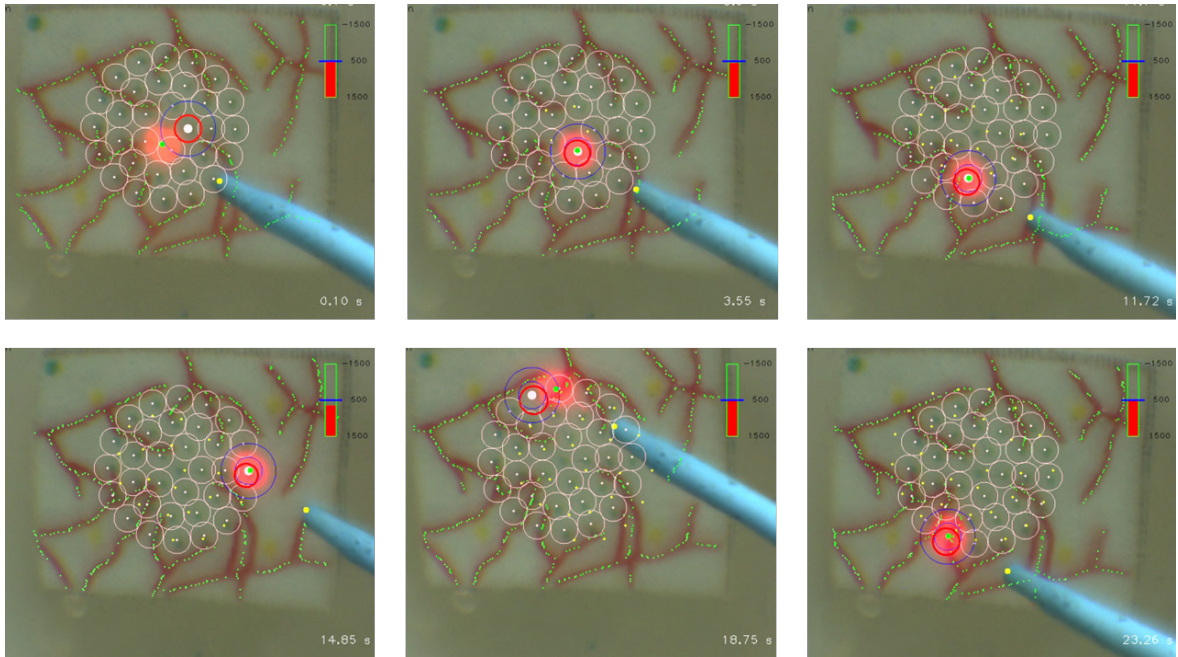


Fig. 8.19. Demonstration of hybrid visual servoing based on the cone beam reconstruction in the wet eye phantom. The pink circles indicate the preplanned targets lying on the inner surface of the eye phantom. The green dots represent the artificial blood vessels as detected by the eyeSLAM algorithm, which tracks the vessels throughout the operation. The red solid circle on a current target represents a visual cue to maintain the hand-eye coordination.

demonstration, we set a targeting threshold as  $100 \mu\text{m}$ , which was used as a typical setting for automated operation. Although we could not analyze the accuracy of automated photocoagulation, the execution time was investigated as a measure of the control performance. For example, erroneous surface estimation and/or incorrect formulation of the image Jacobian may lead to longer execution time or failure of servoing. As a result, the execution time was measured as 23.3 s, which is comparable to the results from hybrid visual servoing that used stereo-reconstruction in Chapter 7; the execution time was about 26 s for the same  $100\text{-}\mu\text{m}$  threshold.

#### 8.4.2 Porcine Eye

We also tested automated laser photocoagulation in porcine eyes *ex vivo* as shown in Fig. 8.20. However, a clear demonstration has not been shown yet. The primary difficulty in tests *ex vivo* arose in simultaneously detecting both an aiming beam and posterior segments of porcine eyes. For instance, in order to reliably detect the aiming beam, less

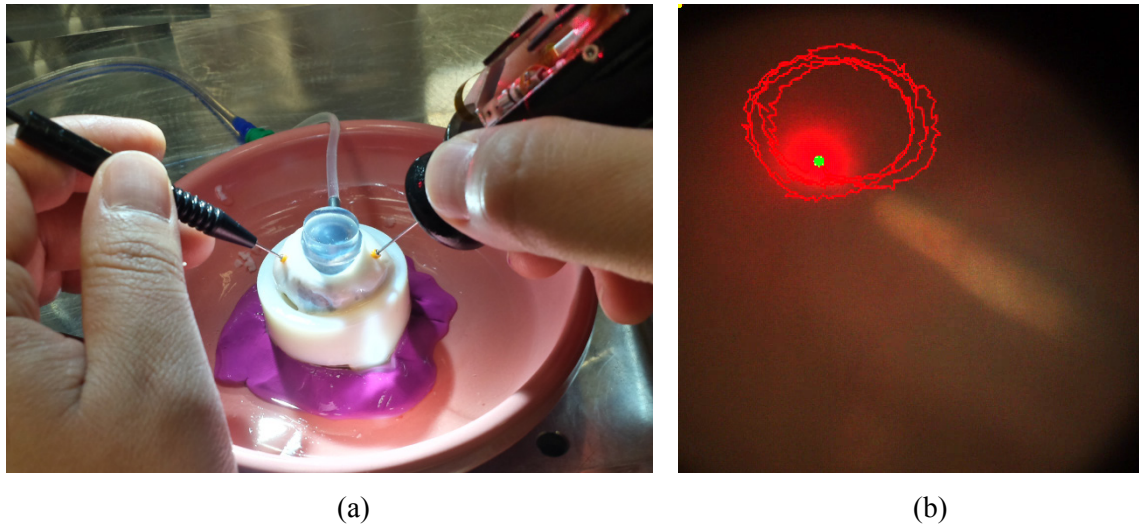


Fig. 8.20. (a) Porcine eye and intraocular surgical setup for the test *ex vivo*. (b) Elliptical trajectories created by cone beam scans inside the porcine eye.

illumination is required, whereas the brighter light is preferable for clearly imaging fundus images and tracking blood vessels. Hence, it was challenging to find a single setting to reliably detect both the aiming beam for visual servoing and blood vessels for tracking. Detection of blood vessels could also be interfered with due to the intense light of the aiming beam; the aiming beam rather widely diffuses on the translucent retina surface, than creating a clear and bright red spot. Furthermore, we could observe only a few blood vessels, for example, as one or two branches, in the porcine eyes, which resulted in either jitter or drift in tracking. Furthermore, the cornea of porcine cadaver eyes gets cloudy due to apoptosis in the corneal epithelium, which hindered clear imaging of the posterior segments of the eyes during the tests.

Therefore, we performed automated laser photocoagulation on fixed targets instead, while disabling the eyeSLAM tracking, but still utilized the cone beam reconstruction for hybrid visual servoing. Although the surface estimation via the cone beam reconstruction could not quantitatively be compared with any ground truth, it did provide a reasonable value of the surface normal for a typical ASAP head orientation. The total execution time was measured as 36 s, while 9 of 36 s were spent on a specific target; without the target, the execution time would 27s for the other 31 targets. This is due to unreliable detection of the aiming beam, caused by bubbles on the contact lens. Hence, time of operation is comparable to the previous experiments performed in the eye phantom.

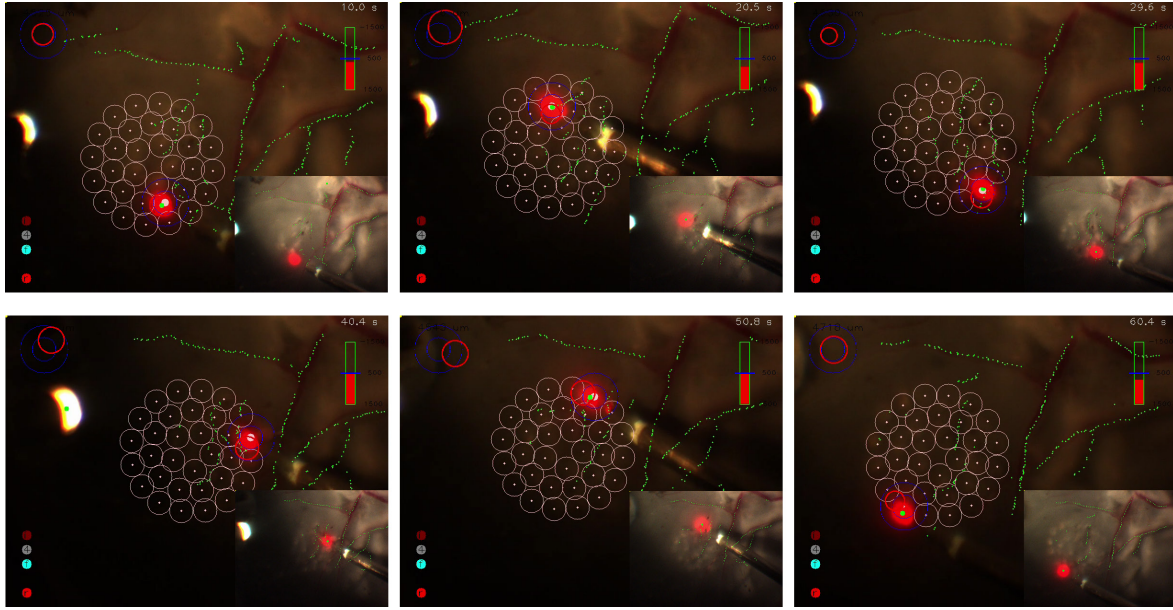


Fig. 8.21. Demonstration of automated intraocular laser surgery in a porcine eye *ex vivo*. The dissected eye was placed inside the eye phantom entailing water and a lens on top for clear imaging. The large main image shows the left camera image with aiming beam detection and moving targets. The brighter sub image at the bottom-right on the main image shows the right camera image used for tracking of blood vessels.

In order to tackle the issues in imaging *ex vivo*, we utilized both the left and right images: one for detecting the aiming beam and the other for blood vessels. Thus, different camera settings were introduced for the two cameras. For instance, the lower gain was set for the left camera to reliably detect the aiming beam, whereas the higher gain was used for clearly imaging the posterior segments in the right camera, as shown in Fig. 8.21. The tracking in the right images was then transformed to the left images via a planar homography constructed during cone beam reconstruction; Fig. 8.21 also shows the transformed blood vessels in the large main images.

We also performed the tests under a modified setting. The eyes were dissected to remove the cloudy cornea, and the eyes cut in half were placed inside the eye phantom. The phantom was then filled with water and also covered with a contact lens on top. Fig. 8.21 demonstrates automated laser photocoagulation in the porcine eye over the time of operation. The total execution time was measured as 60 s for a single trial, which is considerably longer than the time of automated operation without burning targets on the same eye: 25.2 s without the laser firing. 9 of 60 s were spent on a specific target due to unreliable detection of the aiming beam, as the retina was detached and floated in the dissected eye. In addition, undetected aiming beam delayed the time of automated

operation for 5 s. Therefore, further experiments will be performed to clearly demonstrate the advantage of automated intraocular laser surgery, by refining a relevant control scheme to handle erroneous beam detection.

## 8.5 Summary

We demonstrated robot-aided intraocular laser photocoagulation using a monocular camera in the realistic eye model. To address erroneous stereo-reconstruction in the complex eye model, the cone beam reconstruction method was proposed, utilizing the automatic scanning of the Micron and the geometric analysis of projected beam patterns.

The dual cone beam reconstruction was first formulated to estimate the retinal surface. Later, we introduced single cone beam reconstruction, to tackle practical issues raised in the dual cone beam reconstruction. Nevertheless, the dual beam reconstruction can completely describe the surface without involving any ambiguity in estimation of the surface normal; the ambiguity existing in the single cone beam reconstruction was addressed by taking into account the feasible orientation of the ASAP head. The single cone beam reconstruction was tested in various conditions, in order to evaluate its performance and the feasibility in the realistic eye model entailing different medium and optical distortion by lenses. We also investigated the accuracy of the cone beam reconstruction, regarding possible uncertainties that may exist in estimation.

Consequently, automated laser photocoagulation is accomplished by combination of the cone beam reconstruction with hybrid visual servoing introduced in Chapter 7, while accounting for practical issues in automation of microsurgery, such as camera calibration, 3D reconstruction, and zoom optics. A complete demonstration in an intact eye has not been shown yet due to instability in tracking the eye. However, it is found that the new surface estimation works for the intact eye, regardless its optical distortion, and can be used for automation of intraocular laser photocoagulation. We would be able to perform such as complete demonstration in the intact eye, by improving imaging qualities for the reliable detection of both aiming beam and blood vessels.



## 9 CONCLUSION

In this thesis, we demonstrated the design and performance of a new 6-DOF handheld micromanipulator for microsurgery. To realize the miniature 6-DOF manipulator, a new optimization framework was introduced, focusing primarily on the amount of tolerable side load introduced at an RCM during vitreoretinal surgery. Given the design optimization, we developed the new 6-DOF Micron that is superior to other handheld micromanipulators in terms of degrees of freedom and range of motion. The 6-DOF Micron thus allows control with an RCM, providing both fine manipulation for active tremor cancellation and also gross manipulation for automated microsurgery. The benefits of the 6-DOF Micron were also exploited in handheld imaging. The active tremor compensation improved the quality of handheld intraocular OCT imaging, and automatic manipulation in the large range of motion allowed multidimensional scans of single fiber OCT.

These base frameworks were then extended to accomplish automated microsurgery using the handheld micromanipulator. As a first step, we investigated the feasibility of automated intraocular laser photocoagulation in a dry eye phantom, based on position-based visual servoing. However, there are still practical problems in application in an intact eye, such as failure in 3D reconstruction due to a complex imaging system. For real-world use beyond such a simplified testbed, we proposed a hybrid visual servoing control scheme relying on a single camera, which combines monocular vision feedback with 3D position control of the Micron system. The hybrid visual servoing scheme was also validated through experiments with a dry eye phantom, while incorporating adaptive features in control and tracking the eye movement. In addition, we formalized a new framework to estimate the retinal surface, using the automatic scanning of the Micron and the geometric analysis of projected beam patterns on the surface. The new method was thus verified in the realistic phantom model, while addressing issues raised by erroneous stereo-reconstruction in the complex eye model.

Finally, these approaches were fused into the hybrid visual servoing using monocular vision for automated laser surgery. Evaluations were performed on the wet eye phantom and porcine eyes *ex vivo*, demonstrating the applicability of the framework in realistic settings.

## 9.1 Contributions

During the course of this research, I made the following contributions.

- A ***state-of-the-art handheld micromanipulator*** has been designed by introducing a **new optimization framework for the design of a miniature manipulator**. It thus provides **more degrees of freedom and larger range of motion**, which allows accommodating use through a sclerotomy: [22], [147], [163].
- A **versatile handheld micromanipulator** has been applied to **high-precision active tremor cancellation** as well as **automated operations** requiring large range of motion: [115], [146], [147], [164], [165].
- The new handheld manipulator has been utilized in **handheld intraocular imaging: stabilizing handheld imaging and acquiring multidimensional scans** from single-fiber OCT: [115], [165].
- The handheld micromanipulator enables **automated microsurgery** in conjunction with visual servoing and virtual fixture frameworks: [146].
- A **new visual servoing framework** using monocular vision was proposed **for intraocular microsurgery**. In addition, the **comparative study of handheld robot-aided intraocular laser surgery** was conducted. [LSM-submitted, TRO-submitted]
- A **new surface estimation framework applicable to an intact eye** was established, using the automated scanning of the handheld micromanipulator and the geometric analysis of projected beam patterns on the surface.
- **Automated intraocular laser surgery** has finally been demonstrated **in the realistic eye model**, in conjunction with cone beam surface reconstruction and hybrid visual servoing.

## 9.2 Future Directions

This thesis represents progressive research for realizing uses of the handheld micromanipulator in clinically realistic environments. We have tackled some practical issues encountered in real intraocular surgery. However, there still remains a large area of work in order to fully utilize the handheld manipulator in robot-assisted microsurgery. Hence, we outline several next steps that could advance the performance of the handheld micromanipulator and realize automated microsurgery in practice.

- Handheld Micromanipulator Design and Management

The performance of the manipulator can be improved by primarily refining the mechanical components. For example, the current 6-DOF Micron adopts flexures in place of conventional joint mechanisms, such as universal or ball joints. Overall stiffness of the manipulator significantly depends upon the flexure structures, in terms of diameter, length, and shape. Any undesired operation beyond a predefined workspace, especially accidental orientation changes in manipulation, may cause permanent deformation of the flexures beyond the plastic regime of the polypropylene material used. In addition, the inherent characteristics of the Squiggle motor weaken the stiffness of the manipulator. The large clearance between the motor body and screw for generating orbital motion leads to a sloppy structure overall when the motors are used as the struts of a hexapod. Hence, the design and application of a miniature mechanical joint could increase the stiffness of the manipulator and also address instability to external loads. Moreover, the higher stiffness would improve the bandwidth of the manipulator in dynamic operation, yielding improvement on active tremor cancelling performance.

To guarantee the best performance over time, individual motors should be easily replaceable and their performance well managed. For instance, the overall performance of the manipulator may be degraded due to inconsistent capabilities of the motors used, in terms of speed and force. Although the performance of an individual motor is managed using a testing jig, given a fixed amount of preload before the whole assembly, the performance would still be affected by varying loads on the motors over the time of operation. Since the motors are used as the struts of a hexapod, axial and lateral loads acting on the motors inevitably change upon a different pose of the manipulator. In addition, such varying loads on the bearing assembly located at one end of each motor may also accelerate wear on the bearing used due to its tight tolerance. Hence, a new assembly setup that incorporates a position sensor would be helpful in managing the performance of individual motors regarding varying loads.

- Cone beam Reconstruction

We proposed the concept of the cone beam reconstruction to estimate the retinal surface and found its feasibility in an optically distorted imaging system, as a proof of concept. Therefore, several refinements should be made to expect better outcomes, in terms of accuracy and robustness. First, it is found that depth estimation is relatively sensitive to uncertainties in corresponding parameters. A possible remedy might be a more sophisticated way to use both the left and right images in stereo-cameras, instead of just taking the average of ellipse parameters, since even the average method yielded lower deviation in depth estimation than a single camera provided. As the dual cone beam method addresses the ambiguity of the normal estimation, extra information given the two cameras, for example, disparity of resulting ellipses can be utilized to refine the depth estimation. In addition, the zoom factor of the microscope used for depth estimation and visual servoing should be able to found online, in order to be used under unknown optics, rather than using the pre-calibrated scale factor of the optics. For instance, the known size of the tool tip could be a cue to find such a scale factor.

Furthermore, it would be preferable for microsurgery if arbitrary beam patterns created by manual scanning could also allow estimation of the surface, utilizing the similar projective geometry used for an elliptical trajectory. For application to other domains of robot-assisted surgery, the cone beam attained by automated scanning of the handheld micromanipulator could be substituted with a diverging beam source to create a similar cone beam in space, in place of the highly collimated laser. Thus, this approach may be used to locally estimate orientation of a target lesion and proximity of an operating tool in a small area of interest, such as in endoscopic surgery.

- Visual Servoing and Control

Automated laser surgery has been demonstrated to cover a small designated area, which is limited primarily by the workspace of the manipulator. In order to cover a larger area with automated operation, we could combine fully automated operation with semiautomated operation. Thus, gross motion of the Micron handle would be introduced to locate an operating tool on a next area for treatment. Moreover, higher-order modeling of the target surface may be considered for such a large area. For example, we could build a spherical surface via mosaicking small planar patches attained by the cone beam reconstruction. In addition, the avoidance feature could be improved by applying a path-planning algorithm, in order to attain an optimal path for control, resulting in reduced operation time and enhanced safety [166].

- Fusing Different Sensor Modalities

We have shown versatile operations using the new 6-DOF handheld micromanipulator, but most of demonstrations were performed for ‘non-contact’ operations above the retinal surface. To bring benefits of the handheld manipulator to ‘contact’ operations, such as membrane peeling and vein cannulation, fusing other types of sensors that own different modalities could offer a solution. For example, an endoscopic force sensor incorporated in Micron can ensure safety, while maintaining a level of force during operation [167]. The force sensor could also be combined with image-guidance for better control, while identifying anatomical structures through vision and regulating the lateral motion of the tool tip as done in laser surgery.

Moreover, we have also presented the advantages of the new handheld micromanipulator in single-fiber OCT imaging. Thus, it would also be possible to take an advantage of OCT imaging in our control, such as highly accurate and fast depth measurement from the retinal surface. Therefore, the OCT could take responsibility for real-time depth estimation and control [78], which may also tackle the sensitivity issue in depth estimation of the cone beam reconstruction.

- Hand-Eye Coordination

Another important topic to be mentioned is how to maintain hand-eye coordination in automated operation of the handheld micromanipulator; the operator can easily drift to the edge of the reachable workspace without knowing it during automated execution. To overcome this issue, we have designed and delivered guidance cues, such as 2D circles and a bar, to an operator using a monitor and a monocular augmented display through an operating microscope. However, these are in fact insubstantial representations for the relative position of the tool tip and handle. The design and representation should be revisited by considering psychological factors [168] that affect the hand-eye coordination and effective 3D representation [169]. Furthermore, a new guidance cue for seamless transition between unaided and aided operations should be considered for further study.

### 9.3 Concluding Remarks

This thesis presented a novel 6-DOF handheld micromanipulator for robot-assisted microsurgery. Given the design optimization, we developed the new 6-DOF Micron that is superior to other handheld micromanipulators in terms of degrees of freedom and range of motion. Hence, the manipulator could perform high-precision active tremor cancellation as well as versatile automated operations in intraocular imaging and surgery. Finally, automated laser surgery was demonstrated in realistic environments, in conjunction with cone beam surface reconstruction, visual servoing, and virtual fixture frameworks. All these contributions would be invaluable foundations for real-world use of handheld robot-assisted microsurgery.

## BIBLIOGRAPHY

- [1] H. L. Brooks Jr, “Macular hole surgery with and without internal limiting membrane peeling,” *Ophthalmology*, vol. 107, no. 10, pp. 1939–1948, 2000.
- [2] F. Peral-Gutierrez, A. L. Liao, and C. N. Riviere, “Static and dynamic accuracy of vitreoretinal surgeons,” in *Proc. 26th Annu. Int. Conf. IEEE Eng. Med. Biol. Soc.*, 2004, vol. 1, pp. 2734–2737.
- [3] L. F. Hotraphinyo and C. N. Riviere, “Three-dimensional accuracy assessment of eye surgeons,” in *Proc. 23rd Annu. Int. Conf. IEEE Eng. Med. Biol. Soc.*, 2001, vol. 4, pp. 3458–3461.
- [4] Y. Ida, N. Sugita, T. Ueta, Y. Tamaki, K. Tanimoto, and M. Mitsuishi, “Microsurgical robotic system for vitreoretinal surgery,” *Int. J. Comput. Assist. Radiol. Surg.*, vol. 7, no. 1, pp. 27–34, 2012.
- [5] P. K. Gupta, P. S. Jensen, and E. de Juan Jr, “Surgical forces and tactile perception during retinal microsurgery,” *Lect. Notes Comput. Sci.*, vol. 1679, pp. 1218–1225, 1999.
- [6] X. Han and Y. Yang, “Customer requirements for a vitreoretinal robot,” in *Int. Conf. Manage. Sci. Innov.*, 2014, pp. 113–118.
- [7] I. Fleming, M. Balicki, J. Koo, I. Iordachita, B. Mitchell, J. Handa, G. Hager, and R. Taylor, “Cooperative robot assistant for retinal microsurgery,” *Lect. Notes Comput. Sci.*, vol. 5242, pp. 543–50, Jan. 2008.
- [8] G. Dogangil, B. L. Davies, and F. Rodriguez y Baena, “A review of medical robotics for minimally invasive soft tissue surgery,” *Proc. Inst. Mech. Eng. H.*, vol. 224, no. 5, pp. 653–679, May 2010.
- [9] S. Najarian, M. Fallahnezhad, and E. Afshari, “Advances in medical robotic systems with specific applications in surgery-a review,” *J. Med. Eng. Technol.*, vol. 35, no. 1, pp. 19–33, Jan. 2011.
- [10] Y. Sun and B. J. Nelson, “Biological cell injection using an autonomous microrobotic system,” *Int. J. Robot. Res.*, vol. 21, no. 10–11, pp. 861–868, Oct. 2002.
- [11] K. Moorthy, Y. Munz, A. Dosis, J. Hernandez, S. Martin, F. Bello, T. Rockall, and A. Darzi, “Dexterity enhancement with robotic surgery,” *Surg. Endosc.*, vol. 18, no. 5, pp. 790–5, May 2004.

- [12] S. M. Prasad, S. M. Prasad, H. S. Maniar, C. Chu, R. B. Schuessler, R. J. Damiano, and R. J. Damiano Jr, “Surgical robotics: impact of motion scaling on task performance,” *J. Am. Coll. Surg.*, vol. 199, no. 6, pp. 863–868, Dec. 2004.
- [13] A. R. Lanfranco, A. E. Castellanos, J. P. Desai, and W. C. Meyers, “Robotic surgery: a current perspective,” *Ann. Surg.*, vol. 239, no. 1, pp. 14–21, Jan. 2004.
- [14] H. B. Huang, S. Dong, J. K. Mills, and C. Shuk Han, “Robotic cell injection system with position and force control: toward automatic batch biomanipulation,” *IEEE Trans. Robot.*, vol. 25, no. 3, pp. 727–737, 2009.
- [15] I. W. Hunter, T. Doukoglou, S. R. Lafontaine, P. G. Charette, L. A. Jones, M. A. Sagar, G. D. Mallinson, and P. J. Hunter, “A teleoperated microsurgical robot and associated virtual environment for eye surgery,” *Presence*, vol. 2, no. 4, pp. 265–280, 1993.
- [16] P. S. Schenker, H. Das, and T. R. Ohm, “A new robot for high dexterity microsurgery,” in *Conf. Comput. Vis. Virtual Real. Robot. Med.*, 1995, vol. 905, pp. 115–122.
- [17] D. H. Bourla, J. P. Hubschman, M. Culjat, A. Tsirbas, A. Gupta, and S. D. Schwartz, “Feasibility study of intraocular robotic surgery with the da Vinci surgical system,” *Retina*, vol. 28, no. 1, pp. 154–158, Jan. 2008.
- [18] M. Shoham, M. Burman, E. Zehavi, L. Joskowicz, E. Batkilin, and Y. Kunicher, “Bone-mounted miniature robot for surgical procedures: concept and clinical applications,” *IEEE Trans. Robot. Autom.*, vol. 19, no. 5, pp. 893–901, Oct. 2003.
- [19] M. L. Nordlund, D. M. V Marques, F. F. Marques, R. J. Cionni, and R. H. Osher, “Techniques for managing common complications of cataract surgery,” *Curr. Opin. Ophthalmol.*, vol. 14, no. 1, pp. 7–19, 2003.
- [20] R. Taylor, P. Jensen, L. Whitcomb, A. Barnes, R. Kumar, Stoianovici, D. Gupta, Wang, E. De Juan, and L. Kavoussi, “A steady-hand robotic system for microsurgical augmentation,” *Int. J. Robot. Res.*, vol. 18, no. 12, pp. 1201–1210, Dec. 1999.
- [21] B. Mitchell, J. Koo, M. Iordachita, P. Kazanzides, A. Kapoor, J. Handa, G. Hager, and R. Taylor, “Development and application of a new Steady-Hand manipulator for retinal surgery,” in *Proc. IEEE Int. Conf. Robot. Autom.*, 2007, pp. 623–629.
- [22] S. Yang, R. A. MacLachlan, and C. N. Riviere, “Design and analysis of 6 DOF handheld micromanipulator,” in *Proc. IEEE Int. Conf. Robot. Autom.*, 2012, pp. 1946–1951.

- [23] R. A. MacLachlan, B. C. Becker, J. C. Tabarés, G. W. Podnar, L. A. Lobes, and C. N. Riviere, “Micron : an actively stabilized handheld tool for microsurgery,” *IEEE Trans. Robot.*, vol. 28, no. 1, pp. 195–212, 2012.
- [24] R. H. Taylor and D. Stoianovici, “Medical robotics in computer-integrated surgery,” *IEEE Trans. Robot. Autom.*, vol. 19, no. 5, pp. 765–781, 2003.
- [25] P. S. Jensen, K. W. Grace, R. Attariwala, J. E. Colgate, and M. R. Glucksberg, “Toward robot-assisted vascular microsurgery in the retina,” *Graefes Arch. Clin. Exp. Ophthalmol.*, vol. 235, no. 11, pp. 696–701, 1997.
- [26] B. C. Becker, R. A. MacLachlan, L. A. Lobes, and C. N. Riviere, “Semiautomated intraocular laser surgery using handheld instruments,” *Lasers Surg. Med.*, vol. 42, no. 3, pp. 264–273, 2010.
- [27] B. C. Becker and C. N. Riviere, “Real-time retinal vessel mapping and localization for intraocular surgery,” in *Proc. IEEE. Int. Conf. Robot. Autom.*, 2013, pp. 5360–5365.
- [28] M. Balicki, T. Xia, M. Y. Jung, A. Deguet, B. Vagvolgyi, P. Kazanzides, and R. H. Taylor, “Prototyping a hybrid cooperative and tele-robotic surgical system for retinal microsurgery,” *MIDAS J.*, pp. 1–11, 2011.
- [29] D. Pascolini and S. P. Mariotti, “Global estimates of visual impairment: 2010,” *Br. J. Ophthalmol.*, vol. 96, pp. 614–618, 2012.
- [30] “Vision Problems in the U.S.” [Online]. Available: <http://visionproblemsus.org/>.
- [31] D. S. Fong, L. Aiello, T. W. Gardner, G. L. King, G. Blankenship, J. D. Cavallerano, F. L. Ferris, and R. Klein, “Retinopathy in diabetes,” *Diabetes Care*, vol. 27 Suppl 1, pp. S84–S87, 2004.
- [32] J. B. Saaddine, A. A. Honeycutt, K. M. V Narayan, X. Zhang, R. Klein, and J. P. Boyle, “Projection of diabetic retinopathy and other major eye diseases among people with diabetes mellitus: United States, 2005-2050,” *Arch Ophthalmol*, vol. 126, no. 12, pp. 1740–1747, 2008.
- [33] Prevent Blindness America, “The economic impact of vision problems: the toll of major adult eye disorders, visual impairment and blindness on the U.S. economy,” 2009.
- [34] Diabetic Retinopathy Study Research Group, “Photocoagulation treatment of proliferative diabetic retinopathy: clinical application of Diabetic Retinopathy Study (DRS) findings, DRS Report Number 8,” *Ophthalmology*, vol. 88, no. 7, pp. 583–600, Jul. 1981.

- [35] Q. Mohamed, M. Gillies, and T. Wong, “Management of diabetic retinopathy: a systematic review,” *J. Am. Med. Assoc.*, vol. 298, no. 8, pp. 902–916, 2007.
- [36] P. Sternberg, D. P. Han, J. H. Yeo, C. C. Barr, H. Lewis, G. A. Williams, and W. F. Mieler, “Photocoagulation to prevent retinal detachment in acute retinal necrosis,” *Ophthalmology*, vol. 95, pp. 1389–1393, 1988.
- [37] Early Treatment Diabetic Retinopathy Study Research Group, “Photocoagulation for diabetic macular edema. Early Treatment Diabetic Retinopathy Study Report Number 1,” *Arch. Ophthalmol.*, vol. 103, no. 12, pp. 1796–1806, 1985.
- [38] F. Bandello, P. Lanzetta, and U. Menchini, “When and how to do a grid laser for diabetic macular edema,” *Doc. Ophthalmol.*, vol. 97, pp. 415–419, Jan. 1999.
- [39] The Branch Vein Occlusion Study Group, “Argon laser photocoagulation for macular edema in branch vein occlusion,” *Am. J. Ophthalmol.*, vol. 98, pp. 271–282, 1984.
- [40] A. Pielen, N. Feltgen, C. Isserstedt, J. Callizo, B. Junker, and C. Schmucker, “Efficacy and Safety of Intravitreal Therapy in Macular Edema Due to Branch and Central Retinal Vein Occlusion: A Systematic Review,” *PLoS One*, vol. 8, no. 10, pp. 1–21, 2013.
- [41] C. Haritoglou, I. W. Reiniger, M. Schaumberger, C. A. Gass, S. G. Priglinger, and A. Kampik, “Five-year follow-up of macular hole surgery with peeling of the internal limiting membrane: update of a prospective study,” *Retina*, vol. 26, no. 6, pp. 618–622, 2006.
- [42] R. N. Frank, “Retinal laser photocoagulation: Benefits and risks,” *Vision Res.*, vol. 20, no. 12, pp. 1073–1081, Jan. 1980.
- [43] M. S. Blumenkranz, D. Yellachich, D. E. Andersen, M. W. Wiltberger, D. Mordaunt, G. R. Marcellino, and D. Palanker, “Semiautomated patterned scanning laser for retinal photocoagulation,” *Retina*, vol. 26, no. 3, pp. 370–376, Mar. 2006.
- [44] C. H. G. Wright, S. F. Barrett, and A. J. Welch, “Design and development of a computer-assisted retinal laser surgery system,” *J. Biomed. Opt.*, vol. 11, no. 4, p. 041127, Jan. 2006.
- [45] N. Matsunaga, H. Ozeki, Y. Hirabayashi, S. Shimada, and Y. Ogura, “Histopathologic evaluation of the internal limiting membrane surgically excised from eyes with diabetic maculopathy,” *Retina*, vol. 25, no. 3, pp. 311–316, 2005.
- [46] A. M. Joussen, T. W. Gardner, and B. Kirchhof, *Retinal vascular disease*. Springer, 2007.

- [47] J. N. Weiss, “Apparatus and method for cannulating retinal blood vessels.” Google Patents, 2002.
- [48] F. W. Mohr, V. Falk, A. Diegeler, T. Walther, J. F. Gummert, J. Bucerius, S. Jacobs, and R. Autschbach, “Computer-enhanced ‘robotic’ cardiac surgery: experience in 148 patients,” *J. Thorac. Cardiovasc. Surg.*, vol. 121, no. 5, pp. 842–853, 2001.
- [49] M. R. Katz, F. Van Praet, D. De Canniere, D. Murphy, L. Siwek, U. Seshadri-Kreaden, G. Friedrich, and J. Bonatti, “Integrated coronary revascularization: percutaneous coronary intervention plus robotic totally endoscopic coronary artery bypass,” *Circulation*, vol. 114, 2006.
- [50] P. Modi, E. Rodriguez, and W. R. Chitwood, “Robot-assisted cardiac surgery,” *Interact. Cardiovasc. Thorac. Surg.*, vol. 9, pp. 500–505, 2009.
- [51] J. Himpens, G. Leman, and G. B. Cadiere, “Telesurgical laparoscopic cholecystectomy,” *Surg. Endosc.*, vol. 12, no. 8, p. 1091, 1998.
- [52] G. B. Cadière, J. Himpens, O. Germay, R. Izizaw, M. Degueldre, J. Vandromme, E. Capelluto, and J. Bruyns, “Feasibility of robotic laparoscopic surgery: 146 cases,” *World J. Surg.*, vol. 25, pp. 1467–1477, 2001.
- [53] C. N. Gutt, T. Oniu, A. Mehrabi, A. Kashfi, P. Schemmer, and M. W. Büchler, “Robot-assisted abdominal surgery,” *Br. J. Surg.*, vol. 91, no. 11, pp. 1390–1397, 2004.
- [54] A. W. Partin, J. B. Adams, R. G. Moore, and L. R. Kavoussi, “Complete robot-assisted laparoscopic urologic surgery: a preliminary report,” *J. Am. Coll. Surg.*, vol. 181, pp. 552–557, 1995.
- [55] A. Tewari, A. Srivastava, and M. Menon, “A prospective comparison of radical retropubic and robot-assisted prostatectomy: Experience in one institution,” *BJU Int.*, vol. 92, pp. 205–210, 2003.
- [56] S. Kaul, R. Laungani, R. Sarle, H. Stricker, J. Peabody, R. Littleton, and M. Menon, “da Vinci-assisted robotic partial nephrectomy: technique and results at a mean of 15 months of follow-up,” *Eur. Urol.*, vol. 51, pp. 186–192, 2007.
- [57] M. Degueldre, J. Vandromme, P. T. Huong, and G. B. Cadière, “Robotically assisted laparoscopic microsurgical tubal reanastomosis: a feasibility study,” *Fertil. Steril.*, vol. 74, no. 5, pp. 1020–1023, 2000.
- [58] C. Nezhat, N. S. Saberi, B. Shahmohamady, and F. Nezhat, “Robotic-assisted laparoscopy in gynecological surgery,” *JSLS, J. Soc. Laparoendosc. Surg.*, vol. 10, no. 3, pp. 317–320, 2006.

- [59] T. N. Payne and F. R. Dauterive, “A comparison of total laparoscopic hysterectomy to robotically assisted hysterectomy: surgical outcomes in a community practice,” *J. Minim. Invasive Gynecol.*, vol. 15, no. 3, pp. 286–291, 2008.
- [60] P. R. Rizun, P. B. McBeth, D. F. Louw, and G. R. Sutherland, “Robot-assisted neurosurgery,” *Semin. Laparosc. Surg.*, vol. 11, pp. 99–106, 2004.
- [61] T. Haidegger, L. Kovacs, G. Fordos, Z. Benyo, and P. Kazanzides, “Future trends in robotic neurosurgery,” in *IFMBE Proceedings*, 2008, vol. 20, pp. 229–233.
- [62] F. Chan, I. Kassim, C. Lo, C. L. Ho, D. Low, B. T. Ang, and I. Ng, “Image-guided robotic neurosurgery—an in vitro and in vivo point accuracy evaluation experimental study,” *Surg. Neurol.*, vol. 71, pp. 640–647, 2009.
- [63] R. H. Taylor, B. D. Mittelstadt, H. A. Paul, W. Hanson, P. Kazanzides, J. F. Zuhars, B. Williamson, B. L. Musits, E. Glassman, and W. L. Bargar, “Image-directed robotic system for precise orthopaedic surgery,” *IEEE Trans. Robot. Autom.*, vol. 10, pp. 261–275, 1994.
- [64] W. L. Bargar, A. Bauer, and M. Börner, “Primary and revision total hip replacement using the Robodoc system,” *Clin. Orthop. Relat. Res.*, pp. 82–91, 1998.
- [65] M. Honl, O. Dierk, C. Gauck, V. Carrero, F. Lampe, S. Dries, M. Quante, K. Schwieger, E. Hille, and M. M. Morlock, “Comparison of robotic-assisted and manual implantation of a primary total hip replacement a prospective study,” *J. Bone Jt. Surg.*, vol. 85, no. 8, pp. 1470–1478, 2003.
- [66] H. F. Fine, W. Wei, R. Goldman, and N. Simaan, “Robot-assisted ophthalmic surgery,” *Can. J. Ophthalmol.*, vol. 45, no. 6, pp. 581–584, 2010.
- [67] “Intuitive Surgical, Inc.” [Online]. Available: <http://www.intuitivesurgical.com/>.
- [68] G. H. Ballantyne and F. Moll, “The da Vinci telerobotic surgical system: the virtual operative field and telepresence surgery,” *Surgical Clinics of North America*, vol. 83, pp. 1293–1304, 2003.
- [69] C. J. Payne and G.-Z. Yang, “Hand-held medical robots,” *Ann. Biomed. Eng.*, vol. 42, no. 8, pp. 1594–1605, Jun. 2014.
- [70] V. S. E. Jeganathan and S. Shah, “Robotic technology in ophthalmic surgery,” *Curr. Opin. Ophthalmol.*, vol. 21, no. 1, pp. 75–80, Jan. 2010.
- [71] R. Douglas, “Robotic surgery in ophthalmology: reality or fantasy?,” *Br. J. Ophthalmol.*, vol. 91, no. 1, p. 1, Jan. 2007.

- [72] I. Tsui, A. Tsirbas, C. W. Mango, S. D. Schwartz, and J. Hubschman, “Robotic surgery in ophthalmology,” in *Robotic Surgery*, InTech, 2010, pp. 149–164.
- [73] A. Tsirbas, C. Mango, and E. Dutson, “Robotic ocular surgery,” *Br. J. Ophthalmol.*, vol. 91, no. 1, pp. 18–21, Jan. 2007.
- [74] A. P. Mulgaonkar, J.-P. Hubschman, J.-L. Bourges, B. L. Jordan, C. Cham, J. T. Wilson, T.-C. Tsao, and M. O. Culjat, “A prototype surgical manipulator for robotic intraocular micro surgery,” *Stud. Health Technol. Inform.*, vol. 142, pp. 215–217, 2009.
- [75] J.-L. Bourges, J.-P. Hubschman, J. Wilson, S. Prince, T.-C. Tsao, and S. Schwartz, “Assessment of a hexapod surgical system for robotic micro-macro manipulations in ocular surgery,” *Ophthalmic Res.*, vol. 46, no. 1, pp. 25–30, Jan. 2011.
- [76] E. Rahimy, J. T. Wilson, T.-C. Tsao, S. D. Schwartz, and J. P. Hubschman, “Robot-assisted intraocular surgery: development of the IRISS and feasibility studies in an animal model,” *Eye*, vol. 27, pp. 972–978, 2013.
- [77] W. Wei, R. Goldman, N. Simaan, H. Fine, and S. Chang, “Design and theoretical evaluation of micro-surgical manipulators for orbital manipulation and intraocular dexterity,” in *Proc. IEEE Int. Conf. Robot. Autom.*, 2007, pp. 3389–3395.
- [78] H. Yu, J. H. Shen, K. M. Joos, and N. Simaan, “Design, calibration and preliminary testing of a robotic telemanipulator for OCT guided retinal surgery,” in *Proc. IEEE Int. Conf. Robot. Autom.*, 2013, pp. 225–231.
- [79] T. Nakano, N. Sugita, T. Ueta, Y. Tamaki, and M. Mitsuishi, “A parallel robot to assist vitreoretinal surgery,” *Int. J. Comput. Assist. Radiol. Surg.*, vol. 4, no. 6, pp. 517–526, 2009.
- [80] T. Ueta, Y. Yamaguchi, Y. Shirakawa, T. Nakano, R. Ideta, Y. Noda, A. Morita, R. Mochizuki, N. Sugita, M. Mitsuishi, and Y. Tamaki, “Robot-assisted vitreoretinal surgery: development of a prototype and feasibility studies in an animal model,” *Ophthalmology*, vol. 116, no. 8, pp. 1538–1543, Aug. 2009.
- [81] A. Üneri, M. a Balicki, J. Handa, P. Gehlbach, R. H. Taylor, and I. Iordachita, “New steady-hand eye robot with micro-force sensing for vitreoretinal surgery,” *Proc. IEEE. RAS. EMBS. Int. Conf. Biomed. Robot. Biomechatron.*, vol. 2010, no. 26–29, pp. 814–819, Sep. 2010.
- [82] C. N. Riviere, W. T. Ang, and P. K. Khosla, “Toward active tremor canceling in handheld microsurgical instruments,” *IEEE Trans. Robot. Autom.*, vol. 19, no. 5, pp. 793–800, 2003.

- [83] C. N. Riviere, R. S. Rader, and N. V Thakor, “Adaptive canceling of physiological tremor for improved precision in microsurgery,” *IEEE Trans. Biomed. Eng.*, vol. 45, no. 7, pp. 839–846, Jul. 1998.
- [84] W. T. Ang, P. K. Pradeep, and C. N. Riviere, “Active tremor compensation in microsurgery,” in *Proc. 26th Annu. Int. Conf. IEEE Eng. Med. Biol. Soc.*, 2004, vol. 4, pp. 2738–2741.
- [85] D. Choi and C. Riviere, “Flexure-based manipulator for active handheld microsurgical instrument,” in *Proc. 27th Annu. Int. Conf. IEEE Eng. Med. Biol. Soc.*, 2005, pp. 2325–2328.
- [86] W. T. Latt, U.-X. Tan, C. Y. Shee, and W. T. Ang, “A compact hand-held active physiological tremor compensation instrument,” *2009 IEEE/ASME Int. Conf. Adv. Intell. Mechatronics*, pp. 711–716, Jul. 2009.
- [87] W. T. Latt, U.-X. Tan, C. Y. Shee, C. N. Riviere, and W. T. Ang, “Compact sensing design of a handheld active tremor compensation instrument,” *IEEE Sens. J.*, vol. 9, no. 12, pp. 1864–1871, 2009.
- [88] A. Saxena and R. V Patel, “An active handheld device for compensation of physiological tremor using an ionic polymer metallic composite actuator,” in *Proc. IEEE/RSJ Int. Conf. Intell. Robot. Syst.*, 2013, pp. 4275–4280.
- [89] D. Chang, G. M. Gu, and J. Kim, “Design of a novel tremor suppression device using a linear delta manipulator for micromanipulation,” in *Proc. IEEE/RSJ Int. Conf. Intell. Robot. Syst.*, 2013, pp. 413–418.
- [90] C. Song, D. Y. Park, P. L. Gehlbach, S. J. Park, and J. U. Kang, “Fiber-optic OCT sensor guided ‘SMART’ micro-forceps for microsurgery,” *Biomed. Opt. Express*, vol. 4, no. 7, pp. 1045–50, Jul. 2013.
- [91] G. Stetten, B. Wu, R. Klatzky, J. Galeotti, M. Siegel, R. Lee, F. Mah, A. Eller, J. Schuman, and R. Hollis, “Hand-held force magnifier for surgical instruments,” in *2nd Int. Conf. Inf. Process. Comput. Interv.*, 2011, pp. 90–100.
- [92] C. J. Payne, W. T. Latt, and G.-Z. Yang, “A new hand-held force-amplifying device for micromanipulation,” in *Proc. IEEE Int. Conf. Robot. Autom.*, 2012, pp. 1583–1588.
- [93] C. J. Payne, K.-W. Kwok, and G.-Z. Yang, “An ungrounded hand-held surgical device incorporating active constraints with force-feedback,” in *Proc. IEEE/RSJ Int. Conf. Intell. Robot. Syst.*, 2013, pp. 2559–2565.

- [94] G. Dogangil, O. Ergeneman, J. J. Abbott, S. Pane, H. Hall, S. Muntwyler, and B. J. Nelson, “Toward targeted retinal drug delivery with wireless magnetic microrobots,” in *Proc. IEEE/RSJ Int. Conf. Intell. Robot. Syst.*, 2008, pp. 22–26.
- [95] M. Kummer, J. Abbott, B. E. Kratochvil, R. Borer, A. Sengul, and B. J. Nelson, “OctoMag: An electromagnetic system for 5-DOF wireless micromanipulation,” *IEEE Trans. Robot.*, vol. 26, no. 6, pp. 1006–1017, 2010.
- [96] F. Ullrich, C. Bergeles, J. Pokki, O. Ergeneman, S. Erni, G. Chatzipirpiridis, S. Pané, C. Framme, and B. J. Nelson, “Mobility experiments with microrobots for minimally invasive intraocular surgery,” *Invest. Ophthalmol. Vis. Sci.*, vol. 54, no. 4, pp. 2853–63, Apr. 2013.
- [97] J.-P. Hubschman, J.-L. Bourges, W. Choi, A. Mozayan, A. Tsirbas, C.-J. Kim, and S.-D. Schwartz, “‘The Microhand’: a new concept of micro-forceps for ocular robotic surgery,” *Eye*, vol. 24, no. 2, pp. 364–367, Feb. 2010.
- [98] A. Ramadan, K. Inoue, T. Arai, and T. Takubo, “New architecture of a hybrid two-fingered micro-nano manipulator hand: optimization and design,” *Adv. Robot.*, vol. 22, no. 2–3, pp. 235–260, 2008.
- [99] J. Peirs, D. Reynaerts, and H. Van Brussel, “Design of miniature parallel manipulators for integration in a self-propelling endoscope,” *Sens. Actuators. A. Phys.*, vol. 85, no. 1–3, pp. 409–417, 2000.
- [100] U.-X. Tan, W. T. Latt, C. Y. Shee, and W. T. Ang, “A low-cost flexure-based handheld mechanism for micromanipulation,” *IEEE/ASME Trans. Mechatronics*, vol. 16, no. 4, pp. 773–778, Aug. 2011.
- [101] V. E. Gough, “Contribution to discussion of papers on research in automobile stability, control and tyre performance,” *Proc. Auto. Div. Inst. Mech. Eng.*, vol. 171, pp. 392–394, 1956.
- [102] D. Stewart, “A platform with six degrees of freedom,” *Proc. Inst. Mech. Eng.*, vol. 180, no. 1, pp. 371–386, 1965.
- [103] M. S. Fee and A. Leonardo, “Miniature motorized microdrive and commutator system for chronic neural recording in small animals,” *J. Neurosci. Meth.*, vol. 112, no. 2, pp. 83–94, 2001.
- [104] S. Yang, J. Cho, S. Lee, K. Park, J. Kim, Y. Huh, E.-S. Yoon, and H.-S. Shin, “Feedback controlled piezo-motor microdrive for accurate electrode positioning in chronic single unit recording in behaving mice,” *J. Neurosci. Meth.*, vol. 195, no. 2, pp. 117–127, 2011.

- [105] N. M. Thanh, V. Glazunov, and L. N. Vinh, “Determination of constraint wrenches and design of parallel mechanisms,” in *Int. Conf. Elect. Eng. Comput. Sci. Autom. Control*, 2010, pp. 46–53.
- [106] I. A. Bonev, D. Zlatanov, and C. M. Gosselin, “Singularity analysis of 3-DOF planar parallel mechanisms via screw theory,” *J. Mech. Des.*, vol. 125, no. 3, pp. 573–581, 2003.
- [107] X.-J. Liu, J. Wang, F. Gao, and L.-P. Wang, “On the design of 6-DOF parallel micro-motion manipulators,” in *Proc. IEEE/RSJ Int. Conf. Intell. Robot. Syst.*, 2001, vol. 1, pp. 343–348.
- [108] K.-K. Oh, X.-J. Liu, D. S. Kang, and J. Kim, “Optimal design of a micro parallel positioning platform. Part I: Kinematic analysis,” *Robotica*, vol. 22, no. 6, pp. 599–609, Nov. 2004.
- [109] A. D. Jagtap and C. N. Riviere, “Applied force during vitreoretinal microsurgery with handheld instruments,” in *Proc. 26th Annu. Int. Conf. IEEE Eng. Med. Biol. Soc.*, 2004, vol. 4, pp. 2771–2773.
- [110] C. Gosselin and J. Angeles, “Singularity analysis of closed-loop kinematic chains,” *IEEE Trans. Robot. Autom.*, vol. 6, no. 3, pp. 281–290, 1990.
- [111] R. A. MacLachlan and C. N. Riviere, “High-speed microscale optical tracking using digital frequency-domain multiplexing,” *IEEE Trans. Instrum. Meas.*, vol. 58, no. 6, pp. 1991–2001, Jun. 2009.
- [112] W. T. Ang, P. K. Khosla, and C. N. Riviere, “Kalman filtering for real-time orientation tracking of handheld microsurgical instrument,” in *Proc. IEEE/RSJ Int. Conf. Intell. Robot. Syst.*, 2004, vol. 3, pp. 2574–2580.
- [113] B. C. Becker, R. A. MacLachlan, L. A. Lobes, G. D. Hager, and C. N. Riviere, “Vision-based control of a handheld surgical micromanipulator with virtual fixtures,” *IEEE Trans. Robot.*, vol. 29, no. 3, pp. 674–683, Jun. 2013.
- [114] Y. Noda, Y. Ida, S. Tanaka, T. Toyama, M. F. Roggia, Y. Tamaki, N. Sugita, M. Mitsuishi, and T. Ueta, “Impact of robotic assistance on precision of vitreoretinal surgical procedures,” *PLoS One*, vol. 8, no. 1, p. e54116, Jan. 2013.
- [115] S. Yang, M. Balicki, R. A. MacLachlan, X. Liu, J. U. Kang, R. H. Taylor, and C. N. Riviere, “Optical coherence tomography scanning with a handheld vitreoretinal micromanipulator,” in *Proc. 34th Annu. Int. Conf. IEEE Eng. Med. Biol. Soc.*, 2012, pp. 948–951.
- [116] L. T. Du, I. F. Wessels, J. P. Underdahl, and J. D. Auran, “Stereoacuity and depth perception decrease with increased instrument magnification: comparing a non-

- magnified system with lens loupes and a surgical microscope," *Binocul. Vis. Strabismus Q.*, vol. 16, no. 1, pp. 61–67, 2001.
- [117] D. Huang, E. A. Swanson, C. P. Lin, J. S. Schuman, W. G. Stinson, W. Chang, M. R. Hee, T. Flotte, K. Gregory, and C. A. Puliafito, "Optical coherence tomography," *Science*, vol. 254, no. 5035, pp. 1178–1181, 1991.
- [118] D. F. Kiernan, W. F. Mieler, and S. M. Hariprasad, "Spectral-domain optical coherence tomography: a comparison of modern high-resolution retinal imaging systems," *Am. J. Ophthalmol.*, vol. 149, no. 1, pp. 18–31, Jan. 2010.
- [119] J. U. Kang, J.-H. Han, X. Liu, K. Zhang, C. G. Song, and P. Gehlbach, "Endoscopic functional fourier domain common path Optical coherence tomography for microsurgery," *IEEE J. Sel. Top. Quantum Electron.*, vol. 16, no. 4, pp. 781–792, Jan. 2010.
- [120] R. H. Webb, G. W. Hughes, and F. C. Delori, "Confocal scanning laser ophthalmoscope," *Appl. Opt.*, vol. 26, pp. 1492–1499, 1987.
- [121] A. Roorda, F. Romero-Borja, W. Donnelly Iii, H. Queener, T. Hebert, and M. Campbell, "Adaptive optics scanning laser ophthalmoscopy," *Opt. Express*, vol. 10, pp. 405–412, 2002.
- [122] S. Han, M. V Sarunic, J. Wu, M. Humayun, and C. Yang, "Handheld forward-imaging needle endoscope for ophthalmic optical coherence tomography inspection," *J. Biomed. Opt.*, vol. 13, no. 2, p. 020505, 2008.
- [123] S. P. N. Singh and C. N. Riviere, "Physiological tremor amplitude during retinal microsurgery," in *Proc. IEEE 28th Annu. Northeast Bioeng. Conf.*, 2002, pp. 171–172.
- [124] M. Balicki, J.-H. Han, I. Iordachita, P. Gehlbach, J. Handa, R. Taylor, and J. Kang, "Single fiber optical coherence tomography microsurgical instruments for computer and robot-assisted retinal surgery," *Lect. Notes Comput. Sci.*, vol. 5761, pp. 108–115, Jan. 2009.
- [125] X. Liu, M. Balicki, R. H. Taylor, and J. U. Kang, "Towards automatic calibration of Fourier-Domain OCT for robot-assisted vitreoretinal surgery," *Opt. Express*, vol. 18, pp. 24331–24343, 2010.
- [126] C. Song, P. L. Gehlbach, and J. U. Kang, "Active tremor cancellation by a 'Smart' handheld vitreoretinal microsurgical tool using swept source optical coherence tomography," *Opt. Express*, vol. 20, no. 21, pp. 23414–21, Oct. 2012.

- [127] J. Ren, J. Wu, E. J. McDowell, and C. Yang, “Manual-scanning optical coherence tomography probe based on position tracking,” *Opt. Lett.*, vol. 34, no. 21, pp. 3400–2, Nov. 2009.
- [128] A. Ahmad, S. G. Adie, E. J. Chaney, U. Sharma, and S. A. Boppart, “Cross-correlation-based image acquisition technique for manually-scanned optical coherence tomography,” *Opt. Express*, vol. 17, pp. 8125–8136, 2009.
- [129] K. Zhang, W. Wang, J. Han, and J. U. Kang, “A surface topology and motion compensation system for microsurgery guidance and intervention based on common-path optical coherence tomography,” *IEEE Trans. Biomed. Eng.*, vol. 56, no. 9, pp. 2318–21, Sep. 2009.
- [130] E. J. Seibel and Q. Y. J. Smithwick, “Unique features of optical scanning, single fiber endoscopy,” *Lasers Surg. Med.*, vol. 30, pp. 177–183, 2002.
- [131] E. J. Seibel, C. M. Brown, J. A. Dominitz, and M. B. Kimmey, “Scanning single fiber endoscopy: a new platform technology for integrated laser imaging, diagnosis, and future therapie,” *Gastrointest. Endosc. Clin. N. Am.*, vol. 18, no. 3, pp. 467–478, 2008.
- [132] S. Moon, S. Lee, and M. Rubinstein, “Semi-resonant operation of a fiber-cantilever piezotube scanner for stable optical coherence tomography endoscope imaging,” *Opt. Express*, vol. 18, no. 20, pp. 21183–21197, 2010.
- [133] Y. Chen, A. D. Aguirre, P. L. Hsiung, S. Desai, P. R. Herz, M. Pedrosa, Q. Huang, M. Figueiredo, S. W. Huang, A. Koski, J. M. Schmitt, J. G. Fujimoto, and H. Mashimo, “Ultrahigh resolution optical coherence tomography of Barrett’s esophagus: preliminary descriptive clinical study correlating images with histology,” *Endoscopy*, vol. 39, pp. 599–605, 2007.
- [134] X. Liu, Y. Huang, and J. U. Kang, “Distortion-free freehand-scanning OCT implemented with real-time scanning speed variance correction,” *Opt. Express*, vol. 20, no. 15, p. 16567, Jul. 2012.
- [135] S. Rodriguez Palma, B. C. Becker, L. A. Lobes, and C. N. Riviere, “Comparative evaluation of monocular augmented-reality display for surgical microscopes,” in *Proc. 34th Annu Int. Conf. IEEE Eng. Med. Biol. Soc.*, 2012, pp. 1409–1412.
- [136] A. Kampik, “Laser, intravitreal drug application, and surgery to treat diabetic eye disease,” *Oman J. Ophthalmol.*, vol. 6, no. Suppl 1, pp. S26–S31, Jan. 2013.
- [137] J. Chhablani, A. Mathai, P. Rani, V. Gupta, J. Fernando Arevalo, and I. Kozak, “Comparison of conventional pattern and novel navigated panretinal photocoagulation in proliferative diabetic retinopathy,” *Investig. Ophthalmol. Vis. Sci.*, vol. 55, pp. 3432–3438, 2014.

- [138] P. Leaver and C. Williams, “Argon laser photocoagulation in the treatment of central serous retinopathy,” *Br. J. Ophthalmol.*, vol. 63, pp. 674–677, 1979.
- [139] M. S. Markow, Y. Yang, A. J. Welch, H. G. Rylander, and W. S. Weinberg, “An automated laser system for eye surgery,” *IEEE Eng. Med. Biol. Mag.*, vol. 8, no. 4, pp. 24–29, 1989.
- [140] C. H. G. Wright, R. D. Ferguson, H. G. Rylander III, A. J. Welch, and S. F. Barrett, “Hybrid approach to retinal tracking and laser aiming for photocoagulation,” *J. Biomed. Opt.*, vol. 2, no. 2, pp. 195–203, Apr. 1997.
- [141] E. Naess, T. Molvik, D. Ludwig, S. Barrett, S. Legowski, C. Wright, and P. de Graaf, “Computer-assisted laser photocoagulation of the retina—a hybrid tracking approach,” *J. Biomed. Opt.*, vol. 7, no. 2, pp. 179–89, Apr. 2002.
- [142] I. Kozak, S. F. Oster, M. A. Cortes, D. Dowell, K. Hartmann, J. S. Kim, and W. R. Freeman, “Clinical evaluation and treatment accuracy in diabetic macular edema using navigated laser photocoagulator NAVILAS,” *Ophthalmology*, vol. 118, pp. 1119–1124, 2011.
- [143] A. V Chappelow, K. Tan, N. K. Waheed, and P. K. Kaiser, “Panretinal photocoagulation for proliferative diabetic retinopathy: pattern scan laser versus argon laser,” *Am. J. Ophthalmol.*, vol. 153, no. 1, pp. 137–142, Jan. 2012.
- [144] C. Sanghvi, R. McLauchlan, C. Delgado, L. Young, S. J. Charles, G. Marcellino, and P. E. Stanga, “Initial experience with the Pascal photocoagulator: a pilot study of 75 procedures,” *Br. J. Ophthalmol.*, vol. 92, pp. 1061–1064, 2008.
- [145] S. R. Wilkes, “Current therapy of diabetic retinopathy: laser and vitreoretinal surgery,” *J. Natl. Med. Assoc.*, vol. 85, pp. 841–847, 1993.
- [146] S. Yang, R. A. MacLachlan, and C. N. Riviere, “Toward automated intraocular laser surgery using a handheld micromanipulator,” in *Proc. IEEE/RSJ Int. Conf. Intell. Robot. Syst.*, 2014, pp. 1302–1307.
- [147] S. Yang, R. A. MacLachlan, and C. N. Riviere, “Manipulator design and operation of a six-degree-of-freedom handheld tremor-canceling microsurgical instrument,” *IEEE /ASME Trans. Mechatronics*, vol. 20, no. 2, pp. 761–772, 2015.
- [148] R. Hartley and A. Zisserman, *Multiple View Geometry in Computer Vision*. Cambridge university press, 2003.
- [149] J. Chhablani, I. Kozak, G. Barteselli, and S. El-Emam, “A novel navigated laser system brings new efficacy to the treatment of retinovascular disorders,” *Oman J. Ophthalmol.*, vol. 6, no. 1, pp. 18–22, Jan. 2013.

- [150] E. Malis, F. Chaumette, and S. Boudev, “2 1/2D visual servoing,” *IEEE Trans. Robot. Autom.*, vol. 15, no. 2, pp. 238–250, 1999.
- [151] P. I. Corke and S. A. Hutchinson, “A new partitioned approach to image-based visual servo control,” *IEEE Trans. Robot. Autom.*, vol. 17, no. 4, pp. 507–515, 2001.
- [152] S. Hutchinson, G. D. Hager, and P. I. Corke, “A tutorial on visual servo control,” *IEEE Trans. Robot. Autom.*, vol. 12, no. 5, pp. 651–670, 1996.
- [153] A. Castaño and S. Hutchinson, “Visual compliance: Task-directed visual servo control,” *IEEE Trans. Robot. Autom.*, vol. 10, no. 3, pp. 334–342, 1994.
- [154] K. Hosoda and M. Asada, “Versatile visual servoing without knowledge of true Jacobian,” in *Proc. IEEE/RSJ Int. Conf. Intell. Robot. Syst.*, 1994, pp. 186–193.
- [155] M. Jägersand, O. Fuentes, and R. Nelson, “Experimental evaluation of uncalibrated visual servoing for precision manipulation,” in *Proc. IEEE Int. Conf. Robot. Autom.*, 1997, pp. 2874–2880.
- [156] J. A. Piepmeyer, G. V McMurray, and H. Lipkin, “Uncalibrated dynamic visual servoing,” *IEEE Trans. Robot. Autom.*, vol. 20, no. 1, pp. 143–147, 2004.
- [157] P. Hynes, G. Dodds, and A. Wilkinson, “Uncalibrated visual-servoing of a dual-arm robot for surgical tasks,” in *Proc. IEEE Int. Symp. Comput. Intell. Robot. Autom.*, 2005, pp. 151–156.
- [158] C. Bergeles, K. Shamaei, J. J. Abbott, and B. J. Nelson, “Single-camera focus-based localization of intraocular devices,” *IEEE Trans. Biomed. Eng.*, vol. 57, no. 8, pp. 2064–2074, Aug. 2010.
- [159] C. Bergeles, B. E. Kratochvil, and B. J. Nelson, “Visually servoing magnetic intraocular microdevices,” *IEEE Trans. Robot.*, vol. 28, no. 4, pp. 798–809, Aug. 2012.
- [160] Y. Zhou and B. J. Nelson, “Calibration of a parametric model of an optical microscope,” *Opt. Eng.*, vol. 38, no. 12, pp. 1989–1995, 1999.
- [161] Q. Chen, H. Wu, and T. Wada, “Camera calibration with two arbitrary coplanar circles,” in *Computer Vision-ECCV 2004*, 2004, pp. 521–532.
- [162] F. Noo and R. Clackdoyle, “Analytic method based on identification of ellipse parameters for scanner calibration in cone-beam tomography,” *Phys. Med. Biol.*, vol. 3489, pp. 3489–3508, 2000.

- [163] S. Yang, R. A. MacLachlan, and C. N. Riviere, “Performance of a six-axis handheld microsurgical robot with ultrasonic linear motors,” in *ASME 5th Annu. Dyn. Syst. Control Conf.*, 2012, pp. 395–402.
- [164] S. Yang, T. S. Wells, R. A. MacLachlan, and C. N. Riviere, “Performance of a 6-degree-of-freedom active microsurgical manipulator in handheld tasks,” in *Proc. 35th Annu. Int. Conf. IEEE Eng. Med. Biol. Soc.*, 2013, pp. 5670–5673.
- [165] S. Yang, M. Balicki, T. S. Wells, R. A. MacLachlan, X. Liu, J. U. Kang, J. T. Handa, R. H. Taylor, and C. N. Riviere, “Improvement of optical coherence tomography using active handheld micromanipulator in vitreoretinal surgery,” in *Proc. 35th Annu. Int. Conf. IEEE Eng. Med. Biol. Soc.*, 2013, pp. 5674–5677.
- [166] E. J. Brunenberg, A. Vilanova, V. Visser-Vandewalle, Y. Temel, L. Ackermans, B. Platel, and B. M. ter Haar Romeny, “Automatic trajectory planning for deep brain stimulation: a feasibility study,” *Lect. Notes Comput. Sci.*, vol. 4791, pp. 584–592, 2007.
- [167] T. Wells, S. Yang, R. A. MacLachlan, L. A. Louis Jr., J. N. Martel, and C. N. Riviere, “Hybrid position/force control of an active handheld micromanipulator for membrane peeling,” *Int. J. Med. Robot. Comput. Assist. Surg.*, *in press*.
- [168] F. R. Sarlegna, G. Baud-Bovy, and F. Danion, “Delayed visual feedback affects both manual tracking and grip force control when transporting a handheld object,” *J. Neurophysiol.*, vol. 104, no. 2, pp. 641–53, Aug. 2010.
- [169] C. Hand, “A survey of 3D interaction techniques,” *Comput. Graph. forum*, vol. 16, no. 5, pp. 269–281, 1997.
- [170] “See What Eye See: Spotting Vision Problems.” [Online]. Available: <http://www.webmd.com/eye-health/eye-health-tool-spotting-vision-problems/>.
- [171] “Eye illustrations and animations for ophthalmology.” [Online]. Available: <http://jirehdesign.com/>.
- [172] M. Ober and S. Hariprasad, “Retinal Lasers: Past, Present, and Future,” *Retin. Physician*, pp. 36–39, 2009.